THE EFFECT OF CHEMICAL ADDITIVES ON THE DEPOSITION OF MAGNETITE ONTO ALLOY-800 UNDER NUCLEATE BOILING HEAT TRANSFER

by

Cyprien Gasnier

Ingénieur Civil des Mines
Ecole Nationale Supérieur des Mines de Saint-Etienne, France, 2014

A Thesis Submitted in Partial Fulfillment
of the Requirements for the Degree of

Master of Science in Engineering

in the Graduate Academic Unit of Chemical Engineering

Supervisor: Derek H. Lister, Ph.D., Chemical Engineering

Examining Board: Brian Lowry, Ph.D., Chemical Engineering
William Cook, Ph.D., Chemical Engineering
Amirkianoosh Kiani, Ph.D., Mechanical Engineering

This thesis is accepted by the
Dean of Graduate Studies

THE UNIVERSITY OF NEW BRUNSWICK

May, 2014

ABSTRACT

This thesis investigates the effects of three polymeric dispersants – two types of polyacrylic acid (PAA) and sodium polymethacrylate (PMA) – and a commercial film-forming amine (FFA) on the deposition onto heated nickel alloy of particulate magnetite from suspension in water during sub-cooled boiling and bulk boiling.

In bench-top experiments, ribbons of Nichrome immersed in a magnetite suspension are heated electrically with and without additives. Results show that deposits are less numerous in the presence of polymeric additive. The smaller molecular weight PAA is the most effective at preventing magnetite deposition.

Complementary experiments are carried out in a recirculating loop with an electrically-heated heat-exchanger tube of Alloy-800. The tube is exposed to flowing water under chemistry conditions comparable to those used during bench-top experiments. A laser profilometer is used to measure the thickness of the deposited magnetite at the end of each run. The use of polymeric dispersant is efficient at mitigating magnetite deposition. Again, the smaller molecular weight PAA is the most effective. A numerical model is developed to assist in the interpretation of the results from the laser profilometer.

Due to its agglomerating effect on magnetite, one can conclude little about the effect of FFA on magnetite deposition.

ACKNOWLEDGEMENTS

First and foremost, I would like to express my sincere gratitude to my supervisor Dr. Derek Lister for welcoming me in his research group and for making this project possible. Thank you for your trust and for all the knowledge and skills I have acquired.

I am very thankful to all the persons that help me completing this thesis. Dr. Piti Srisukvatananan, Dr. Noel Kippers and Dr. Kittima Khumsa-Ang for your expertise and your help in the lab, Keith Rollins and Adon Briggs for your availability in the shop, and Carl Murdock for the logistic support. It has been a pleasure working with you during these past few years.

I am also grateful to Atomic Energy of Canada Limited for helpful discussions, the Natural Sciences and Engineering Research Council of Canada and the CANDU Owners Group for funding, and BK Giulini for providing a commercial FFA product.

Thank you to the fellow graduate students I have been rubbing shoulders with all this time. I will miss the friendly atmosphere of the UNB Nuclear Group.

Finally, my thoughts and gratitude go to the friends that have transformed my stay in Fredericton into a memorable experience, Chutima, Sarita and Nich.

Table of Contents

List of Tables

List of Figures

Nomenclature

Magnetite Cluster Model

R	Alloy-800 tube radius
r_0	Idealised magnetite cluster radius
θ	Magnetite cluster position in relation to the tube centre, the top of the tube corresponding to the position $\theta = 0$
θ^*	Spacing angle; angle separating two magnetite clusters belonging to the same plane
$h(\theta)$	Height of the shadow projected by a magnetite cluster while it is being illuminated by the laser
l_{min}	Closest neighbour distance; smallest distance separating the centre of two magnetite clusters

Fingertip Model

R	Bare fingertip diameter
d_0	Bump diameter, or bump base width
h_0	Bump height
θ	Magnetite cluster position in relation to the tube centre, the top of the tube corresponding to the position $\theta = 0$
θ^*	Spacing angle; angle separating two bumps belonging to the same plane
h_{ora}, h_{red}	Approximated bump height deducted from the orange and red fingertip scan results
h_0^{ora}, h_0^{red}	Adjusted bump height used for final calculations

1.0 INTRODUCTION

The secondary side circuit of nuclear power plants, which uses water as a working fluid, transports energy from the steam generators to the turbine to generate electricity. Despite the use of protective chemistry, the secondary side coolant water can be corrosive for some low corrosion resistant elements, such as carbon steel piping. Metal oxides, which form at the metal-coolant interface along the secondary side circuit, are transported by the coolant water and may deposit in sensitive areas, such as in the steam generator. This acts like a trap for impurities as only a negligible portion is entrained with the vapour phase out of the steam generator. The accumulation of oxide particles induces the fouling of the steam generator on the secondary side.

Fouling has a negative impact on the overall efficiency and integrity of the power plant. Not only do deposits constitute a resistance to heat transfer, but they also threaten the physical integrity of the steam generator by promoting flow disturbances and under-deposit corrosion which can lead to tube failure and leaks of the primary coolant into the secondary circuit.

Due to maintenance, repairs, equipment replacement and loss of productivity, fouling represents a significance cost in the power generation. Therefore, fouling mitigation has been one of the main concerns for plant operators, as far as the secondary circuit is concerned. One way to reduce fouling is to reduce corrosion in the secondary

side and thus reduce the oxide colloid concentration in the steam generator feed water. In this respect, finding a coolant chemistry favourable to material preservation is critical. Chemical additives used are typically light ammoniated species, such as ammonia, ethanolamine, morpholine and hydrazine. Plant operators are now looking for compounds that could preserve the secondary side in a more efficient way, either by reducing further the corrosion rate of carbon steel piping and/or by making heat exchanger walls less attractive to oxide colloids. Additives that could play this role have been identified in previous studies. These species differ from traditional chemistry applied in the secondary side by their relatively large size. Polymeric additives Polyacrylic Acid (PAA) and Polymethacrylic Acid (PMA) have dispersing properties and could thus mitigate agglomeration and deposition in the steam generator. The Film-Forming Amine (FFA) Cetamine® has an important effect on surface properties that translate into an increased resistance to corrosion. It would then be interesting to investigate the impact FFA has on colloid deposition.

These additives are studied in four steps: zeta potential analyses on magnetite and Alloy-800 particles, surface wettability measurements carried out on Alloy-800 and carbon steel samples coated with the chemical additives of interest, and two types of fouling experiment at low pressure and low temperature. In bench-top fouling experiments, ribbons of Nichrome immersed in a suspension of magnetite are heated electrically. Deposition is analysed photographically and with scanning electron microscopy (SEM). Complementary experiments are carried out in a stainless steel recirculating loop with a vertical glass column as test section. An electrically-heated heat-

exchanger tube of Alloy-800 is mounted in the top of the column and exposed to flowing water under the chemistry conditions of the bench experiments but under flow-boiling heat transfer. A laser micrometer/profilometer indicates the thickness of the deposited magnetite at the end of the run. Finally, a numerical model is proposed to refine the laser micrometer data interpretation.

The objectives of this work are to investigate the impact of additives on the deposition of magnetite onto heated nickel alloy surfaces and perform surface analyses that would help in the fouling test result interpretation.

2.0 LITERATURE REVIEW

2.1 Industrial Context

2.1.1 Nuclear Power Plant

In Pressurized Water Reactors (PWR), the coolant water is boiled in a heat-exchanger called a steam generator and the produced steam is used to spin a turbine and generate electricity. The steam is then condensed and sent back to the steam generator as shown in Figure 1. This water and steam loop, called secondary loop ("Feed-water" and "Steam" in Figure 1), is coupled with a primary coolant loop, which provides the heat necessary for steam generation, and a tertiary loop that removes the heat out of the condenser during steam condensation. The primary coolant is heated in the reactor core where it is in contact with the fuel assemblies. The sustained fission chain reaction occurring in the reactor core produces heat which is removed from the core to the steam generator by the primary coolant ("Heat Transport System" in Figure 1). The tertiary loop is connected to a cold water source, which can either be sea water, fresh water, or an intermediate cooling circuit connected to a cooling tower.

Since the late 1950s Canada has developed a series of reactor designs, called CANadian Deuterium Uranium (CANDU) reactors. The main features of CANDU reactors are the use of heavy water in the primary loop and of natural uranium in the fuel assemblies. Most of the other commercial nuclear reactors around the world use light

water as the primary coolant and enriched uranium in fuel assemblies. Reactors using heavy water as a moderator can achieve a sustained fission chain reaction with natural uranium. Light water on the other hand, absorbs too many neutron during the neutron moderation process to be used with natural uranium. Therefore, PWRs using light water moderator need to be fuelled with enriched uranium to compensate for the increased neutron loss due to light water absorption. Another feature specific to CANDU reactors is the possibility of on-load refuelling that allows the operator to keep the reactor running during fuel replacement and thus prevent costly plant shut-downs, such as those required for light water PWR refuelling

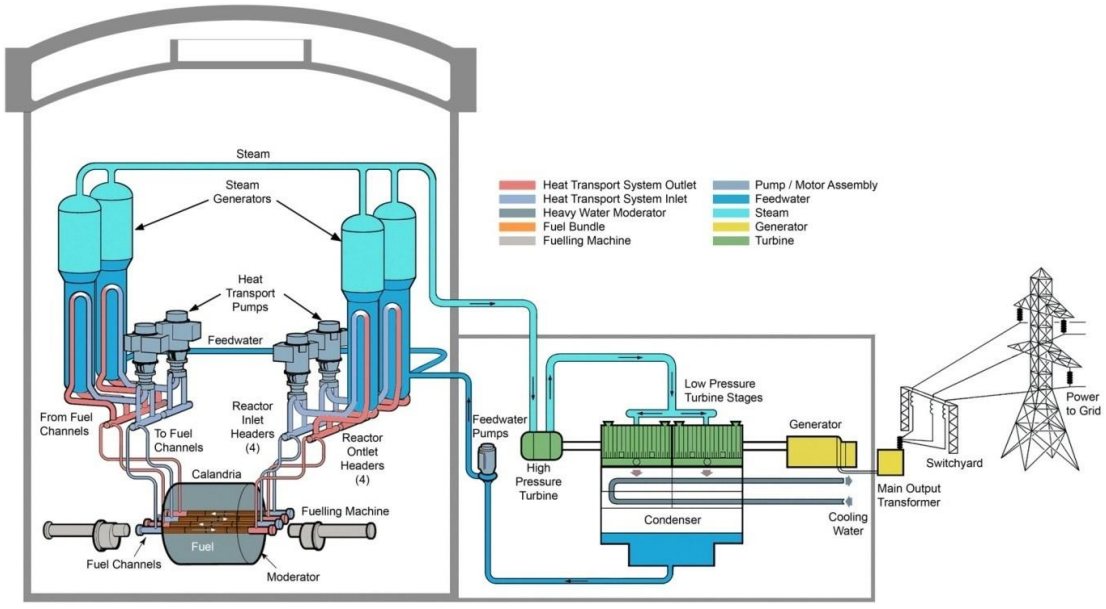

Figure 1 Simplified diagram of the CANDU 6 heavy water reactor (courtesy of AECL)

Canadian and Indian organisations are the only two manufacturers of commercial Pressurized Heavy Water Reactors (PHWRs) for electricity production. India has developed its own CANDU-derivatives industry after the acquisition of CANDU technologies from Canada in the early 1970s.

Although PWR and PHWR primary circuits have many differences in terms of design and operation conditions, their secondary circuits are similar. Therefore, in spite of the focus made on CANDU systems, the conclusions drawn in this study may reasonably be extended to any steam generating circuit with similar chemistry conditions.

2.1.2 Steam Generator

In all CANDU reactors, steam generators are composed of vertical U-tube bundles inserted inside shells (Figure 2). The primary coolant circulates inside the tubes, while the secondary coolant removes the heat from the outside of the tubes. The tube bundle is supported by tube support plates and anti-vibration bars are installed at the top of the tube bundle to maintain the tubes as steady as possible. The steam generator has a major importance in a nuclear power plant. From an economical and operational point of view its role is to produce steam as efficiently as possible. From a safety point of view, it is needed to continuously cool down the reactor core and prevent overheating of fuel assemblies. The tube bundle also constitutes a barrier between the radioactive primary coolant and the non-radioactive secondary coolant. A tube failure would induce a spread of radioactive species into the secondary side circuit which could then represent a health hazard for employees working on the supposedly non-radioactive secondary circuit.

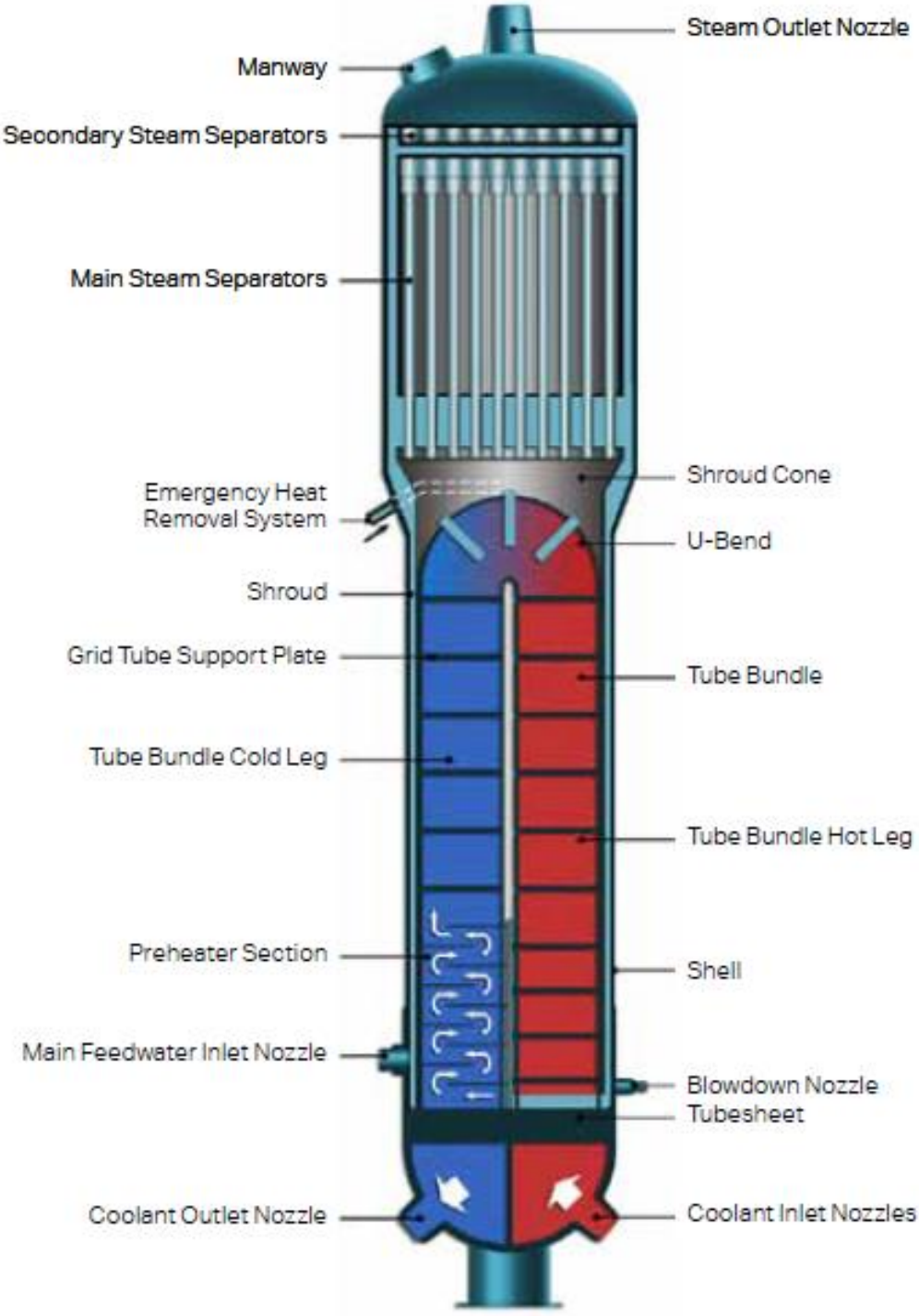

Figure 2 Cross-section drawing of a steam generator (courtesy of CANDU Energy)

The containment barrier constituted by the steam generator tubes is all the more critical as it is exposed to extreme conditions. Indeed, the tubes have to withstand very high pressure and temperature on the primary side and boiling and two-phase flow on the secondary side. Moreover the tubes are exposed to two different chemistry conditions, from the primary and secondary coolant water, and thus need to present very good corrosion resistance for both of them. However harsh these conditions might be, the tube has to be as thin as possible to minimize the heat transfer resistance.

In the case of the CANDU reactor, the material typically used for steam generator tubes is an austenitic alloy called Alloy-800 or Incoloy 800. It is a high nickel and chromium alloy that shows very good corrosion resistance and strength at high temperatures. Different types of Alloy-800 with various composition are manufactured, the composition ranges used in the nuclear industry are presented in Table 1 and are designated as "nuclear grade" or Alloy-800 NG. The high nickel content makes the material more noble, i.e. more resilient to corrosion, by increasing its equilibrium potential while the chromium is responsible for the formation of a protective and regenerative oxide layer at the surface of the alloy that offers a better protection than iron-based oxide layers such as those observed on carbon steel surfaces [1, 2].

Table 1 Chemical **c**omposition of Alloy-800 NG [3]

Fe	Ni	Cr	Ti	Al	Si	Cu	Mn	C	S
≥ 39.5	≥ 30 ≤ 35	≥ 19 ≤ 23	≥ 0.15 ≤ 0.6	≥ 0.15 ≤ 0.6	≤ 0.1	≤ 0.75	≤ 0.15	≤ 0.1	≤ 0.015

2.1.3 Corrosion in the Secondary Side

Corrosion is a reaction that turns a material into a more stable form, for a given environment, from a thermodynamic point of view. Corrosion is synonymous with degradation and destruction as some critical properties of the materials can changed dramatically, such as strength [1]. Corrosion implies charge and mass transfer between the corroding metal and its surrounding environment, which then needs to be conductive. In this respect, the electrolyte coolant water is a medium that can sustain corrosion processes at the coolant-metal interface. Considering that the composition of the coolant as well as the metal surface characteristics (topography, adsorption of chemical species, etc.) have an impact on charge and mass transfers, the control of the coolant chemistry is crucial to minimize corrosion and preserve the integrity of the plant components. Table 2 presents the temperature conditions inside a CANDU cooling system along with the chemistry and materials used.

Table 2 CANDU secondary side characteristics at Darlington power station [4]

Number of tubes per steam generator	4663
Thermal output per steam generator (MW)	664
Tube material	Incoloy 800
Tube outer diameter (mm)	15.9
Inlet/Outlet primary coolant temperature (˚C)	309/265
Steam temperature (˚C)	265
Feed-train heaters	Low/High pressure: Stainless steel Reheater: Carbon steel
Condenser tubes	Titanium
Secondary chemistry	All Volatile Treatment (AVT): Ammonia, Hydrazine

Light volatile amine species, such as morpholine and ammonia are typically chosen to increase the pH in the secondary coolant. Table 2 emphasizes the importance of volatility of species used for chemistry control as it is necessary to maintain a protective chemistry all along the water-steam circuit [4]. Among other reasons, alkalinity of the coolant is required as it guarantees a low iron solubility in the water [5].

All the main alloy constituents used in the secondary circuit (iron, nickel and chromium) are subjected to corrosion; however, kinetic factors differ between constituents as well as the characteristics of the resulting corrosion products. Metals that form a dense and adherent oxide layer separating the underlying bare metal from the corrosive liquid will present a significant reduction of their corrosion rate. This is the case of most austenitic steels that form a protective chromium oxide layer on their surface. However, porous and/or brittle oxide layers will not prevent efficiently the diffusion of species between the bare metal and the liquid resulting in a corrosion rate reduced only to some extent. In particular, carbon steel, which typically corrodes into magnetite Fe_3O_4 in reducing conditions, is not always efficiently protected by its oxide layer [2]. Nevertheless, due to its better resistance to Stress Corrosion Cracking (SCC) [1, 6] as well as for economic reasons, carbon steel is preferred to stainless steel for the secondary circuit piping. SCC is a mechanically assisted form of corrosion that may initiate when a metal is both exposed to a corrosive environment and tensile stress. These mechanical forces, which can either be due to applied load or residual stresses, may result in the initiation and the propagation of cracks despite the compliance of typical design stress [1, 7].

In general, when put in contact with the water coolant under the normal power plant operating conditions, the iron constituting carbon steel turns into magnetite at the metal-water interface, or at the metal-oxide interface if the oxide layer is already formed, according to the following reaction [8, 9]:

$$3\mathrm{Fe} + 4H_2O = Fe_3O_4 + 4H_2 \qquad \text{Equation 1}$$

Other iron oxides, such as hematite and lepidocrocite, that form inside the secondary circuit presumably do so when the coolant conditions are disrupted, during reactor shut-down operations for instance [9]. The formation of an oxide layer reduces the corrosion rate of the metal by providing a barrier to mass transfer processes required for corrosion to occur. However, it is still possible for species to diffuse through the magnetite layer.

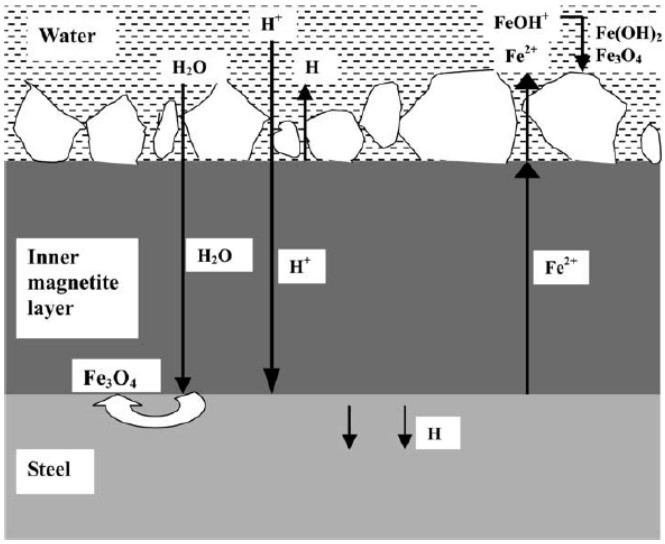

Figure 3 Schematic view of the double oxide layer and its formation mechanism on steel at high temperature [10]

In particular, water and hydrogen atoms can reach the bare metal surface under the oxide layer and the corrosion process may continue. The resulting metal ions may then turn into magnetite as described by Equation 1, or diffuse through the oxide layer as shown on Figure 3. Upon reaching the oxide layer surface, ferrous ions typically precipitate as ferrous hydroxide (Equation 2) that can either be washed away by the water flow, or deposit onto the oxide layer. The deposited oxides then undergo further oxidation and eventually form magnetite crystals at the oxide-water interface (Equation 3, known as the Schikorr equation). Magnetite formation processes are more complex than described above. In particular, magnetite may be produced by different reactions from those in Equation 2 and Equation 3, not to mention that the succession of events (iron diffusion, precipitation, deposition, oxidation) may also vary [8, 11].

$$Fe + 2H_2O = Fe(OH)_2 + H_2 \qquad \text{Equation 2}$$

$$3Fe(OH)_2 = Fe_3O_4 + H_2 + 2H_2O \qquad \text{Equation 3}$$

Typically, two different oxide layers can be distinguished on carbon steel surfaces; an inner fine-grained layer of magnetite and an outer layer formed atop the latter composed of coarse magnetite crystals. This layout is called the double oxide layer (Figure 3). The inner layer is occupying the volume originally filled by the corroded metal [8, 11].

From a heat transfer point of view, the inner magnetite layer offers a certain resistance to heat transfer, as the thermal conductivity of magnetite is lower than that of steel. By contrast, the thin porous outer layer enhances heat transfer by increasing the

contact area with the coolant and decreasing the wall superheat required for bubble nucleation. However, the positive effect of fouling on heat transfer is quickly balanced out as the dense inner oxide layer grows and the overall heat resistance becomes positive once the oxide reaches a thickness of about 10 μm [12, 13]. As a comparison, the outer oxide layer is a few micrometres thick [2, 11], but the thickness can vary depending on the coolant conditions at the wall. The porosity of the deposit will affect the heat transfer resistance as well, this latter increasing with increasing oxide layer porosity [13].

The magnetite double oxide layer is not always allowed to grow and become protective. In some areas of the secondary circuit, the coolant flow may be particularly turbulent and impose severe shear stress at the wall as well as quick pressure variations. Under these conditions the protective oxide layer is constantly disrupted and its growth impeded. Erosion, spalling and magnetite dissolution maintain a thin oxide layer on the wall, if the oxide layer exists at all, which promotes species diffusion to the bare metal surface and thus increase its corrosion rate [1, 7]. This phenomenon, called Flow-Accelerated Corrosion (FAC), is a major issue in the feed-water and steam extraction system and demands a thorough monitoring of the equipment by the operator [14].

As for austenitic steel alloys, the double oxide layer formed on their surfaces usually has a different composition. The inner layer is enriched in chromium spinel, such as chromite $FeCr_2O_4$, and the outer layer is composed of ferrite containing some nickel [2]. Austenitic and nickel alloys have thinner, more compact and more adherent oxide films compared to the oxide layer formed on carbon steel, which explains the greater protection conferred by the former [7].

As well as using resistant alloys to mitigate corrosion, plant operators can maintain a chemistry free of oxidizing agents in the coolant water. The low-pressure condenser exposes the secondary circuit to potential leaks and contamination by the cooling water. Among other impurities, dissolved air and salts can have serious consequences for the feed-water system and the steam generator. The steam generator is particularly vulnerable as impurities will accumulate in the water phase during evaporation and may lead to acidic conditions in stagnant areas such as crevices or within porous deposits; conditions that may result in high corrosion rates in localized areas. As for oxygen concentration, hydrazine, a volatile amine, is used as an oxygen scavenger [2, 12]. However, there will always be the possibility of corrosion through the process of hydrogen evolution at the metal interface. Besides, it is not desirable to remove dissolved oxygen completely from the coolant as it would induce the dissolution of protective magnetite layers on carbon steel surfaces. Actually, there are evidences that injecting an appropriate amount of oxygen in the coolant could decrease the corrosion products release rate from carbon steel piping due to the formation of a more protective oxide diffusion barrier [15]. Oxygen injection is particularly interesting in mitigating FAC as it could entail the formation of an oxide layer adherent enough to stifle FAC sites. However, high oxygen concentration have to be avoided in the steam generator as it would increase the risk of localized corrosion of the tube bundle.

2.1.4 Consequences of Fouling in the Secondary Side

Fouling in the secondary loop affects heat exchangers such as those belonging to the feed-water heater train from the condenser to the steam generator, this latter being particularly affected. Indeed, at the stage of evaporation of the coolant, the colloids are trapped in the steam generator which leads to an increase of the oxide concentration in the coolant water, thus increasing the particle deposition rate on the steam generator surfaces. Tube bundle fouling inside a steam generator is illustrated by Figure 4 that depicts fouled tubes on the left-hand side of the picture corresponding to hot legs while cold legs, on the right-hand side, are relatively clean. Fouling of heat exchangers by corrosion products can have serious implications for the operation of the plant, both in terms of the loss of efficiency and the deterioration of the equipment.

Notable direct consequences include [2, 3]:

- Heat transfer efficiency deterioration
- Hydraulics modifications: head loss increase through heat-exchangers, flow induced vibrations due to tube support plate blockages
- Under-deposit corrosion

The two last points are the most problematic as they threaten the integrity of heat exchangers. Flow-induced vibration may enhance fretting, wear and fatigue corrosion of steam generator tubes, especially at the contact points of tubes and anti-vibration bars or tube support plates. Fouling may also increase the coolant speed in some areas and induce FAC of carbon steel supports [9].

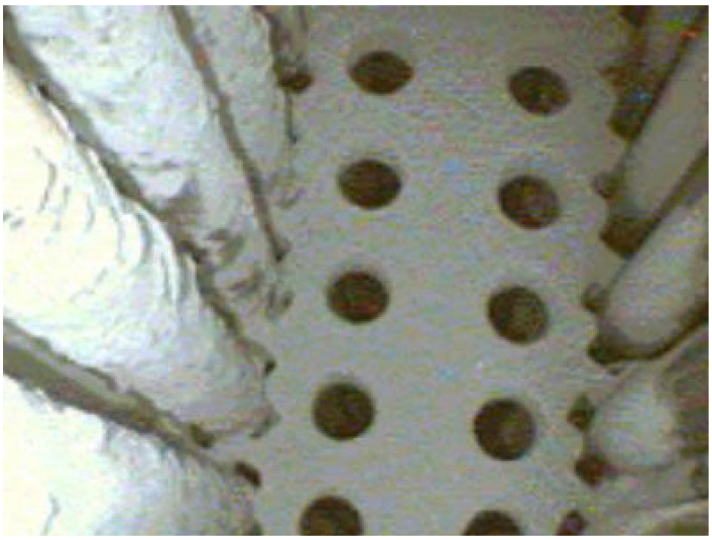

Figure 4 Picture of PWR steam generator tubes maintained by a tube support plate [16]

Tube support plate blockage occurs when corrosion products plug the space between the tube support plate and the tube. Under-deposit corrosion can lead to tube pitting and SCC, particularly within the sludge pile at the steam generator bottom plate [3].

A fouling mitigating measure widely used is the continuous purge, or blowdown (see the "Blowdown nozzle" on Figure 2) of steam generators. Purge lines are meant to remove a small portion of the coolant water in the steam generator to prevent the corrosion product concentration to increase above a certain value. In order to maintain a high heat to electricity conversion ratio, the flow rate of the purge line, which is a heat loss, is kept low compared to the steam generator feed-water line debit. Typically the purge ratio is 200 to 400 fold smaller than the feed-water flow and it removes about 15% of the total corrosion product mass transported inside the steam generator by the feed-water line [9]. Curative methods, such as water lancing and chemical cleaning, are also used.

Nevertheless, unlike the mitigation measures presented previously, these operations require the plant shutdown and are thus costly due to the loss of income from electricity generation.

The choice of the pH control agent has an influence on the deposit rate of corrosion products inside heat exchanger under flow boiling condition. As mentioned earlier, a typical protective chemistry requires an alkaline pH using volatile ammoniated species. To mitigate the deposition rate, an amine with a low surface coverage is preferable. A suggested reason is a modification of surface charges that result in electrostatic forces applied to colloids as will be explained later in this study [17, 18]. By performing magnetite deposition tests onto an Alloy-800 surface and under flow boiling and alkaline pH conditions, McCrea [19] concluded that cyclohexylamine is the most efficient at mitigating fouling followed by ammonia and morpholine.

2.2 Fouling in the Secondary Cooling Loop

Fouling can be classified into different categories depending on the processes involved in the deposit formation. Six forms of fouling have been identified by Epstein [20], among which the following categories can be encountered inside the secondary side:

- Particulate fouling, when colloid particles carried by the flow deposit and accumulate on a heat transfer surface.

- Precipitation fouling, when dissolve metal precipitates into one of its oxide forms in the vicinity of the wall, or inside the pores of an already existing oxide layer, and attaches to the surface.
- Corrosion fouling, when the oxide layer growing on a wall results from the corrosion of this same wall. Unlike the two previous categories, no corrosion product transport by the coolant water is required for corrosion fouling to happen.

The present study only focuses on particulate fouling.

Corrosion fouling is particularly severe at the contact between steam generator tubes and Tube Support Plates (TSP) when the latter are made out of carbon steel, which is the case in the early CANDU stations [4]. Indeed the oxide layer growth on the TSP will impose stress not only on the steam generator tube that may lead to denting and SCC issues [3], but also on the TSP itself which may speed up the carbon steel corrosion rate.

Concerning precipitation fouling, it occurs at places where the coolant water experiences an increase of the dissolved iron concentration or a decrease of the iron solubility. A noticeable case of precipitation fouling is the one occurring in flashing areas such as those generated by steam generators' tube support plates as shown in

Figure **5**. Upon passing through the holes of tube support plates, the coolant water experiences a local pressure decrease. Providing that the coolant temperature is high enough, the water vaporizes. This phenomenon is called flashing. While the water evaporates, the dissolved iron concentration increases. If the dissolved iron concentration reaches the iron solubility in the coolant, iron oxides precipitate and may deposit on the

tube support plate or within an already existing oxide layer. Flashing can eventually lead to tube support plate blockage and thus to flow-induced vibrations [16].

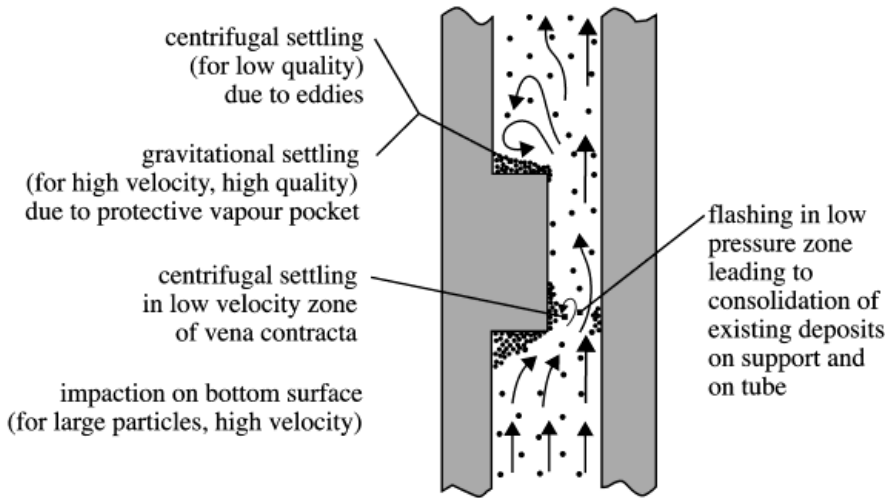

Figure 5 Proposed support fouling mechanisms [21]

2.3 Particulate Fouling

Particulate fouling of a heating surface exposed to a colloidal suspension has originally been described mathematically by Kern and Seaton [22] as a deposition and a removal component in an equation (Equation 4) that describes the evolution of the deposit mass m_f per unit area on the heating surface.

$$\frac{dm_f}{dt} = \Phi_d - \Phi_r \qquad \text{Equation 4}$$

In Equation 4, Φ_d is the particle deposition flux and Φ_r is the particle removal flux. This model has then been developed [23-27] and is now understood as a three-stage mechanism that takes into account the consolidation of the deposit and distinguishes two different sub-steps, transport and attachment, within the deposition stage:

- Deposition
    - Transport
    - Attachment
- Re-Entrainment (or removal)
- Consolidation

The deposition stage occurs in two successive steps. Particles are first transported to the vicinity of the heating wall before going through the attachment step where a physical bond is created between particles and the heating surface.

Prior to attachment, particles have to be brought to the vicinity of the heating surface. This requires the crossing of the viscous sub-layer that separates the turbulent flow region of the boundary layer and the wall. In the turbulent region, particles may be transported toward the wall by turbulent eddies. As the particles approach the viscous sub-layer, hydrodynamic effects diminish and diffusion starts to have more influence on particle displacement. Once particles reach the viscous sub-layer, particle displacement through the sub-layer is mainly supported by diffusion processes until the distance to the wall is small enough for surface interactions to become significant.

Diffusion processes imply two main phenomena:

- Brownian diffusion, which is the chaotic displacement of particles due to molecular excitation.
- Thermophoresis diffusion, which is due to the high temperature gradient at the surface of heating surfaces which repels particles.

This transport description is valid for submicron particles only. As particles get heavier, the diffusion effects tend to be overwhelmed by inertia effects. In fact, particles may accumulate enough inertia from momentum transfer within the turbulent region to go through the viscous sub-layer and reach the vicinity of the wall without relying on diffusion processes. However, the present study focusses on colloid particles, i.e. less than 1µm in diameter, for which diffusion phenomena are typically required to reach the wall.

However small particles may be, some hydrodynamic forces still affect their movement within the viscous layer [2, 27]:

- The drag force applied to any object in movement in a viscous fluid. It is opposed to particle displacement.
- The drainage force which results from the energy required to drain the thin layer of fluid which is trapped between the wall and the approaching particle.
- The lift force, also known as the Magnus effect, which applies to rotating particles when the rotation axis is orthogonal to the surrounding flow direction. The resulting force is orthogonal to both rotation axis and incoming flow lines, and the force direction is dictated by the particle rotation direction.

The attachment step is controlled by forces that become significant in the vicinity of the wall. These forces are electromagnetic interactions and they become dominant at a distance of about 10 nm from the wall. Surface charges and London-Van der Waals interactions are mainly responsible for the attachment process [27]. The latter interaction is always attractive, while the former one can be either attractive, repulsive or null depending on the sign of the charged surface.

- The London dispersion force, or London van-der Waals force, is an attractive force that originates from the interaction of induced dipole moments. Electric dipoles are created by the distribution of electron clouds in metal or oxide lattices. Once formed these dipole moments, which may be very short-lived, induce dipole moment formation in neighbouring lattices. The electric dipoles formed on both particle and wall surfaces may then interact with each other and generate an attractive electrostatic force [23, 28].
- Immersed in an electrolyte solution, solid interfaces are covered with ions. On the solid surface, a net charge of a certain sign builds up on a plane called the inner Stern layer, while a net charge of the opposite sign builds up in the solution on a plane facing the solid interphase, the outer Stern layer. These latter charges correspond to solvated ions and are called “counter-ions”. These two oppositely charged layers are called the electrical double layer [28]. In reality, all the counter-ions are not directly facing the charges of opposite sign on the solid surface, but are distributed within a thicker layer of solution where the ratio of the counter-ions concentration over the total ion concentration gradually decreases as the distance to the interphase increases as shown

on Figure 6. In this diagram, active silicon sites $SiOH$ should be replaced by $FeOH$ sites to make the explanation relevant to the present study. The counter-ions required to compensate for the charge carried by the inner Stern layer, also called surface charge, and that are not contained in the outer Stern layer, lie within the diffuse layer. The two Stern layers are tightly adherent to the solid surface while the counter-ions belonging to the diffuse layer are loosely attached, particularly those that lie outside the surface shear plane, as they can be easily be washed away by the flow and replaced by other counter-ions from the solution. By adsorbing and/or reacting with the surface, ions such as hydronium (H_3O^+) and hydroxide (OH^-) modify the composition of the Stern layers. The pH thus has a major influence on the surface charge as it dictates its sign. The pH at which the net charge contained in the plane of shear has its sign changed is called the isoelectric point (IEP). The IEP is also highly dependent on the material constituting the surface and on the possible species adsorbed on it.

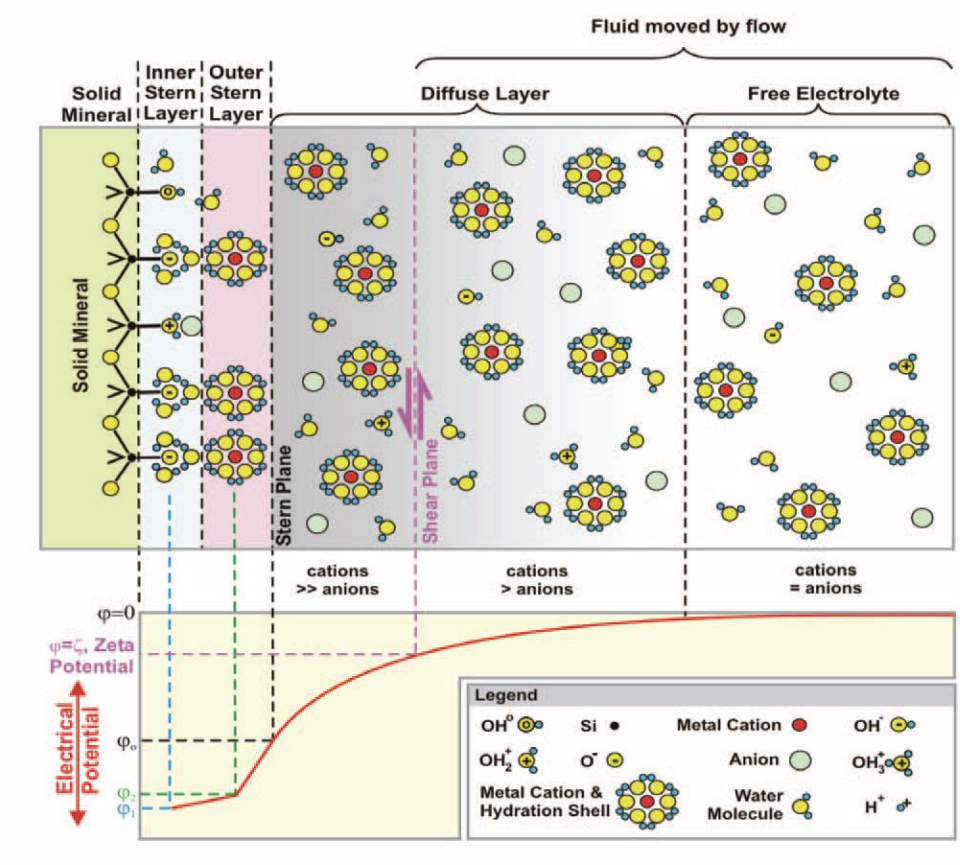

Figure 6 Schematic view of the electrical double layer at a solid-electrolyte interphase in the case of a silicon-based solid [29]

In a practical way, if two surfaces made of the same material and thus carrying the same surface charge get close enough to each other, two configurations can be distinguished depending on the pH of the solution:

i. If the pH is higher or lower than the IEP of this particular material, the surfaces will carry the same net charges and an electrostatic repulsive force will appear and repel the surfaces from each other. The two solids will have to overcome an

electrostatic potential barrier to approach close enough for the attractive London energy to allow physical contact. Typically, the deposition rate will be limited by the rate of attachment in this case.

ii. If the pH is close enough to the IEP, the surfaces net charge will be small and the electrostatic repulsive force negligible. In that case the attachment process is dictated by the attractive London Van-der Waals force and the deposition rate is thus controlled by the rate of transport.

Similarly, if two surfaces made of different materials or coated with different species do not have the same IEP, a solution with a pH above the higher IEP, or below the lower IEP, will result in the creation of a repulsive electrostatic force. Attachment will require the overcoming of an energy barrier as in the case described above in paragraph (i.). A solution pH included within the two IEP values will lead to opposite charges on the two surfaces and will generate an attractive electrostatic force adding up to the attractive London dispersion force. Finally, if the pH is such that the surface charge on one of the surfaces is close to zero, surface interaction will be attractive as explained previously in paragraph (ii.). As a consequence, pH control in a nuclear power plant is critical to mitigate agglomeration and deposition of corrosion product particles. The surface potential at the plane of shear, called the zeta potential (Figure 6), is usually used instead of the surface charge to describe electrostatic interaction between surfaces.

Oxide mineral surfaces in aqueous media are covered with hydroxyl groups that belong to the inner Stern layer and react with the solution chemistry. These surface sites, $metal - OH$, having an amphoteric behaviour, are sensitive to the pH of the solution [30]

and partly dictate the solid zeta potential. For instance in the case of an iron base solid (magnetite or Alloy-800) immersed in water in which the pH is above their IEP, the solid reactive sites $FeOH$ become negatively charged FeO^- sites by combining with hydroxide ions. The second electric layer is then formed by positive hydrated species (such as hydronium or ammonium ions). For a pH lower than the IEP values, hydronium cations may combine with surface sites to form positively charged $FeOH_2^+$ sites and negative hydrated species (such as hydroxide ions) form the second electric layer [30, 31]. Similar phenomena, i.e. the formation of negatively (respectively positively) charged surface sites for an alkaline (respectively acidic) conditions, are assumed to occur for nickel and/or chromium surface sites in the case of Alloy-800 and Nichrome [30].

The removal stage, or re-entrainment, involves both chemical and mechanical processes and breaks down into three categories: dissolution, erosion and spalling. Oxide dissolution will occur if the product concentration at the oxide-coolant interphase is too low. This can be observed when turbulent eddies reach the vicinity of the wall and dilute the saturated coolant close to the oxide layer with fresh coolant from the bulk. Erosion is a particulate removal where oxide colloids are mechanically removed from the wall due to high shear stress exerted by the coolant. Spalling, which is the detachment of agglomerates from the wall, may occur when physical bonds within the oxide layer weakens and/or when a localized area of the deposit is exposed to high shear stress. This latter case may be due to turbulent bursts that have enough energy to go through the viscous sub-layer and impact the oxide layer. Re-entrainment becomes more significant as the roughness of the wall increases due to fouling. Indeed, the viscous sub-layer has a

protective effect for the oxide layer by limiting flow velocities. However, as the deposit grows and roughness increases, some parts of the oxide layer may get closer to the buffer region and thus be subjected to higher shear stress which can accentuate the three phenomena described above.

The consolidation stage, also called deposit "aging", is responsible for the strengthening of the oxide layer. It consists in the increase of physical or chemical bonds between the colloids forming the oxide layer. Precipitation of oxide within the oxide layer pores may accelerate the consolidation process. The aging stage makes the oxide layer more adherent to the wall and thus reduces the possibility of re-entrainment.

2.4 Fouling of Heat-Transfer Surfaces

The fouling mechanisms described earlier take into account the presence of a heat flux through the thermophoresis contribution. However, boiling phenomena need to be addressed as well since they have a significant impact on corrosion product deposition. Different fouling behaviours are observed depending on the heat transfer mode.

2.4.1 Fouling under Single Phase Heat Transfer

Under single phase heat transport, although thermophoresis repels particles from the wall, elevated temperatures enhance Brownian diffusion and eddy diffusivity, which could be responsible for particle transport through the boundary layer [32, 33]. According to Basset [34], forced convection single phase heat transfer under neutral pH shows an increase of about 50% of the deposition rate of magnetite on Alloy-800 compared to isothermal

conditions during the early stage of fouling. The study [34] investigates fouling transport steps by maintaining a neutral pH for which magnetite particles and Alloy-800 present opposite surface charges. The absence of an electrostatic energy barrier leads to a transport controlled deposition. Turner [35] reported that the deposition of magnetite on Alloy-800 is transport-controlled in the pH range 6.5 to 8.3, whereas it is limited by the attachment step outside this range when particles and wall carry like charges. Magnetite deposition under single phase forced convection seems to be uniform, with denser magnetite spots on surface imperfections such as scratches or pits [34].

2.4.2 Fouling under Boiling Heat Transfer

Among numerous other studies, investigations carried out at the UNB Nuclear Group have shown the importance of boiling on fouling processes [25, 26, 34, 36]. Indeed, the presence of bubbles on the heat transfer surface disturbs the protective laminar sub-layer which enhances particle flux to the wall. Unlike under single phase heat transfer, magnetite deposition under boiling heat transfer seems to be closely related to the heat flux [35]. Turner [18] reported a magnetite deposition rate increase of an order of magnetite between single-phase forced-convection and sub-cooled boiling.

2.4.2.1 Boiling Phenomena in the Secondary Side

Depending on the water temperature at the wall and the heat flux passing through the heating surface, various boiling phenomena may be observed.

A first distinction can be made between sub-cooled and saturated boiling. Sub-cooled boiling occurs when the bulk coolant temperature is below its saturation point, in which

case the vapour bubbles that form on the wall condense once they leave the thermal layer and eventually collapse. If the thermal layer is not thick enough, bubbles may also condense and collapse while still attached to the wall. Saturation boiling is observed when the bulk coolant temperature is equal or superior to the saturation temperature. The vapour bubbles can then detach from the wall and mix with the bulk coolant without collapsing.

A second distinction comes from the motion within the coolant. When the fluid motion is due to natural convection and buoyancy-driven bubbles, boiling phenomena are referred to as pool boiling. When the fluid motion is due to a combination of buoyancy and external forces that entrain the bulk, it is forced convection boiling. This latter is the boiling type encountered within the secondary circuit as the coolant is always in motion with mass flow rate varying between 800 and 1000 kg/s in CANDU 6 reactors [9].

Heat transfer modes in water-steam systems also need to be addressed to describe boiling phenomena. The four different modes of heat transfer in pool boiling are listed below by increasing wall temperatures [37].

- Free convection: vapour bubbles may form but fluid motion is determined by free convection effects.
- Nucleate boiling: the vapour bubbles impact on heat transfer increases with the temperature, evolving from isolated bubbles to jets and columns up to a point where the liquid can no longer wet the surface properly as too much vapour is produced.
- Transition boiling: an unstable vapour film forms on the surface, oscillating between nucleate and film boiling.

- Film boiling: the heating surface is completely covered with a vapour blanket. Heat transfer occurs via vapour convection and thermal radiation absorption by the water

The boiling curve of water under atmospheric pressure [37] is presented in Figure 7. Nucleate boiling occurs at low wall temperature, which is about 5˚C above the saturation temperature, and is characterized by a heat flux that increases with increasing wall temperatures. At a wall temperature of about 30˚C above saturation, the heat flux reaches a local maximum, called the critical heat flux, and nucleate boiling turns into transition boiling. In this new regime, the heat flux decreases with increasing wall temperatures until the temperature is high enough to maintain a stable steam film on the surface of the heating wall. This last regime, called film boiling, is characterized by an increasing heat flux with increasing wall temperature. In the film boiling regime, the value of the critical heat flux is reached for a wall temperature of about 1000˚C above saturation.

Transition and film boiling are less efficient in transferring heat than nucleate boiling and thus should be avoided in heat transfer system where steam production is not required [37].

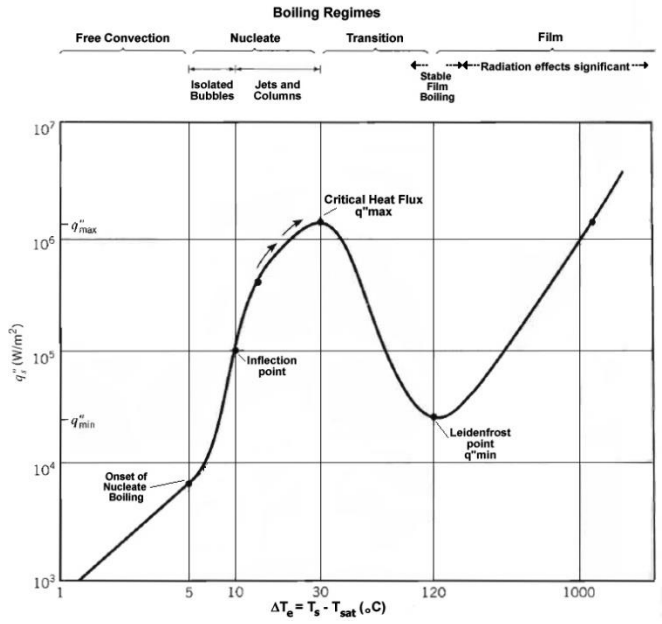

Figure 7 Pool boiling curve for saturated water under atmospheric pressure [37]

Inside the steam generator, the coolant is maintained in motion by the combining effect of pressure gradient and buoyancy, therefore heat is transferred through forced convection and the mode of heat transfer differs from pool boiling. As the coolant is brought to the top of the tube bundle it goes through the following heat transfer modes, successively [37]:

- Single phase liquid forced convection
- Two-phase sub-cooled flow boiling
- Two-phase saturated flow boiling

Typically, a steam generator tube bundle produces wet steam that is sent through steam separators (Figure 2) to extract the saturated steam needed to drive the turbine.

2.4.2.2 Impact of Boiling on Particulate Fouling

Nucleate flow boiling heat transfer has proven to be favourable to particulate fouling. Basset [34] showed that over the minimum heat flux required for the onset of nucleate boiling, the heat flux has a strong influence on magnetite deposition rate on Alloy-800 under neutral pH conditions. While the heat flux has little effect on the deposition rate under non-boiling heat transfer, the deposition rate follows the square of the heat flux from about 65 kW/m² to 240 kW/m², the former heat flux corresponding to the onset of nucleate boiling. Turner [17] has observed a sharp increase of the deposition rate of magnetite onto Alloy-600 when switching the heat transfer mode from single phase forced convection to sub-cooled flow boiling.

A feature of fouling under nucleate boiling heat transfer is the formation of a ring-shaped deposits centred on nucleation sites as shown on Figure 8. This picture was taken after 10 hours of exposure under forced convection sub-cooled boiling heat transfer. The presence of boiling heat transfer seems to introduce new corrosion product transport and attachment phenomena that lead to an increased deposition rate. The assumed major effects of boiling on particulate fouling are listed below.

- Increased colloid concentration at the wall
- Pumping effect
- Microlayer and particle trapping
- Turbulences and bubbles collapse

Metal oxides, being non-volatile, are not entrained with the vapour during boiling. Therefore, the vicinity of the heating surface is characterized by high colloid and dissolved metal concentrations which promote particulate and precipitation fouling.

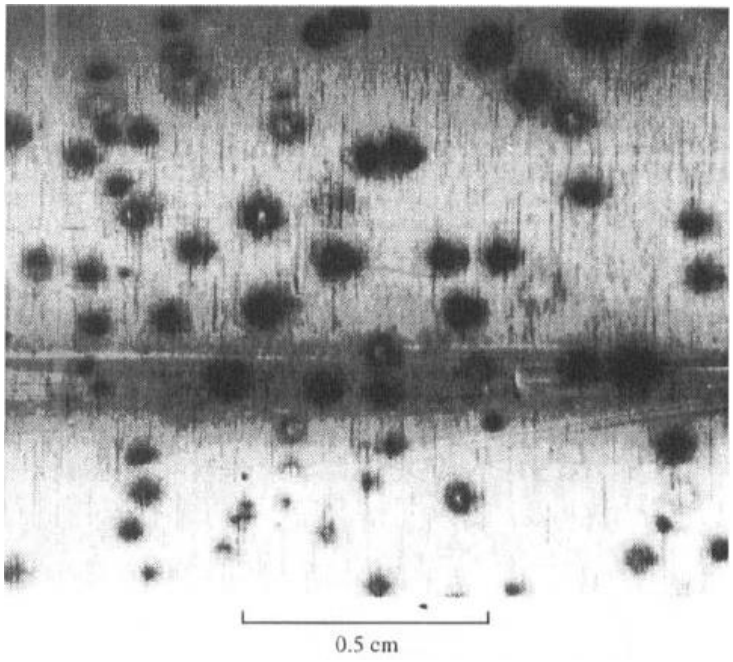

Figure 8 Picture of magnetite deposits on an Alloy-800 heater [34]

Bubbles' pumping effect has been explained as the movement of the fluid surrounding the vapour bubble upon detaching from the solid surface [38, 39]. Hamburger [39] has described bubble departure in nucleate pool boiling. Being covered by a superheated boundary layer, the detaching bubble carries along a certain amount of superheated liquid away from the heating surface. The vacant nucleation site is then immediately filled with relatively cooler fluid from the bulk carrying additional corrosion product particles close

to the wall. It was also reported that Pliolite® particles of about 50µm in suspension are attracted to nucleation spots resulting in a particle concentration increase around bubbling sites [38]. These two consequences of the bubble pumping effect tend to increase the particle flux toward nucleation sites and could explain partially the deposit pattern seen on Figure 8.

The existence of a microlayer of water between growing vapour bubbles and the heating wall, as it is shown on Figure 9, has been proven [40]. Utaka et al. [41] measured its thickness and showed that it increases linearly with the distance to the bubble centre and can measure around 40µm when the vapour bubble reaches its maximum radius. Cooper and Lloyd [40] distinguished several stages in the microlayer lifetime. The microlayer forms once the bubble starts to nucleate. As the bubble grows and the microlayer evaporates, the dry patch at the centre of the nucleation site expands. Once the bubble reaches its maximum radius and starts to rise, water is drawn back into the microlayer from outside the nucleation site and progressively make the microlayer and the dry patch recede until the bubble detaches completely. The superheated boundary eventually reforms over the vacant nucleation site. It is believed that the microlayer is responsible for the formation of ring-shape deposits under boiling heat transfer [38, 42]. Particularly during the dry patch expansion stage when the microlayer evaporates, forcing the colloids it contains to deposit on the wall. Metal oxide precipitation is likely to occur during the microlayer evaporation. Finally, Basset [43] observed that magnetite particles can be trapped by the bubble vapour-liquid interface. These particles may then slide along

the interface toward the dry patch and deposit on the wall during the microlayer evaporation.

The formation and departure of bubbles from the heating wall is also responsible for disturbances in the laminar viscous layer. This causes the layer to lose some of its protective nature due to the pumping effect described earlier as it provides an easier alternative to particle transport than the diffusion barrier that colloids have to cross under non-boiling conditions. Nucleate boiling creates turbulence downstream of nucleation sites, therefore a rising bubble may be responsible for an increased particle flux toward the wall outside its own nucleation sites. On the other hand, under sub-cooled boiling heat transfer, the collapse of bubbles in the vicinity of the wall may induce stress on the existing deposit and facilitate removal processes.

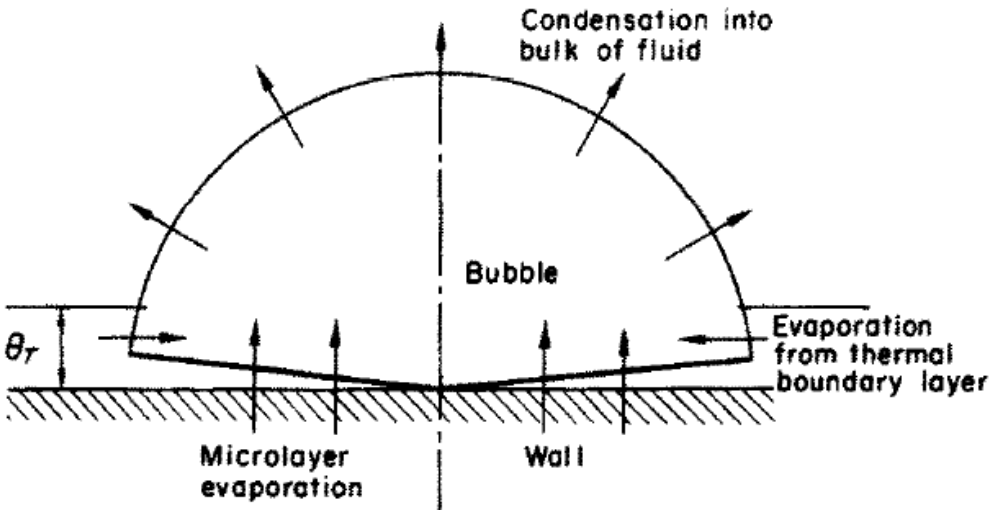

Figure 9 The micro-layer model during bubble growth [40]

2.5 Chemical Additives

Chemical additives have been investigated for their beneficial effect on fouling. Unlike the amine species mentioned previously, the main role of these additives is not to raise the pH to protect the equipment but to modify corrosion product interactions. Typically, chemical additives need to be used along with a pH control agent. By adsorbing on walls and corrosion-product colloids, the molecules affect surface properties and could thus modify fouling mechanisms. Surface properties identified as possibly responsible for the effect of additives on fouling are the zeta potential, contact angle and steric interactions. Only the first two are investigated in the present study. Steric interactions are described for interpretation and discussion purposes.

2.5.1 Zeta Potential

The zeta potential is the electric potential arising from the formation of the electric double layer. More precisely, it is the electric potential only due to charges that travel with the particle in the fluid, i.e. charges that are contained within its shear plane [28]. The net charge present in the diffuse layer outside the shear plane is not accounted for in the zeta potential. Therefore, the net charge contained in the shear plane has the same sign as the particle surface charge but with a lower magnitude. In particular, the isoelectric point, described previously, corresponds to a null zeta potential. As the charges included within the shear plane are adherent to the particle, any electrostatic force applied to them will be transmitted to the whole particle. It is thus relevant to study the particle zeta potential to investigate electrostatic forces existing between particles, or between a particle and a wall.

Measuring the IEP is important so as to conclude on the nature of the electrostatic interaction: repulsive, attractive or null. The zeta potential gives an additional piece of information that is the amplitude of the interaction.

A common way to measure the zeta potential of a sample is to apply an electric potential between two electrodes immersed in a colloid suspension. If the colloids' zeta potential is not null, the particles will then be attracted by one of the two electrodes depending on the sign of their zeta potential. The isoelectric point is the pH of the sample for which the velocity of colloids within the electric field is zero on average. Practically, the pH at the IEP is interpolated using two values of pH giving opposite zeta potential values.

A literature review report on IEP values [44] indicates that the $pH_{25°C}$ at the IEP for magnetite particles is commonly found between 6 and 7. Little seems to be published on the zeta potential of Alloy-800. The only IEP value of Alloy-800 found in the literature is given by Khumsa-Ang [45] as shown in Figure 3. The IEP value of Alloy-600, measured using the streaming current method, is given as well since this metal composition is chemically close to Alloy-800's. The IEP value of Alloy-800 given by Turner et al. [24] is an estimate based on the deposition rate of magnetite particles on an Alloy-800 surface at various pH. Since the zeta potential of magnetite particles was known, the IEP of Alloy-800 could be estimated around a $pH_{25°C}$ value of 8.

Table 3 IEP values of magnetite, Alloy-800 and Alloy-600 found in various studies

Studies	IEP of magnetite ($pH_{25°C}$)	IEP of Alloy-800 ($pH_{25°C}$)	IEP of Alloy-600 ($pH_{25°C}$)
Turner et al. [24]	6.5	8	___
Turner et al. [17]	5.8 – 6.7	___	4.1 - 4.7
Khumsa-Ang [45]	___	4.4	___
Hajdú et al. [31]	7.9	___	___

The IEP results presented above were obtained using strong acids and bases, such as hydrochloric acid and potassium hydroxide, as pH control agents. Turner et al [17] showed that the use of amines, which are weak bases, lead to an increase of the IEP. This is explained by the incomplete dissociation of amines in water that enhance adsorption of protonated amines on surfaces, thus increasing the particle's zeta potential. In particular, the IEP of magnetite was shown to shift from 6.7 in the absence of amines, to 7.2, 7.6 and 8.4 in the presence of a 50 mM solution of morpholine, ethanolamine and ammonium hydroxide respectively.

2.5.2 Contact Angle

In a two-phase system, molecules or atoms that form the interphase within each phase are submitted to interfacial tensions. Indeed, due to their position, interactions of these molecules or atoms with their immediate surrounding is different from what is observed in the bulk. This results in the creation of an interfacial free energy, or interfacial tension, which is by definition "the minimum amount of work required to create unit area of the interface or to expand it by unit area" [28].

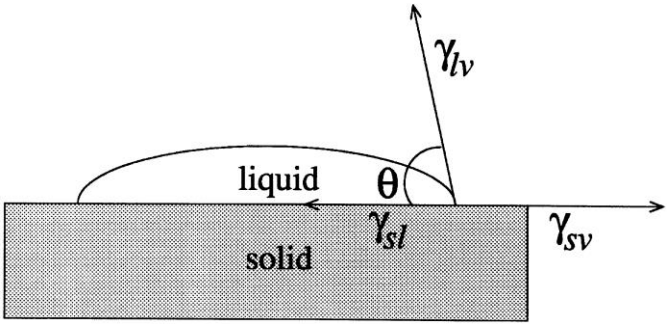

Figure 10 Schematic of a sessile-drop contact angle system [46]

A simple way to assess interfacial tensions is to measure the contact angle created by a drop on a solid surface (Figure 10). This contact angle is actually the result of the interactions occurring at three different interphases, solid-liquid, liquid-gas and gas-solid. The equilibrium of the drop on the solid surface is described by the Young equation (Equation 5) linking $\gamma_{lv,}$ γ_{sv} and γ_{sl} (respectively the interfacial tensions of the liquid-vapour, solid-vapour, and solid-liquid interfaces), and the angle θ that forms the drop at the contact of the solid [46].

$$\gamma_{lv}\cos(\theta) = \gamma_{sv} - \gamma_{sl} \qquad \text{Equation 5}$$

In the case of an interface between a gas and a condensed phase, molecular interactions due to the gas phase are negligible compared to those of the condensed phase and the interfacial tension is thus dictated by the properties of the condensed phase only. The term "surface tension" is used in this case as the interface is then a solid or liquid surface [28]. In the assumption that the chemical additive that may be present on the metal surface does not diffuse in the liquid drop during the contact angle measurement, it may be assumed

that the liquid surface tension, which is known in the case of pure water, remains constant. According to Equation 5, the measurement of the contact angle is then proportional to the difference of interfacial tension of the solid with the gas and the liquid phase.

The equilibrium between the three phases mentioned above also appears during boiling when vapour bubbles form at the heating surface. Although these two situations differ on many points (temperature, relative position of the liquid and vapour phase, constitution of the liquid and vapour phase, thermo-hydraulic effects, shape of the solid surface, ect.), contact angle measurements provide qualitative information that may be useful for the interpretation of fouling results.

2.5.3 Steric Interactions

The coating of particles and walls by polymers may induce another type of interaction due to the presence of a steric barrier. Steric effects originate from the energy expended to achieve electron clouds overlapping, which occurs when atoms come too close to each other. When polymers adsorb on particles and walls, their chains extending in the surrounding fluid may form an energy barrier making agglomeration or deposition more difficult. In fact, polymer coating does not necessarily have a repulsive effect on surfaces. Two configurations have to be considered depending on the strength of the chain-solvent and the chain-chain interactions. When the former is stronger than the latter, the chain overlapping region results in an increase of the system energy and thus the interaction is repulsive, in other words a steric barrier is formed. On the contrary, when the chain-chain interaction is stronger, overlapping and desolvation of the polymer chain reduces the

system energy. Thus physical bond between surfaces will be promoted and flocculation may be observed [28].

According to previous studies [31, 47-49] additives containing carboxylic groups such as PAA and PMA, are good magnetite dispersants. Therefore it is reasonable to assume that these additives act as steric stabilizers in water rather than as flocculation enhancers. For these polymers, the repelling steric force increases with polymer chain length and polymer density on the surface [50]. However, long polymers may promote bridging between particles. Therefore, there should be an optimum polymer length that provides a maximum steric hindrance to particle attachment [28].

2.5.4 Additives of Interest

Three additives that have shown interesting properties and results are investigated in this study. A commercial unsaturated diamine film-forming amine (FFA) and the two polymers polymethacrylic acid (PMA sodium salt of molecular weight 9500) and polyacrylic acid (two versions – pure PAA of molecular weight 1800 and PAA sodium salt of molecular weight 8000), as shown on Figure 11. Polymers carrying carboxylic groups are interesting as they provide sites that can form strong chemical bonds with iron based surfaces [30, 31, 51]. As aliphatic carboxylic acids, PAA and PMA have a pK_a inferior to 5 [52] and they achieve full ionization at pH 8.5 - 9 [30]. Considering that both magnetite and Alloy-800 surfaces are negatively charged at high pH (their IEP is lower than 8), once these polymers attach to surfaces, they could mitigate agglomeration and attachment by contributing to repulsive electrostatic forces applied to approaching

surfaces. Surface chemical bonding with carboxylic groups is considered the most likely possible adsorption mechanism, and although electrostatic repulsion must occur at high pH between deprotonated carboxylic groups and the ionized surface sites, adsorption does not seem to be impeded. This latter phenomenon is not fully understood [30].

Polyacrylic Acid (PAA)		Polymethacrylic Acid (PMA)	Film-Forming Amine (FFA)
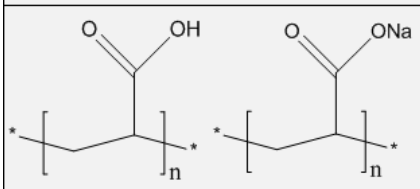		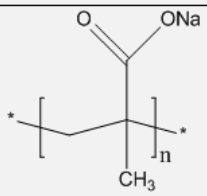	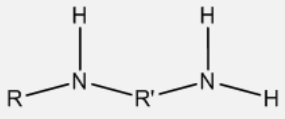
MW ~ 1800	Sodium Salt MW ~ 8000	Sodium Salt MW ~ 9500	MW = 324.6

Figure 11 Chemical additives investigated in this study; " R " and " R' " represent the two carbon chains composing the FFA molecule

The dispersant properties of PAA in the presence of magnetite particles were proven by Balakrishnan et al. [47]. The lower molecular weight PAA (MW ~ 3500 to 5000) proves to be the most efficient at preventing agglomeration, ahead of the heavier type PAA (MW ~ 27000). It was also found that, under flow-boiling and alkaline pH conditions, the lower molecular weight PAA is the more efficient at mitigating magnetite deposition on Alloy-600 for a polymer concentration of 6 mg/kg, reducing the deposition rate by more than a factor two, while the use of the heavier type PAA leads to a two-fold increase. At lower polymer concentration (0.6 mg/kg) however, the heavier PAA type shows better

deposition inhibition efficiency than the lighter one, the former decreasing the deposition rate by 55% while the latter leads to a 20% decrease. The lighter PAA molecule has shown a very high fouling mitigation efficiency at higher concentrations (e.g. a concentration of 20 mg/kg results in a deposition rate decrease of 83%). Under single phase forced convection, the use of polymer seems to increase the deposition rate of magnetite, an effect which is not yet fully understood [47].

In a study conducted under conditions similar to PWR's secondary circuit (high pressure, high temperature, alkaline and de-aerated chemistry using ETA and hydrazine), Akhilesh et al. [53] showed that the use of PAA at a concentration of 700 ppb reduces greatly the thickness of the outer oxide layer on carbon steel and Alloy-800 surfaces as well as the size of the oxide crystal composing this layer, which is probably due to the dispersant properties mentioned above. However, the presence of PAA does not prevent the formation of the inner oxide layer.

In addition to the dispersant properties of PAA, Umoren et al. [54, 55] provided evidence, using potentiodynamic polarization measurements, that the polymer exhibits a corrosion inhibiting effect on iron and aluminium under acidic conditions by retarding the cathodic hydrogen evolution reaction as well as the anodic metal dissolution. Further Electrochemical Impedance Spectroscopy (EIS) measurements proved that the charge transfer resistance at the metal interface increases in the presence of PAA, and that the polymer decreases the double layer capacitance, presumably by shielding the metal surface. This protective effect was also observed under alkaline conditions on aluminium by Amin et al. [52] and on carbon steel and Alloy-800 by Akhilesh et al. [53]. In the

former study, PAA of three different molecular weights was used (1800, 11000 and 14000 g/mol) allowing the authors to conclude that the heavier the PAA molecule, the more efficient the corrosion inhibition. Also, increasing polymer concentration increases the protection of the metal. Finally, Balakrishnan et al. [47] demonstrated the protective effect of PAA (MW 3500 - 5000) on carbon steel at high temperature and alkaline pH (using morpholine). However, the corrosion resistance of both Alloy-600 and Alloy-800 seems to be slightly deteriorated in the presence of the polymer under the same experimental conditions.

PAA degradation at high temperatures (180˚C to 350˚C) has been studied [47, 56, 57] and is believed to go through decarboxylation and chain breakdown processes, among others, resulting in the formation of small molecules, such as carbon dioxide and hydrogen, but also intermediate-size ones, acetate for instance. Generally, the higher the temperature, the faster the PAA degradation. Lépine et al. [56] emphasize the possible threat the decomposition products may constitute for the integrity of the secondary circuit. Small molecules such as bicarbonate and carbonate species could be entrained with the vapour and lead to condensate acidification which could possibly enhance turbine blade corrosion. The study also points out that the use of PAA would complicate greatly the monitoring of the coolant chemistry in power plants due to the formation of numerous new species from polymer degradation. Gurkaynak et al. [57] noticed that, under alkaline pH, PAA is stable at temperatures lower than 150˚C.

Although magnetite dispersion and deposition experiments showed mixed results in the presence of PMA [48], Nsid et al. [30] proved that it acts as an efficient dispersant

for aqueous suspensions of hematite, goethite and rutile. It appears that PMA relies on both electrostatic and steric repulsive interactions to mitigate agglomeration of coated surfaces. Besides, the dispersant efficiency increases with increasing molecular weight (PMA molecular weight tested: 1200, 8000, 15000 and 30000). Steric repulsion was assessed by measuring hematite suspension viscosity around the IEP. In the absence of electrostatic repulsing forces, agglomeration increases and thus viscosity reaches a peak at the IEP. Results show that the viscosity peak is lower, i.e. the suspension is better dispersed, in the presence of polymethacrylate than without additive. Size distribution measurements conducted on goethite suspensions at the IEP also gave evidences of the steric dispersing properties of PMA as it prevents particle flocculation and reduces particle diameter significantly (from a size distribution range of 1µm-1mm in the absence of dispersant to a range of 100nm-1µm with the heaviest PMA).

Ramminger et al. [58] showed how the use of FFA in the secondary circuit of a nuclear plant reduced the formation of corrosion products. It was reported that FFA protects the metal by creating a hydrophobic film on its surface that acts as a barrier to charge and/or mass transport. Its effect is particularly beneficial during outages and standstill operations, when moisture and oxygen ingress can lead to rapid corrosion [58-60]. Foret et al. [60] conducted potentiodynamic polarization and EIS measurements using carbon steel samples and concluded that FFA coating results in an increase of the electrochemical impedance at the metal interface and in a decrease of the anodic and cathodic current thus protecting the metal from corrosion. This protective effect was verified in corrosion experiments using neutral water containing chlorides. Monoamine

and diamine FFA types are the most efficient at protecting the metal with a corrosion inhibition of about 75%, the triamine type resulting in a 50% inhibition efficiency. The EIS results support the idea that the number of amine groups contained in the FFA molecule has an importance on the protection it confers to the metal. Indeed, measurements conducted on monoamine, diamine and triamine types FFA showed that the metal interfacial impedance decreases with increasing number of amine groups in the molecule used to coat the metal. To explain this observation, the authors suggested that the presence of numerous amine groups along the molecule carbon chain may impede the formation of a uniform and protective coating.

2.6 Magnetite

Magnetite is a form of iron oxide of chemical formula Fe_3O_4. It is one of the most common forms of iron oxide found in iron ore naturally occurring on the planet as well as the most strongly magnetic natural mineral [61]. Magnetite crystallizes in the face-centred cubic system with one third of iron atoms are ferrous atoms Fe^{2+}, the other two thirds being ferric atoms Fe^{3+}. Therefore, magnetite formula can be rewritten $Fe^{2+}Fe_2^{3+}O_4^{2-}$. This formula structure is characteristic of a class of oxides called spinel group. More precisely, its anions and cations being distributed a certain way within the tetrahedral and octahedral sites, magnetite has an inverse spinel structure. Half of the ferric ions occupy octahedral sites while the other half occupies tetrahedral sites along with all the ferrous ions [62].

3.0 EXPERIMENTAL TECHNIQUES

3.1 Magnetite Synthesis

All magnetite particles used in the present study have been synthesised using the high-temperature solid state method. This method is based on the reaction of iron and hematite powder at high temperature, according to the chemical reaction described by the Equation 6 [63]. The effect of temperature and rate of heating/cooling applied during magnetite synthesis have been investigated by Deydier de Pierrefeu [62]. According to this study, the formation of a fine spherical and homogenous powder is optimal when reactants are heated under vacuum for 12h at 600°C with a heating and cooling rate of 0.5°C/min.

Equation 6

$$Fe + 4Fe_2O_3 = 3Fe_3O_4$$

3.2 Zeta Potential Measurements

Zeta potential measurements are performed using a 1 mM potassium chloride solution. Magnetite particles are sonicated for one hour and added to the potassium chloride solution to a concentration of 100 mg/kg (ppm). The pH at 25˚C of the solution is adjusted with ammonium hydroxide or hydrochloric acid. Additives are introduced as required to the desired concentration. Zeta potential is measured using a zeta meter ZetaPlus (Brookhaven Instruments Corporation®), which determines the particle mobility between

two electrodes using a red laser and the Doppler effect. For each pH value, the arithmetic mean of twenty measurements is recorded.

Alloy-800 powder is obtained by grinding a sample of Alloy-800 tubing. The result is a very coarse powder and particles can measure up to 100 μm; however, some particles are small enough to behave as colloids and zeta potential measurements can be performed the same way as for magnetite except that the larger particles have to be allowed to sediment and leave the smaller particles in suspension. In order to obtain sufficient particles in the samples, an Alloy-800 concentration of 500 ppm is used along with an electrolyte concentration of 10 mM potassium chloride. The concentration of additives is increased accordingly to maintain the same quantity of additive per mass of particles as for magnetite samples.

3.3 Contact Angle Measurements

Interfacial surface tensions between deionized water and solid surfaces are measured by investigating the contact angle created by a drop of water on two different metals, air being the surrounding medium. The two metal samples used are a piece of Alloy-800 cut from a steam generator tube and a piece of carbon steel A106-B from a feed-water heater tube. Carbon steel A106-B contains a small quantity of chromium (0.019 wt%) that provides passivation properties to its surface [14]. The samples are polished using a grit 1200 sand paper, rinsed and wiped with acetone. When applicable, samples are then exposed for 15 minutes to a coating solution containing either the polymeric dispersants PAA(1800) or PMA(9500) at a concentration of 100 ppm or FFA at a concentration of

about 1 ppm (residual concentration measured after sample exposure). The $pH_{25°C}$ is adjusted to 9.8 using ammonium hydroxide and vigorous stirring is maintained as long as the samples are immersed. Blank samples only exposed to ammonium hydroxide, acetone and deionized water are also prepared. Just after exposure to these solutions, samples are dried with nitrogen gas, or simply wiped, and stored in a desiccator for 4 hours. The sample preparation is summarized in Table 4. Contact angles are measured using a tensiometer (Attension® Theta Optical Tensiometer). This device and the associated software provide a continuous contact angle reading after the drop has touched the metal surface. For all measurements, the contact angle value read 10 seconds after the drop has settled on the surface is recorded. To avoid corrosion issues during surface conditioning in the case of deionized water, samples are simply rinsed. To avoid deposition during drying in the case of acetone, using paper wipes is preferred to nitrogen gas. The deionized sample is wiped as well for the sake of consistency.

Table 4 Surface preparation prior to contact angle measurements

<table>
<tr><th>Sample #</th><th>Surface conditioning</th><th>Treatment</th><th>Drying</th><th>Storage</th></tr>
<tr><td>1</td><td>Deionized water</td><td rowspan="2">Sample rinsed</td><td rowspan="2">Wiped</td><td rowspan="6">Store in a desiccator for 4 hours</td></tr>
<tr><td>2</td><td>Acetone</td></tr>
<tr><td>3</td><td>Ammonia</td><td rowspan="4">Sample immersed for 15 minutes</td><td rowspan="4">Dried with nitrogen gas</td></tr>
<tr><td>4</td><td>PAA(1800)</td></tr>
<tr><td>5</td><td>PMA(9500)</td></tr>
<tr><td>6</td><td>FFA</td></tr>
</table>

3.4 Bench-top Experiments

The effect of additives on magnetite deposition during pool boiling at atmospheric pressure is estimated via a bench-top experiment that observes fouling on a thin nickel-chromium alloy (Nichrome) ribbon (dimensions: 25 μm by 1.5 mm by 30 mm) heated with the Joule effect to create pool-boiling heat transfer. Figure 12 represents the bench-top setup. All experiments last 60 minutes and are conducted in a 2-litre heated beaker containing the 30 ppm magnetite suspension suitably conditioned with additive.

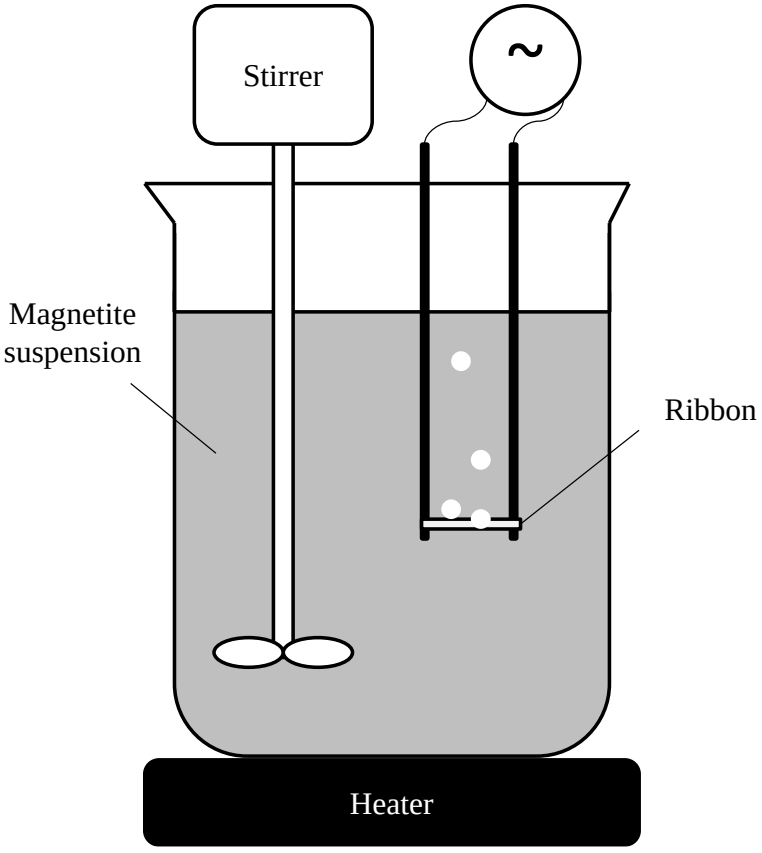

Figure 12 Simplified diagram of the beaker experiment apparatus

A beaker is filled with two litres of deionised water and the $pH_{25°C}$ is adjusted to a final value of 9.9 with ethanolamine, a relatively non-volatile base chosen to minimize evaporation losses, taking into account the pH increase or decrease due to the use of additives. The beaker is placed on a heating plate to raise the temperature to about 100°C. The nichrome ribbon is welded at both ends to copper wires acting as supports and electrical connectors (Figure 13). The ribbon assembly and a mechanical stirrer are cleaned with acetone, rinsed with deionised water and mounted in the beaker. The copper wires are connected to a Variac® and 5 amperes are passed through the ribbon, generating about 240 kW/m² on both faces of the ribbon. The start of a run begins with the addition of 60 mg of magnetite, previously agitated ultrasonically (sonicated) in deionised water for 30 minutes, to the beaker. During the run, the stirring is continuous and the bulk temperature is maintained between 99°C and 101°C. Additives are introduced in two batches, the first at 10 minutes before and the second just after the addition of magnetite.

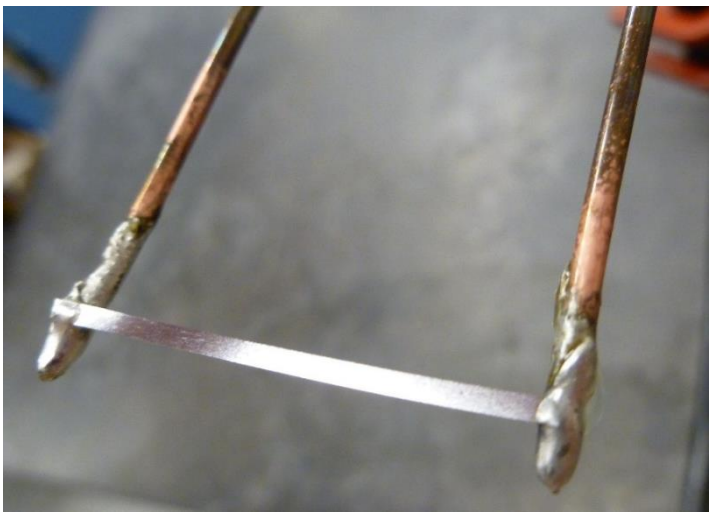

Figure 13 Picture of the Nichrome ribbon welded at the ends of two copper wires

At the end of a run, the $pH_{25°C}$ and magnetite concentration in the beaker are measured and the ribbon is detached from the copper rods for further analysis. A sample of the coolant is mixed with hydrochloric acid and sonicated at 40°C for 60 minutes to digest the magnetite. Following dilution and pH adjustment with 5N sodium hydroxide, the iron concentration in the sample is measured colorimetrically with a spectrophotometer (HACH® DR2800) and FerroVer AccuVac® ampoules containing an iron reagent. The sample iron concentration is then used to calculate the magnetite concentration in the water at the end of the run. A detailed procedure describing magnetite concentration measurements is presented in Appendix A. The ribbon analyses are mainly qualitative, comprising visual observations, SEM examinations. High-speed videos are recorded during the runs.

3.5 Recirculating Fouling Loop

Fouling experiments under sub-cooled flow boiling are conducted in a recirculating loop that has been described in detail before [26, 43]. The loop cooling water is contained in a 180-litre tank, where it is purged with nitrogen and its temperature maintained at 93°C using an electrical heater. It is pumped upwards through a 1.5-m long, 10 cm diameter vertical glass column containing a cylindrical cartridge heater, shown in Figure 14, at a flow rate of 10 litres per minute. The average water velocity in the annulus formed by the glass column and cartridge heater is about 2.2 cm/s. The coolant is then sent back in the tank.

Figure 14 Picture of the recirculating loop test section

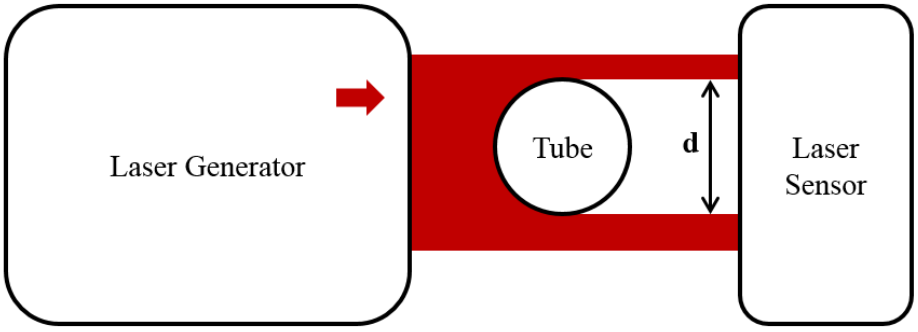

Figure 15 Simplified diagram of the laser profilometer scanning a tube of diameter ‘d’

For all the runs reported here, the $pH_{25°C}$ is maintained between 9.7 and 9.9 using ammonium hydroxide and the magnetite concentration is kept between 8 ppm and 14 ppm. Prior to addition in the loop, the magnetite is sonicated for at least 1h. Before each run, the loop water is purged with nitrogen in the tank for at least 24h. Magnetite concentration is again monitored by sampling and spectrophotometric analysis. The test section is composed of a 59 cm long Alloy-800 tube, 15.6 mm outside diameter and 12.7 mm internal diameter, containing a cartridge heater so as to generate about 110 kW/m² at the tube outer surface. Before each run it is cleaned with dilute nitric acid, rinsed with acetone and then mounted centrally in the top of the glass column.

After each run, the Alloy-800 tube from the test section is scanned with a laser profilometer (LaserLinc® TLaser 122) that measures diameters with a resolution of 25 nm; it generates a laser sheet that measures the projected shadow of any objet placed between the laser generator and the sensor as shown on Figure 15. The tube diameter can thus be measured by placing the Alloy-800 tube across the laser sheet. By comparing the diameter of the fouled tube with that of the tube after cleaning, the magnetite deposit thickness can be measured. To perform quick and consistent measurements, the tube is held in the chuck of a lathe and the profilometer is mounted on the translating platform, as shown in Figure 16. As the tube rotates typically at 100 rpm its surface is scanned helically as the platform travels at 20.3 mm/minute. The diameter measurement is continuous at a frequency of 400 measurements per second. The software TotalVu® calculates the average diameter every 40 measurements and logs the value. Between the two laser scans performed successively on the fouled and clean tube, magnetite is

removed at selected positions along the tube using ethanol and a rubber eraser. The ethanol is collected and left for total evaporation, after which the magnetite powder is recovered and dissolved in hydrochloric acid for spectrophotometric analysis. The mass of magnetite deposited on the tube per unit area is then determined. Once the magnetite is collected and prior to the second laser profiling, the tube is thoroughly cleaned with acetone and rinsed with deionized water. The loop experiments are conducted with the polymeric dispersants only.

3.6 Laser Scan Model

The laser profilometer results need to be interpreted with care. The tube diameter increase, noted Δd, due to the presence of magnetite and read by the profilometer is not necessarily the result of the presence of a uniform magnetite layer with a thickness of $\frac{\Delta d}{2}$ on the surface of the tube.

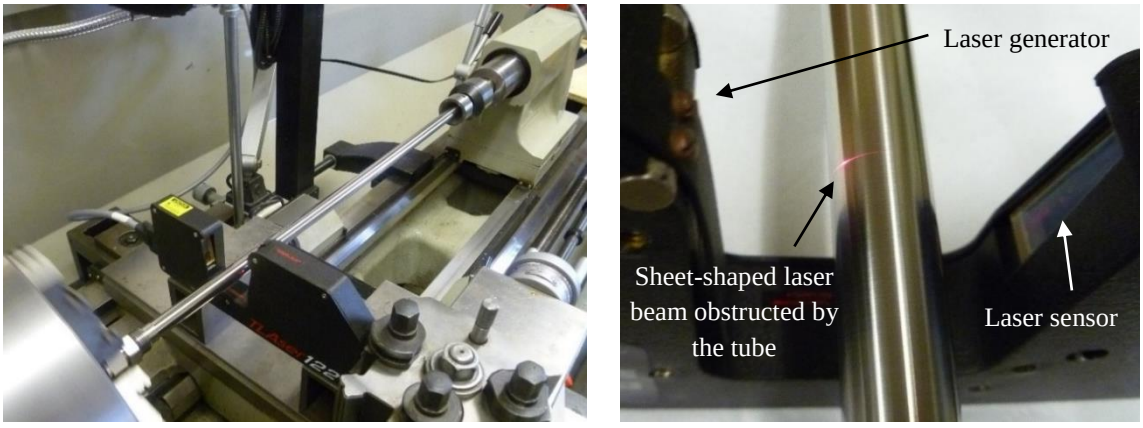

Figure 16 Tube and profilometer installed on a lathe (left); laser sheet shadowed by the tube (right)

The reason is that when the laser measures the deposit thickness at one point, the sensor might actually receive the shadow projected by the deposit at another point of the tube. As a consequence, depending on the magnetite deposition pattern, the laser measurements might be misleading to some extent. To interpret the profilometer results, numerical simulations are performed on a simplified deposit model. The objective is to find a disposition of magnetite particles on the tube that satisfies both the scan results and the measurements of magnetite deposit mass. To do so, the model assumes an idealised pattern of deposit and calculates the corresponding diameter increase and magnetite mass that would be measured if this pattern were to be scanned by the laser device.

Several assumptions are made to construct this model:

1. Magnetite particles deposit on the tube as spherical clusters of radius 'r_0' (Figure 17).
2. Magnetite clusters are regularly spaced over the tube surface thus forming a uniform microscopic deposition pattern; ring-shaped deposits are ignored in this model.
3. The clusters belong to planes parallel to each other and orthogonal to the tube axis, these planes being one cluster diameter apart (Figure 17).
4. Clusters belonging to the same plane are separated from each other by the same angle θ^*, called spacing angle, from the centre of the tube (Figure 17).
5. The laser beam width (about 0.2 mm) is much larger than a cluster diameter, thus more than one cluster plane can project a shadow on the laser sensor at a time.
6. The shadow area projected on the sensor is normalized by the laser width, giving the average diameter of the tube over the area illuminated by the laser at any time.
7. The scan is performed as if a continuously recording laser profilometer were used.

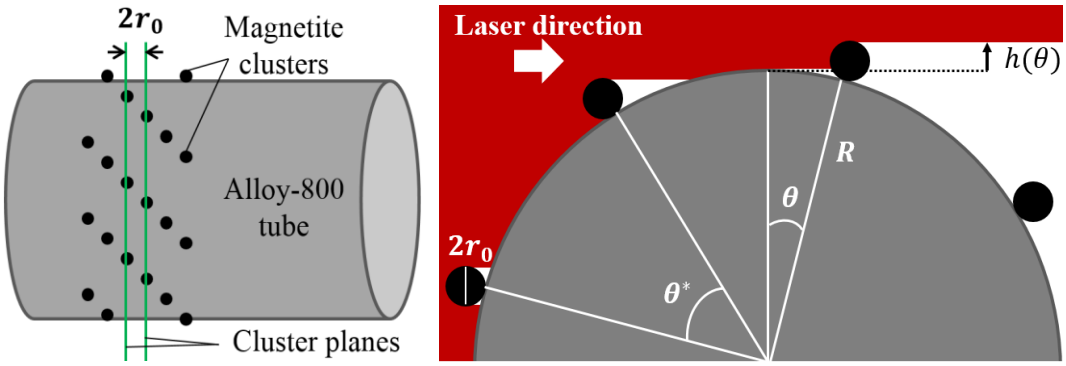

Figure 17 Magnetite cluster disposition on the tube (left); cross section of the tube of radius 'R' with clusters of radius 'r_0' on its surface (right)

As the deposition pattern is regular along the tube, the model needs only to consider one cluster plane. The arrangement of a cluster plane with respect to its neighbours does not influence the result, since the average diameter measured by the laser is calculated from the measurements made during several rotations of the tube. Indeed, whether the cluster planes are in phase or not, all the clusters of each plane are taken into account once per rotation. The study can thus focus on only one cluster plane and normalize the projected shadow by the distance separating two planes, i.e. one cluster diameter, to obtain the average height increase due to the idealised deposit. Periodicity by rotation of the tube is also exploited in the model. The shadow projected by one cluster as it progressively enters the laser field, reaches the horizon at the top of the tube and recedes below the tube horizon is the same for all the clusters in a plane. Therefore, only the path of one cluster between the positions $\theta = \frac{\theta^*}{2}$ and $\theta = 0$ is considered, θ being the angular displacement of the considered cluster in relation to the top of the tube (Figure 17).

As explained in Figure 18, the software Matlab is used to calculate the shadow produced by one magnetite cluster while it moves in the interval $[0\ ;\ \frac{\theta^*}{2}]$. For each infinitesimal angle within this range, the program calculates the vertical height $h(\theta)$ of the cluster above the tube horizon. This height is then used to calculate the extent of the shadow projected on the sensor and then the deposit thickness that would be read by the profilometer. All the thicknesses measured are averaged to obtain the tube diameter that the profilometer would have measured, were this idealised magnetite pattern scanned. The mass of magnetite per unit surface area that results from a deposition pattern such as that shown in Figure 17 is simply obtained from the size and density of clusters disposed on one plane, as well as the cluster number per tube surface area. Figure 19 and Figure 20 are presented to illustrate the two main calculation steps of the model algorithm. Both figures depict the same magnetite cluster on the tube at a certain angular position θ belonging to $\left[0\ ;\ \frac{\theta^*}{2}\right]$. The first step is to calculate the height $h(\theta)$ of the most elevated point of the cluster, taking the tube most elevated point as a reference. The height then becomes the input of a function that calculates the projected shadow area for this specific cluster angular position. The shadow of the circular cluster is converted into circular-top and rectangular-bottom projected shadow as it is assumed that other clusters placed just before or after the cluster being scanned, and on the same cluster plane, are likely to shadow the laser where the bottom-half of the scanned cluster does not. The detailed Matlab code is presented in Appendix B.

For each angle θ belonging to $\left[0\ ;\ \frac{\theta^*}{2}\right]$:

- Calculate the additional shadow height $h(\theta)$ due to the cluster at the position θ:

$$if \qquad R > \mathrm{R}.\cos(\theta) + r_0(cos(\theta) + 1) \qquad \Rightarrow \qquad h(\theta) = 0$$

$$otherwise \qquad height(\theta) = h(\theta) = R(\cos(\theta) - 1) + r_0(cos(\theta) + 1)$$

- Calculation of the corresponding shadow projected on the sensor by the cluster:

$$if \qquad height(\theta) \leq r_0 \qquad \Rightarrow \qquad \frac{Shadow(\theta)}{2} = \int_0^{\alpha(max)} \int_{r(\min)}^{r_0} r\ dr d\alpha$$

$$r(min) = \frac{r_0 - h}{\cos(\alpha)}$$

$$\alpha(max) = \mathrm{acos}(\frac{r_0 - h(\theta)}{r_0})$$

$$if \qquad height(\theta) > r_0 \qquad \Rightarrow \qquad Shadow(\theta) = \frac{\Pi {r_0}^2}{2} + 2r_0(h(\theta) - r_0)$$

- Deduction of the magnetite thickness read by the laser at the angle θ:

$$Thickness(\theta) = \frac{Shadow(\theta)}{Width}$$

$$Width = 2r_0$$

⇨ If $\theta = \frac{\theta^*}{2}$, the loop is closed. Otherwise, the loop starts again with $\theta = \theta + d\theta$.

The average thickness measured by the laser is calculated by averaging all the thickness values obtained previously.

$$Average\ Thickness = \frac{\sum_{n=1}^{n=N} Thickness(\theta_n)}{N}$$

Figure 18 Algorithm used to model the virtual laser scan

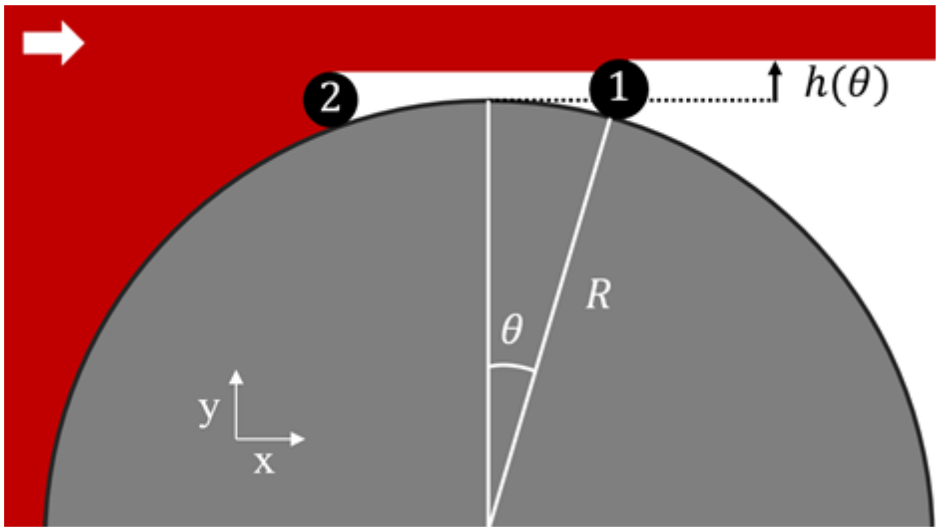

Figure 19 Clusters on the tube being scanned; *h(θ)* is the height of Cluster #1 shadow; Cluster #2 is projecting and additional shadow on the sensor

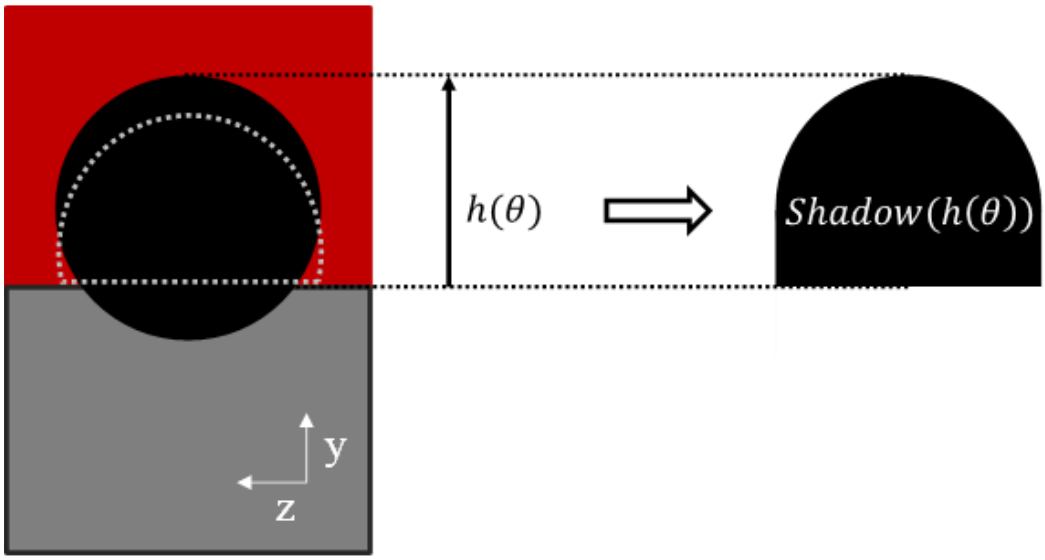

Figure 20 Different view from the configuration of the previous figure with Cluster #1 painted in black; the dotted line is the projected shadow of Cluster #2 placed behind Cluster #1

The area of the projected shadow, $Shadow(h(\theta))$ on Figure 20 is eventually divided by the width of a cluster plane to obtain the shadow height for this position θ. Averaging the shadow height values for all position θ belonging to $\left[0\ ;\ \frac{\theta^*}{2}\right]$ provides the average shadow height of the cluster plane and, by symmetry, of the whole idealised pattern.

3.7 An Attempt to Assess the Laser Scan Model Accuracy

In order to estimate the laser model reliability, a deposit pattern has to be tested by both the virtual laser scan, using the model described earlier, and the real helical laser scan. The comparison of the average tube diameter increase obtained from these two methods is a way to assess the accuracy of the model. To do so, two different rubber fingertips, shown on Figure 21, are chosen for their resemblance to the idealised deposit pattern used for the Matlab model (Figure 17).

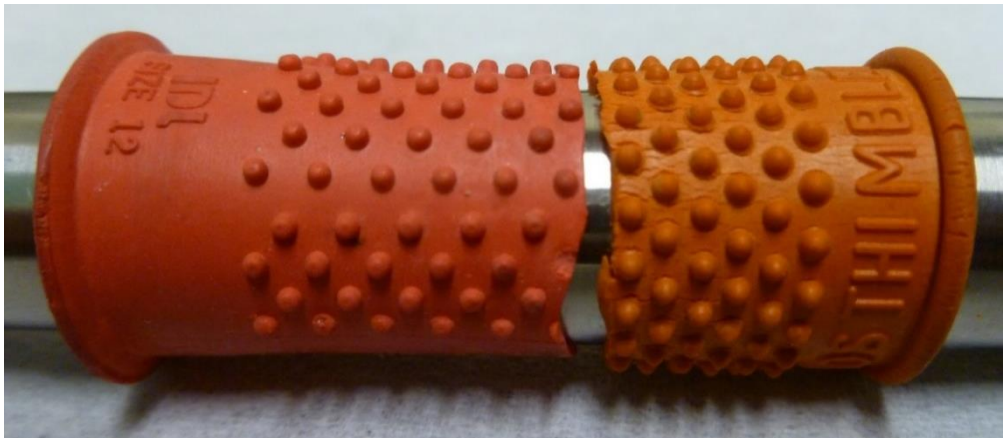

Figure 21 Rubber fingertips inserted on the tube prior to the laser scan; the orange, respectively red, fingertip is on the left, respectively right

By inserting the rubber pieces on the tube used for fouling experiments, the laser scan can be performed as described in the recirculation loop description. The spacing angle θ^* and the rubber bump dimensions can be measured on each fingertip. Therefore, the laser model can be run using the fingertips' pattern characteristics. It should be noted that the typical idealised magnetite cluster pattern is about three orders of magnitude thinner than the rubber bump pattern observed on the fingertips.

Prior to running the virtual scan using Matlab, measurements are taken on each fingertip. A Vernier scale is used to measure the bump base width (or bump diameter d_0, which should not be confused with the bump height h_0), the distance separating two bump planes, i.e. the bump plane width, and the bare fingertip diameter where no bump is on its surface. The results are gathered in Table 5. The spacing angle is simply deduced from the regular bump arrangement on each fingertip. The red fingertip circumference is carrying 7 bumps but they are gathered only on one side of the fingertip, the other side being bare, so $\theta^* = \frac{\pi}{7}$. The orange fingertip circumference is carrying 20 bumps so $\theta^* = \frac{\pi}{10}$.

Table 5 Fingertips pattern dimensions

	Red fingertip	Orange fingertip
Bump base width d_0 (mm)	1.15	1.20
Bare fingertip diameter (mm)	17.4	17.7
Bump plane width (mm)	1.6	1.9
Spacing angle θ^* (rad)	$\frac{\pi}{7}$	$\frac{\pi}{10}$

4.0 RESULTS

4.1 Magnetite Synthesis

Magnetite particles are synthesized using the solid-state method and characterized with SEM analyses (Figure 22). The magnetite particle size distribution ranges from 300 nm to 600 nm for the pure and dry powder. Its purity was established using X-ray diffraction measurements to verify the species stoichiometry.

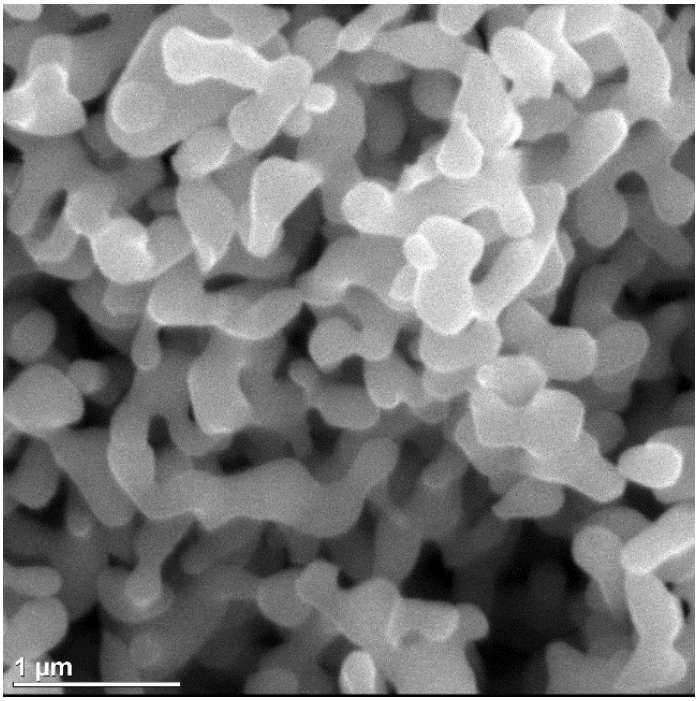

Figure 22 SEM picture of pure and dry magnetite powder

4.2 Zeta Potential Measurements

For the sake of clarity, the standard deviation of the zeta potential measurements is not shown systematically. It always appears for the samples without additive; otherwise, it is shown only if it is greater than 5 mV. Generally, the deviation is lower when PAA, PMA or FFA are used.

The zeta potential of the magnetite powder as a function of $pH_{25°C}$ is presented in Figure 23, which indicates that the IEP without additive is between 7.9 and 8.2. The zeta potential of the Alloy-800 powder as a function of $pH_{25°C}$ is presented in Figure 24, which shows the IEP without additive between 4.4 and 4.6. The zeta potentials of magnetite and Alloy-800 particles are measured in the presence of each of the four additives. The concentrations of the polymers are adjusted to correspond approximately to the same quantity of carboxylic groups per gram of magnetite or Alloy-800.

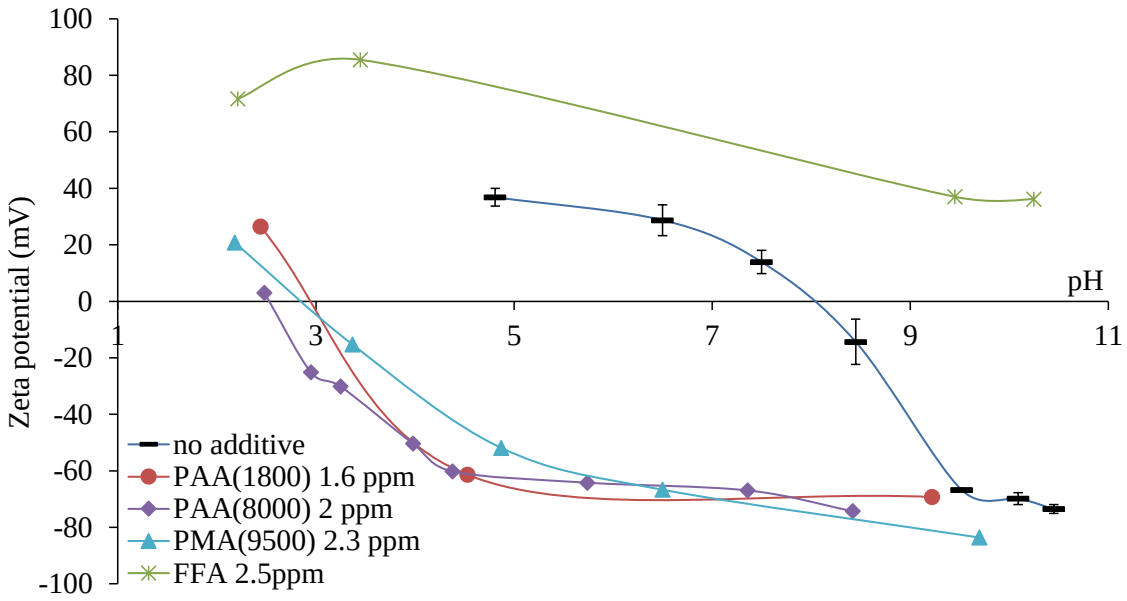

Figure 23 Effect of additives on the zeta potential of magnetite

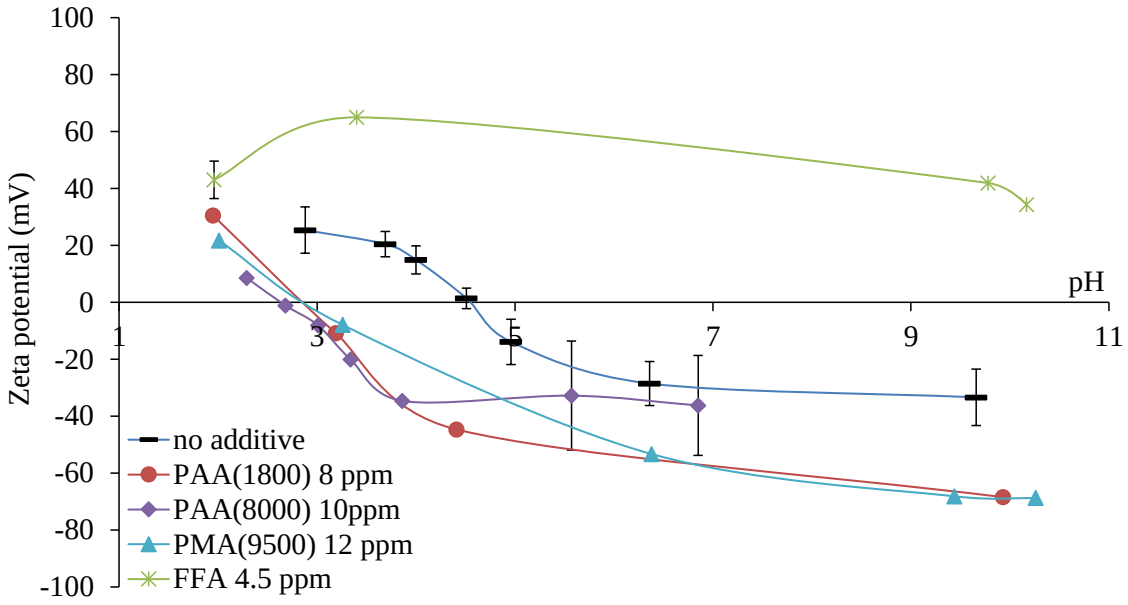

Figure 24 Effect of additives on the zeta potential of Alloy-800

In order to account for losses of FFA due to the coating of the sample cell and the immersed electrode during zeta potential measurements, FFA is added in excess in the samples. The concentration of FFA shown in Figure 23 and Figure 24 is the concentration measured after the zeta potential has been determined. FFA has the opposite effect on the zeta potential of magnetite to that of PMA or PAA. FFA increases the zeta potential of magnetite and maintains it at positive values for all pH tested. Nothing can be concluded about the IEP of magnetite in the presence of FFA except that it is outside the range pH ~2 to pH ~10. The effects of PAA and PMA on the zeta potential of magnetite are very similar. These two polymers reduce significantly the IEP of magnetite from pH 8 to about pH 3. It should be noted, however, that their effect levels off as the pH increases and reaches pH 9. It may be assumed from the present results that the difference of zeta potential with and without polymer is no more than 20 mV for the values pH 9.5-10, the

pH range of interest for the rest of the study. In the case of the IEP of Alloy-800, the effects of all four additives are similar to the ones observed for magnetite; IEP values fall between pH 2.5 and pH 3 for all three polymers, and zeta potential values at the pH of interest (9.8) are about +40 mV in the case of FFA and -70 mV in the case of polymers. The curves obtained with PAA(1800) and PMA(9500) suggest that the zeta potential values in the case of PAA(8000) at the pH of interest can be obtained by extrapolation.

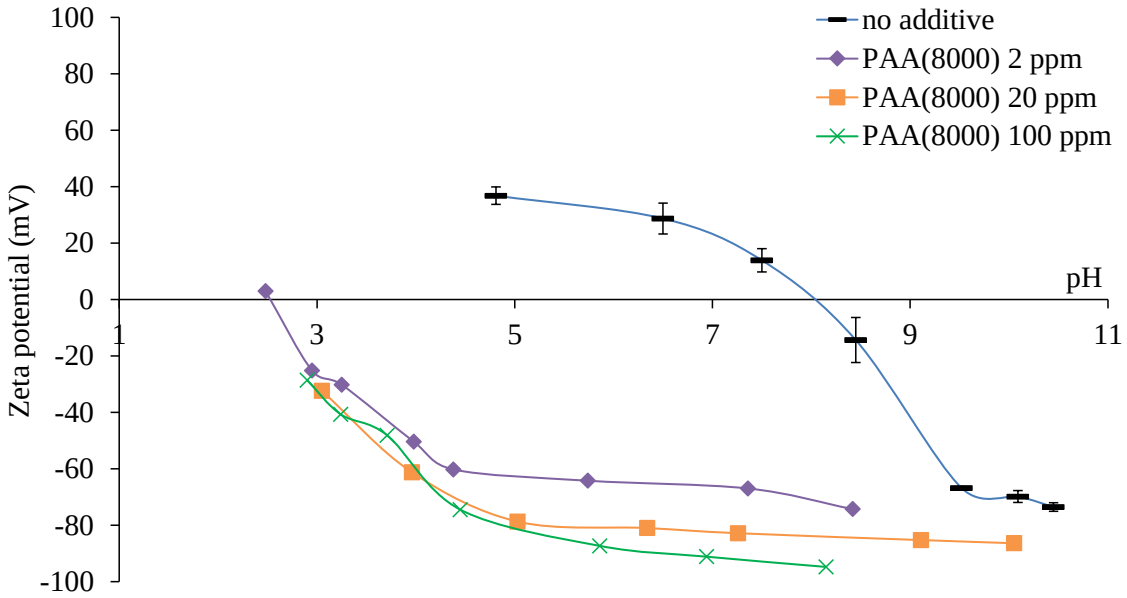

Figure 25 Zeta potential of PAA-loaded magnetite

To illustrate the influence of polymer loading on the magnetite surface, Figure 25 presents the zeta potential of magnetite in the presence of PAA(8000) at three different concentrations, 2 ppm, 20 ppm and 100 ppm. The negative charge density on magnetite surfaces is increased by increasing the PAA concentration, especially at high pH, although more measurements would be necessary to see any effect on the IEP. From the previous

results and due to the similar behavior of the different polymers on magnetite particles, it is reasonable to suggest that the loading effect of PAA(8000) on magnetite could also apply to PAA(1800) and PMA(9500). Similar polymer loading effects probably occur on Alloy-800 surfaces, too.

4.3 Contact Angle Measurements

So as to make the comparison between the two samples consistent, flat surfaces meant to receive water drops are machined on the metal sample pieces. The carbon steel tube being thick enough, a parallelepiped-shaped piece is extracted from it. The Alloy-800 sample is prepared by flattening the outer surface of the tube (Figure 26).

Figure 26 Polished metal samples used for contact angle measurements (Alloy-800 on the left, carbon steel A106-B on the right)

For each sample and each surface conditioning, the contact angles of four deionized water drops are measured and averaged. The results are summarized in Figure 27. Unlike for the PAA(1800) solution, coating solutions containing sodium salt PMA and FFA present an alkaline pH that does not require any adjustment using ammonium hydroxide. The coating of the carbon steel sample with the PMA solution results in the formation of rust on the metal surface. The rust can be observed on picture (c) in Figure 28. No visible evidence of corrosion is detected on the carbon steel samples immersed in ammonia, PAA(1800) & ammonia, and FFA solutions. Carbon steel corrosion might be due to the presence of either PMA molecules or sodium atoms from polymethacrylate addition. The presence of rust on the carbon steel sample makes the surface particularly hydrophilic as shown in Figure 27.

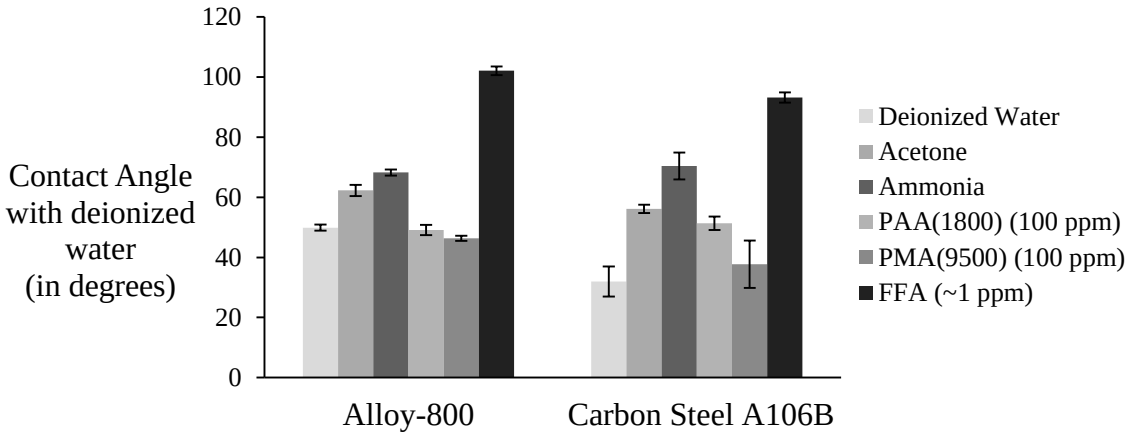

Figure 27 Contact angle of water drops on the conditioned sample surfaces; error bars indicate the measurement standard deviations

During the measurements, carbon steel samples also undergo rapid corrosion at the contact with the deionized water drops. After thirty seconds, the time required to place the drop on the sample, record the contact angle and wipe the sample, rust is already visible on the surface at the position of the drop. That might have an impact on the measurements by slowly decreasing the contact angle as the rust forms between the water drop and the steel surface. Alloy-800 samples show no trace of corrosion on their surface.

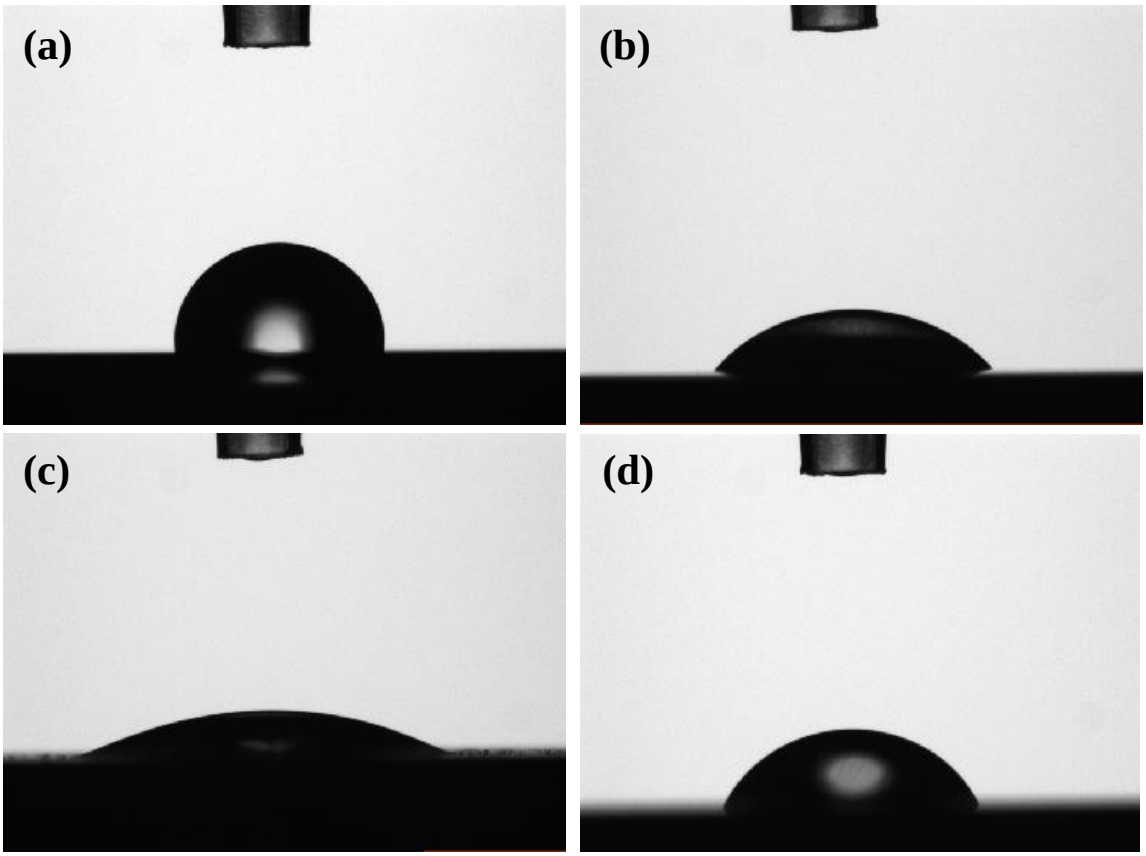

Figure 28 Pictures taken during the contact angle measurements; Alloy-800 sample is shown on the top pictures, coated with FFA (a) and PAA (b); carbon steel A106-B sample is shown on the bottom pictures, coated with PMA (c) and ammonia (d)

In spite of discrepancies observed in the case of the water and the PMA treatment, the contact angle values obtained for both carbon steel and Alloy-800 samples are similar for the other surface conditioning types. As expected, coating samples with FFA provide hydrophobic properties to surfaces characterized by contact angle close to 100˚. The ammonia treatment results in moderate contact angles included between 65˚ and 75˚ for both metals. Compared to the ammonia treatment, polymeric treatments seem to make surfaces more hydrophilic. This might be due to the presence of carboxylic groups along PMA and PAA molecules that can be solvated in aqueous solution. The explanation of the results obtained for the water and the acetone in comparison with the ammonia treatment is more difficult as discrepancies might be due to both adsorbed species (acetone and ammonia) and oxide layer characteristics.

4.4 Bench-top Experiments

The chemistry conditions used during the bench-top experiments are summarized in Table 6. At the end of all runs, the coolant pH is in the interval 9.6-9.9 and magnetite concentration is higher than 25 ppm except when FFA is used. In the latter case, particle agglomeration at the liquid-air interface and deposition on the beaker glass wall lead to a magnetite bulk concentration decrease. For each condition, two runs provide two ribbons for analysis. The run with FFA was not repeated due to the difficulties maintaining the magnetite concentration in the bulk. Accordingly, the results obtained with FFA and

presented below are for information only. Any comparison with other runs is to be done carefully.

A high-speed camera is used to record the bubble nucleation frequency and departure diameter during the runs. Note, however, that the variation of these two quantities between nucleation sites on the same ribbon and the few nucleation sites studied per ribbon add uncertainty to the data collected. The use of additive has little effect on the bubble nucleation frequency, which generally ranges from 40 to 70 bubbles/second, except when FFA is used, in which case the frequency can reach 80 bubbles/second. Also, a high concentration (300 ppm) of PAA(8000) decreases the nucleation frequency to about 30 bubbles/second. The bubble departure diameter ranges from 2 to 3.5 mm for most runs, but when PAA(8000) is used at a concentration of 300 ppm it ranges from 3.2 to 4.2 mm.

Table 6 Run conditions during the bench-top experiment

Run #	pH control	Specific Chemistry	Magnetite Concentration
1-2	ETA	No additive	30 ppm
3-4	ETA	PAA(8000) 60 ppm	30 ppm
5-6	ETA	PMA(8000) 60 ppm	30 ppm
7-8	ETA	PAA(1800) 40 ppm	30 ppm
9-10	ETA	PAA(8000) 300 ppm	30 ppm
11	ETA	FFA	30 ppm

At the end of the run, the number of deposition sites (corresponding to bubble nucleation sites) that can be detected visually is recorded and SEM pictures of the ribbon are used to measure the average diameter of deposition sites. Although uncertainty is high, Figure 29 shows a trend in the magnetite deposit diameter. Higher molecular weight polymers, PAA(8000) or PMA(9500), seem to produce larger deposition sites (up to 2.5 times larger) than when no additive is used. Runs with PAA(1800) and FFA show similar site diameters to those seen in runs without additive. Additives also have a clear effect on the number of deposition sites on the ribbon, reducing them by about 50% when PAA(8000) and PMA(9500) are used and by about 75% when PAA(8000) is used at the high concentration of 300 ppm or PAA(1800) or FFA are used. The number of deposition sites per surface area can be obtained using 9 mm^2 as the surface area of one ribbon. Because attempts to measure iron deposits on ribbons via acid dissolution and spectrophotometry produce uncertain results (traces of iron in the reagents and in the Nichrome give excessive blank corrections; colorimetric measurements disturbed by the presence of nickel and chromium species dissolved from ribbons), SEM pictures are also used to estimate magnetite coverage at deposition sites. Average coverage fractions as in Figure 30 shows that each deposition site is 10% to 55% denser when PAA(8000) and PMA(9500) are used than when there is no additive.

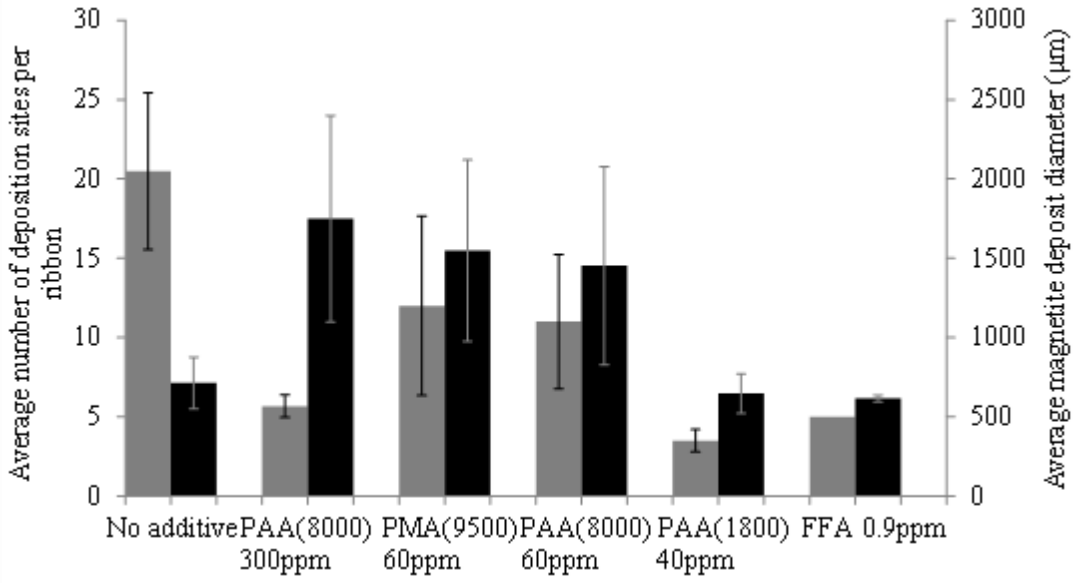

Figure 29 Average number of deposition sites per ribbon in grey; average magnetite deposit diameter in black; error bars stand for the standard deviation

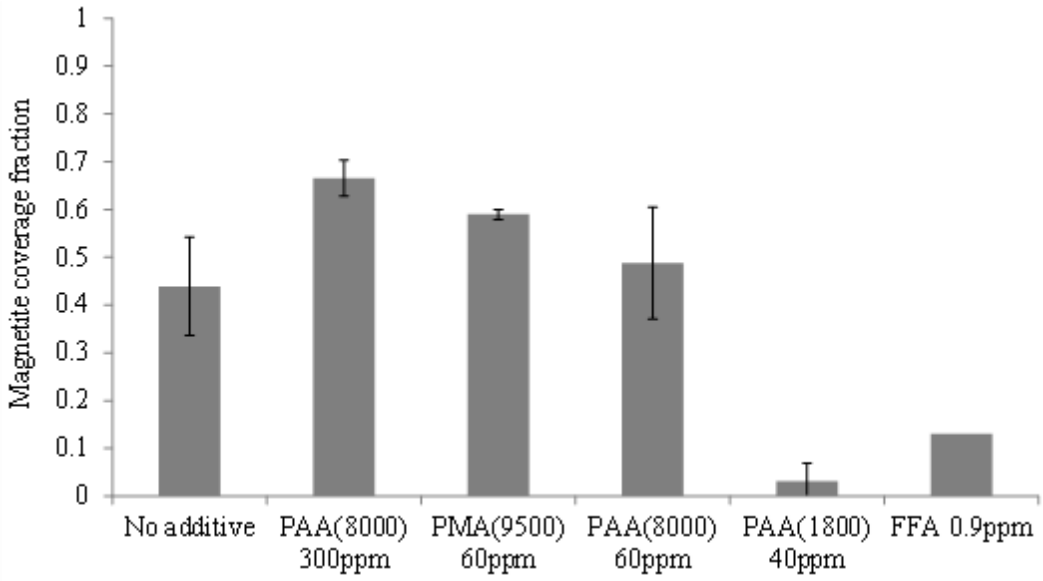

Figure 30 Effect of additive on magnetite coverage fraction at selected nucleation sites present on ribbons; error bars stand for the standard deviation

The magnetite coverage fraction is assessed as follows. On each ribbon, a dense magnetite deposit is selected and its SEM picture is analysed using the software ImageJ®. This digitizes the SEM photograph into a binary black and white picture showing magnetite particles in black and the ribbon surface in white (see a typical example in Figure 31). The total area occupied by black magnetite particles is then computed and normalized to the total area of the analysed ribbon portion to give the 'Magnetite coverage fraction' of Figure 30. The increases in density of deposition sites are probably underestimated as the image analysis method accounts for only the surface coverage and not the deposit thickness.

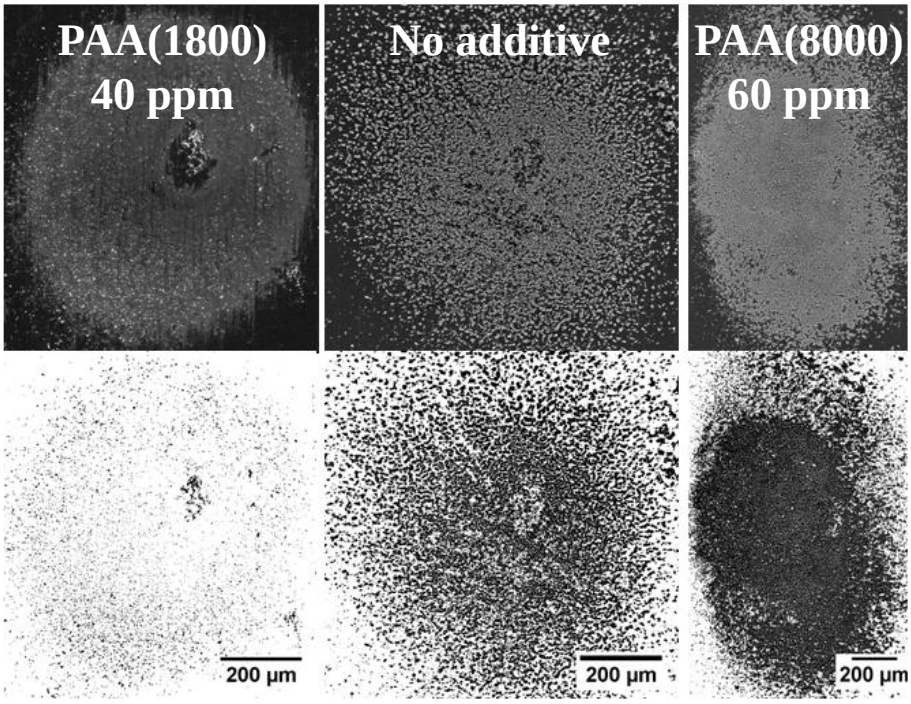

Figure 31 Original and digitised SEM pictures (respectively above and below) of bubble nucleation sites

In general, PAA(1800) reduces by about an order of magnitude the amount of deposit at each site. FFA also reduces significantly the magnetite coverage of the ribbon, but the reduction will be at least partly due to the lowered magnetite concentration during the FFA run.

All the bench-top experiments without FFA show a superheated layer of water at the bottom of the beaker, which is in contact with the heater, but no sign of bubble nucleation sites. The run with FFA, however, resulted in the generation of bulk boiling at the beaker bottom, as shown in Figure 32. It is believed that vapour bubbles trap magnetite particles as they rise to the surface. Coated with FFA, magnetite becomes hydrophobic and particles agglomerate at the water-air interface. The vortex created by the stirring eventually brings agglomerates to the beaker wall where they deposit. The intense boiling at the beaker bottom, as well as the hydrophobic properties of surfaces, are probably responsible for the dramatic decrease of magnetite concentration in the bulk.

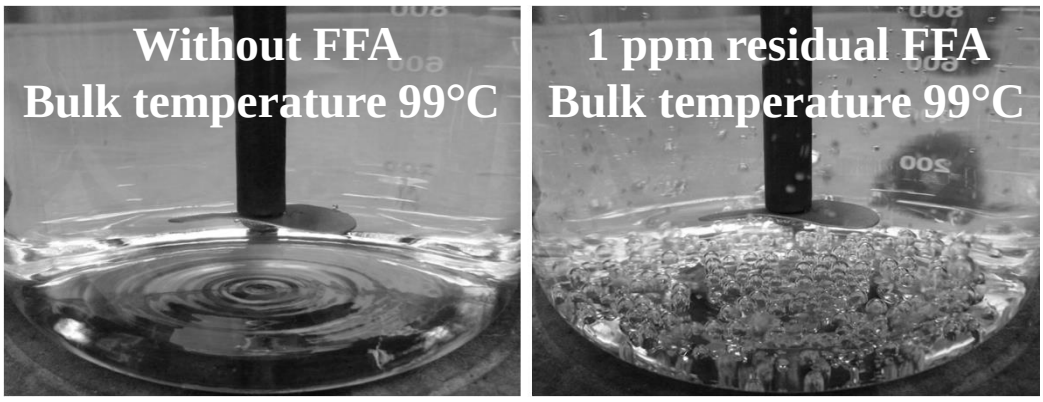

Figure 32 Pictures of the beaker bottom without (left) and with (right) FFA; heat flux is the same

4.5 Recirculating Fouling Loop

Run conditions in the recirculating loop are summarized in Table 7. The first experiments are used to study the evolution of magnetite deposit with time in ammoniated coolant and no surface-active additive. Three runs of different duration provide the magnetite deposit mass results shown in Figure 33, which conform to results from previous experiments carried out by McCrea [19]. However, those experiments were conducted under bulk boiling conditions and thus results need to be adjusted to the sub-cooled boiling conditions of the present work. To do so, another result of McCrea's work is used. Indeed, the same study highlights a proportionality relation between magnetite deposition rate under sub-cooled boiling and bulk-boiling (i.e. deposition for the latter case is about 3.75 times higher than for the former), during the early stages of an Alloy-800 tube fouling. This coefficient is used to adjust deposition results obtained under bulk boiling conditions and alkaline pH (9.5 to 10) using ammonium hydroxide. The magnetite deposition mass results, adjusted to the sub-cooled boiling condition, is presented in Figure 33 under the label "McCrea (2001) – Adjusted".

For the remaining fouling tests of the present study, run duration is set at 50h. For each of the two runs with additive, PAA(1800) and PMA(9500), a blank run is performed without additive but with the same Alloy-800 tube and cartridge heater assembly. When applicable, the polymers are added to the loop once the magnetite concentration has reached the target value of about 10 ppm. PAA(1800) and PMA(9500) are used at concentrations of 20 ppm and 30 ppm respectively to reach a carboxylic group density of about 2.8 moles per gram of magnetite in the water.

Table 7 Run conditions in the recirculating loop

Run #	Tube #	Duration	Chemistry
1	Tube 1	50h	No additive
2	Tube 2	25h	No additive
3	Tube 3	15h	No additive
4	Tube 1	50h	No additive
5	Tube 1	50h	PAA(1800) 20ppm
6	Tube 3	50h	PMA(9500) 30ppm
7	Tube 3	50h	No additive

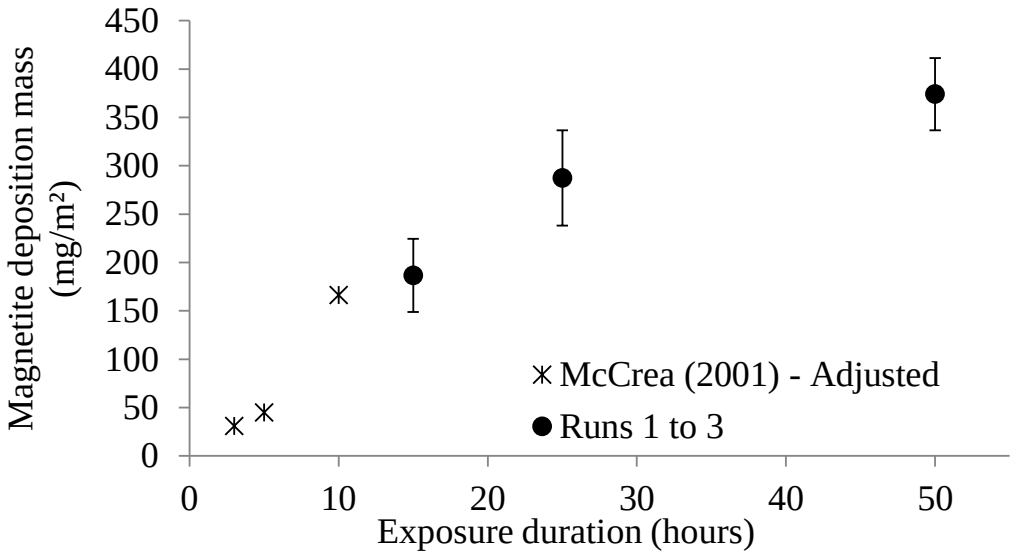

Figure 33 Magnetite deposit mass per unit surface area after Runs 1, 2 and 3 along with data from a previous study

Just after polymer addition and then frequently during the run, the coolant pH is measured and adjusted if necessary. Magnetite concentration in the coolant decreases continuously and needs to be adjusted once or twice a day. When magnetite is added, equivalent amounts of PAA and PMA are added to maintain the carboxylic group density per mass of magnetite.

After each run and the first laser scan, portions of the magnetite deposited on the tube are collected at four different locations and magnetite quantity is measured using the spectrophotometer and the same procedure as for the coolant magnetite concentration measurements. The average mass per square metre is presented in Figure 34. The mass of deposited magnetite in Runs 5 and 6 is reduced below the amounts deposited in runs without additive by about 80% in the presence of PAA(1800) and 55% in the presence of PMA(9500). These results are in agreement with visual observations made on the Alloy-800 tubes at the end of Runs 4, 5, 6 and 7.

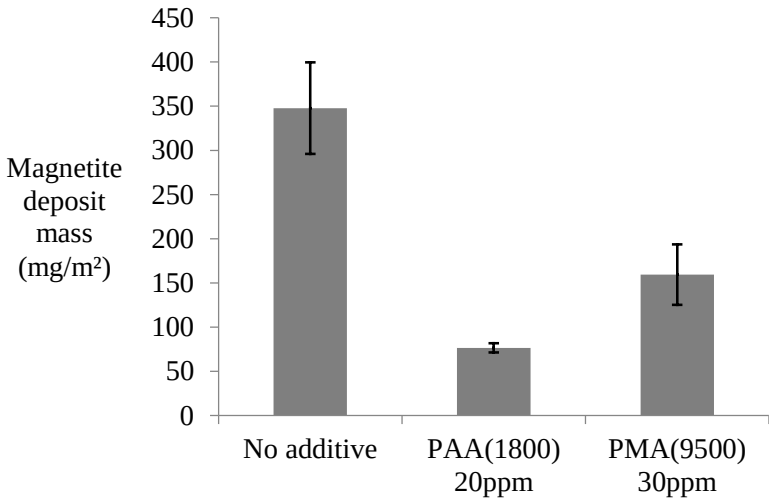

Figure 34 Magnetite deposit mass from Runs 4 to 7; results for Runs 4 and 7 are averaged into 'No additive'

Figure 35 shows the magnetite deposit site density on the Alloy-800. Pictures a) and b) are of the same position on Tube #3. Similarly, pictures c) and d) are of the same position on Tube #1. Presenting the same tube positions on these pictures is important as the heat flux distribution is not perfectly homogeneous along the tubes. The tube exposed in the presence of PAA(1800), which carries the lowest deposit mass, has the lowest site density and lowest deposition site diameter. The tube used in the presence of PMA(9500) shows intermediate values of deposition mass and site density, between those of the PAA run and those of the runs without additive. Mature deposition sites seem to have the same diameter as those observed without additive. In addition to the deposition sites observed on Figure 35, a very thin but apparently uniform layer of magnetite deposits on the tube between nucleation sites. This layer, which is not visible on the pictures, seems to have a thickness that increases with the deposition site density.

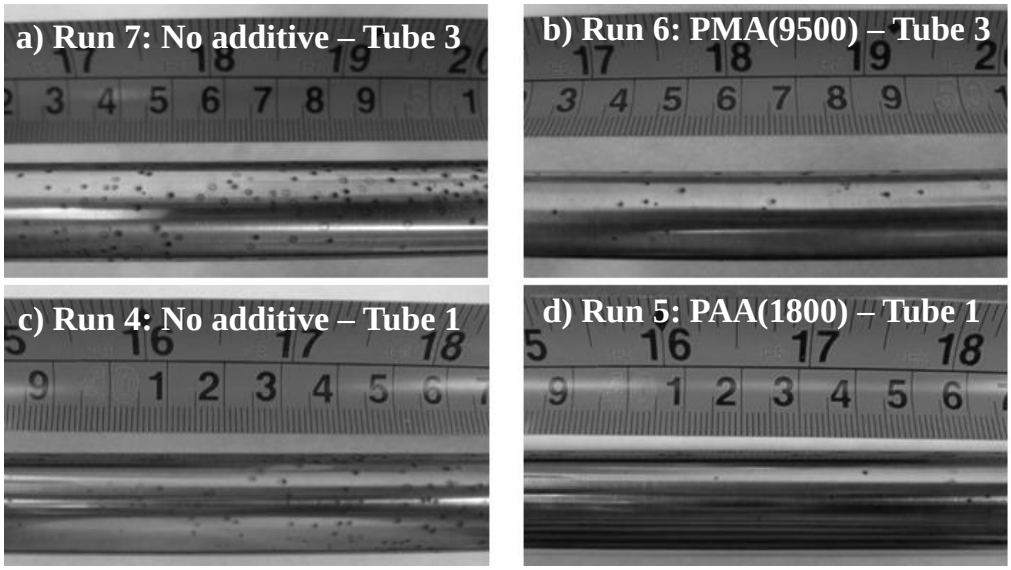

Figure 35 Alloy-800 tubes with magnetite deposition

Tubes are scanned before and after cleaning off the magnetite deposit, at the end of each run. Figure 36 shows the result of the helical laser scan performed after cleaning the tube used during Run 1. Two observations can be made from this scan. First, the tube diameter is not perfectly uniform along the tube axis. Second, any given point along the tube is characterized by a range of diameters that can be as large as 50 µm. This latter remark can be explained by the fact that the tube is not perfectly circular and as it rotates during the scan, it exposes the laser sensor with its changing projected shadow height. The implication of the former remark is that tubes have to be scanned at the exact same places (i.e. the same points along the tube) before and after magnetite removal for comparison to be valid. Due to technical limitations, the scans are performed on portions of the tube only, not on all its length. Scans performed on the fouled and clean tube of Run 1 are presented on Figure 37.

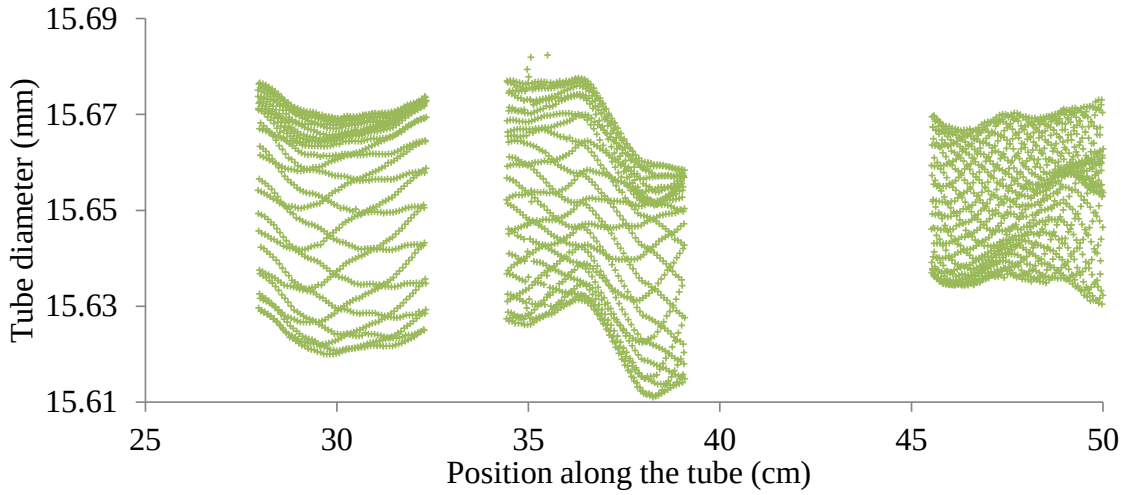

Figure 36 Laser scan performed on the clean tube following Run 1

To avoid data point overlapping and improve readability, diameter measurements are averaged. The result is shown on Figure 38 where every point of the graph corresponds to the average of 40 points of Figure 37. Thus, the relatively small diameter increase due to the presence of magnetite (5 to 7 µm for Run 1) can be measured accurately despite the high tube diameter variations (30 to 50 µm) measured during the tube rotation.

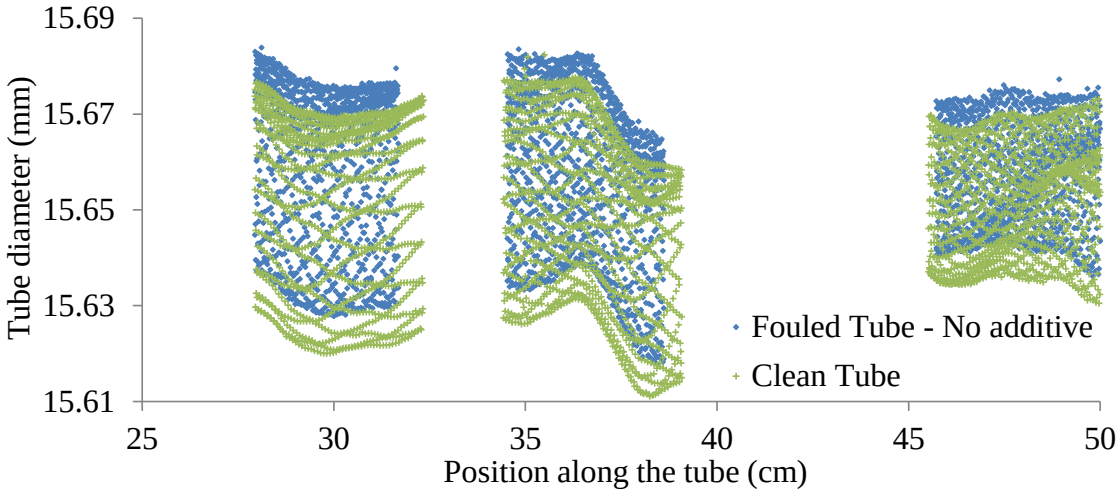

Figure 37 Laser scans from Run 1 before and after magnetite removal

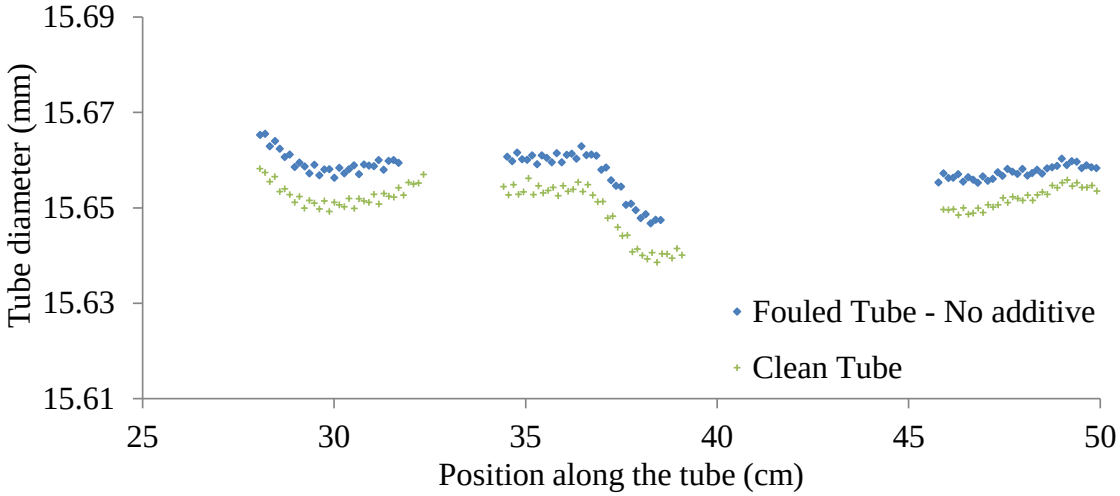

Figure 38 Laser scans from Run 1 after data averaging

Scan results for runs using PAA are shown on Figure 39. Scans of the clean bare tube measured after Runs 1, 4 and 5 are combined under the label 'Clean tube'. Scans of fouled tubes from Runs 1 and 4 are fused as well and labelled 'Fouled tube - No additive'. The scan of the fouled tube from Run 5 is labelled 'Fouled tube - PAA(1800) 20 ppm'.

The difference between the diameter scan obtained before tube cleaning (i.e. on fouled tubes) and the scan obtained after tube cleaning provides the contribution of the deposit to the measured diameter. The apparent deposit thickness on the tube is thus half of this contribution. From Figure 39 the fouling experiments without additive give an apparent average magnetite thickness of 2.5 to 3.5 µm. The run with 20 ppm of PAA(1800) shows an apparent thickness of 0.5 to 0.75 µm. Globally, the reduction of the magnetite layer by PAA ranges from 50% to 80%, which is in agreement with the magnetite deposit mass reduction shown in Figure 34. Likewise, Figure 40 shows the four scans performed after Runs 6 and 7, the two scans done on the clean tube being lumped together. The scan of the run with 30 ppm of PMA(9500) shows an apparent average magnetite thickness of 6 to 6.5 µm. The run without additive results in an apparent average thickness of 3.5 to 5 µm. The fact that the magnetite seems thicker in the presence of PMA contradicts the magnetite deposit mass results (Figure 34) that show a decrease of about 55% of the mass of magnetite collected on the tube when PMA is used.

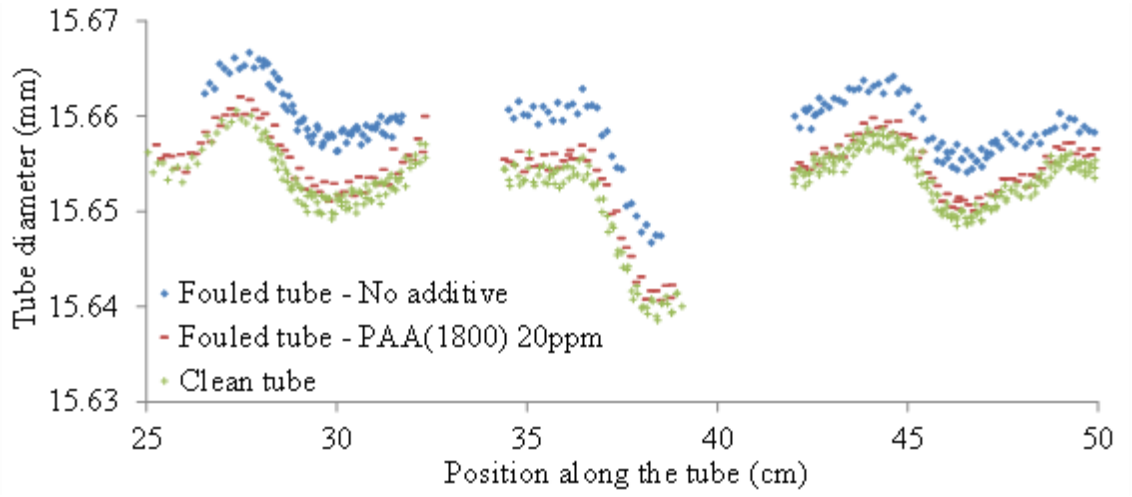

Figure 39 Comparative laser scans performed after Run 5 – 'PAA(1800)' and the 'No additive' runs (Runs 1 and 4); 'Clean tube' regroups data points from Runs 1, 4 and 5

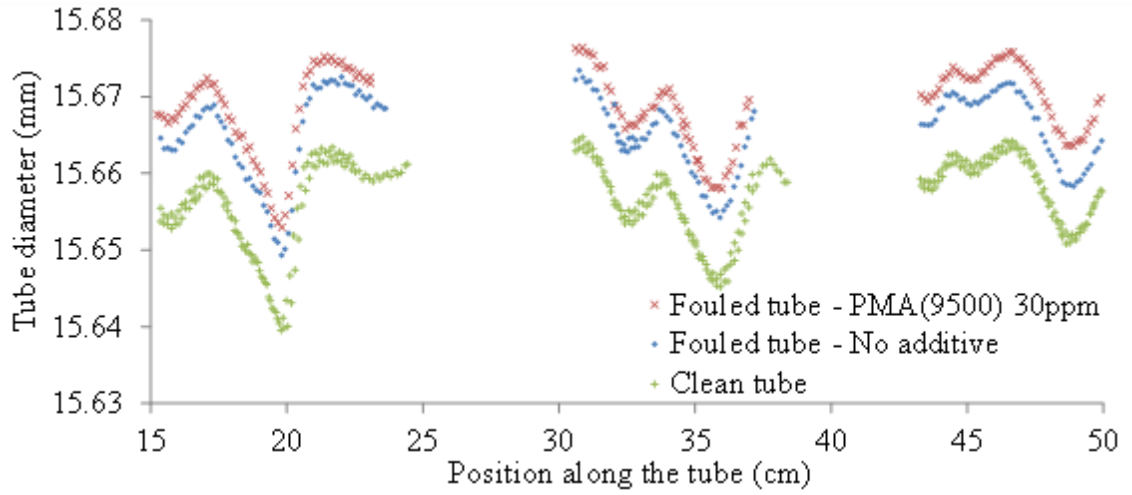

Figure 40 Comparative laser scans performed after Run 6 – 'PMA(9500)" and Run 7 – 'No additive'; 'Clean tube' regroups data points from Runs 6 and 7

4.6 Laser Scan Model

Magnetite removal from the tubes, during the recirculating loop experiments, is performed separately on regions with ring-shaped deposition sites and regions only covered by a thin layer of magnetite. The mass collected per surface area from the latter regions is only 10% to 40% lower than from regions covered with ring-shaped deposits. Therefore, neglecting the presence of ring-shaped deposits in the model should give results that remain reasonably close to reality. Besides, the assumption made during the model construction, stating that magnetite deposits on the tube under the form of regularly spaced spherical clusters, can be confirmed to some extent with the picture of Figure 41, which was taken from an Alloy-800 surface exposed to sub-cooled boiling in a magnetite suspension.

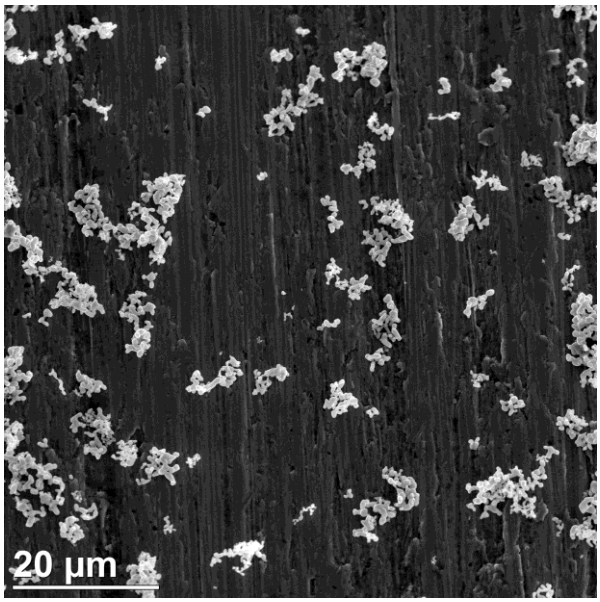

Figure 41 SEM picture of a typical magnetite deposit between nucleation sites; this magnetite "layer" appears uniform from a macroscopic point of view

Three parameters are changed independently to reconcile the apparent tube diameter difference and the corresponding magnetite deposit mass per unit surface. They are the cluster radius, the angle θ^* separating clusters and the cluster porosity. Assuming that each cluster is formed by numerous smaller spherical magnetite particles of same radius and perfectly arranged, the minimum porosity is 26%. This result comes from the maximum value of the packing factor in a face-centred cubic unit cell. However, below a porosity of 55%, the experimental values from Run 6 with PMA cannot be reached by the model algorithm used with the idealised deposition pattern described earlier. Indeed, a high diameter increase due to magnetite and low deposit mass per unit surface area are incompatible at higher packing factors (i.e. lower porosity). A porosity of 55% is then used for the simulations. A survey of literature values of magnetite deposit density performed by Turner [13] reveals that, under boiling heat transfer, two different studies reported porosity values of 50% and 70%, and a final study found values ranging from 70% to 90%. Although these values seems higher in average than the value chosen in the present study, it should be noted that the porosity values reported characterize entire magnetite layers and not individual clusters. The porosity is expected to be lower in the latter case as magnetite layers may be considered as an agglomeration of magnetite clusters, and this agglomeration of clusters has a specific porosity that adds up to the cluster porosity.

For each run, the two remaining parameters, cluster radius and angular spacing, are varied and their values recorded when both the magnetite deposit mass and tube

diameter increase correspond to the experimental values. Table 8 summarizes the parameter values that fit with the target values of the deposit thickness and mass.

Table 8 Magnetite deposit model results for each run performed in the fouling loop

	Target values from fouling experiments		Idealised pattern parameters from model simulations	
Run #	Deposit thickness (µm)	Deposited mass (mg/m²)	Cluster radius r_0 (µm)	θ^* (mrad)
Run 4 (No additive)	3	340	1.677	2.6
Run 5 (PAA 20 ppm)	0.5	75	0.280	0.3
Run 6 (PMA 30 ppm)	6	160	4.533	40.2
Run 7 (No additive)	5	340	2.820	7.3

An example of cluster pattern selection is provided in Appendix C.

According to this model, experimental results can thus be reached in the case of PAA(1800), used during Run 5, providing that the magnetite clusters are about the size of a magnetite particle and that the cluster density is very high on the tube surface (very small spacing angle). The latter configuration gives a very low tube diameter difference and magnetite deposit mass. In the case of PMA(9500), the large diameter difference measured during the scan requires very large clusters in the model; however, the magnetite deposit mass being moderate, these large clusters have to be spaced widely. The runs conducted without additive, Runs 4 and 7, show intermediate values of cluster size as well as cluster spacing angle.

For a magnetite cluster arrangement similar to the one shown in Figure 42, where the cluster planes' phase is gradually shifted along the tube, the cluster closest neighbour distance l_{min} is either the length l_1 or the length l_2. The length l_1 represents the distance between the reference cluster plane and the closest cluster plane that is in phase with this latter. The length l_2 represents the smallest distance that can be observed between clusters belonging to adjacent planes. The curvature of the tube being negligible compared to the clusters' curvature, formulas presented below assume a flat tube surface. The cluster radius r_0 and spacing angle θ^* being fixed, the only unknown parameter is the number of cluster planes N separating the reference plane and the closest plane in phase with this latter. The length l_1 increases with the value of N while the length l_2 is a decreasing function of N. Besides, the case $N = 1$ results in a value of $l_1 = 2r_0$ smaller than the value of $l_2(N = 1)$ which means that the two functions $l_1(N)$ and $l_2(N)$ have a unique intersecting point. Therefore, finding the plane configuration that maximizes the closest neighbour distance l_{min} is tantamount to finding the value of N that verifies Equation 7, which can be rewritten $l_1(N) = l_2(N)$.

$$\sqrt{\left(\frac{2R.sin(\theta^*)}{N}\right)^2 + (2r_0)^2} = 2N.r_0 \qquad \text{Equation 7}$$

$$Closest\ neighbour = l_{min} = 2N_0.r_0 \qquad \text{Equation 8}$$

The number of planes N being an integer, the solution of Equation 7 is rounded to the closest integer N_0. The closest neighbour length is then calculated using the rounded

solution N_0 as shown in Equation 8. The value of N is always kept low enough so that l_1 never exceeds the distance between two clusters of the same plane, $d = 2R.sin(\theta^*)$, (Figure 42). This latter distance is thus always higher that the closest neighbour distance. The closest neighbour values are given in Table 9 as an indication only as there are certainly other more complex plane configurations that give a higher closest neighbour value. Besides, Table 9 provides the model results for a cluster porosity of 40%. The values of r_0 and θ^* obtained for a porosity of 55%, and listed in Table 8, are repeated to ease the comparison. The number of clusters forming one cluster plane $n_0 = \frac{2\pi}{\theta^*}$ is also reported in Table 9.

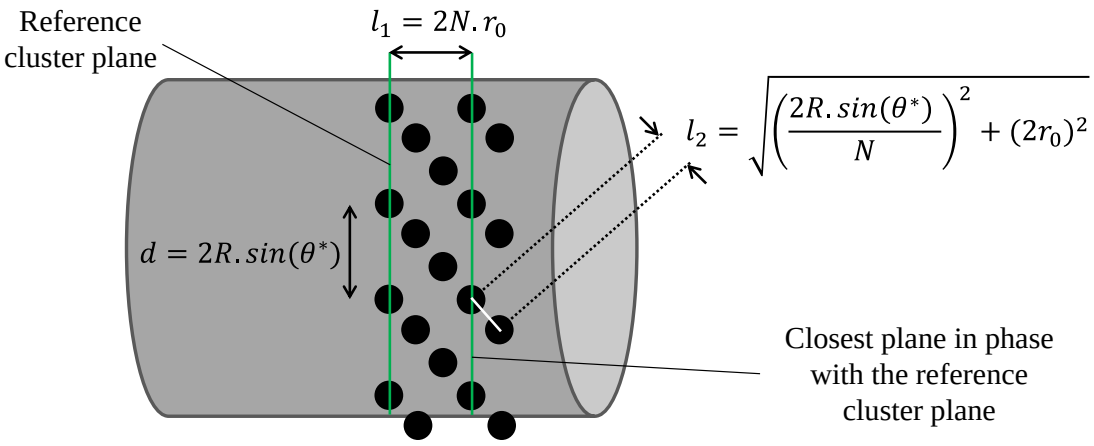

Figure 42 Diagram of the idealised cluster pattern with the two possible closest neighbor values l_1 and l_2; in this example, N = 3

Table 9 Idealised magnetite cluster pattern characteristics (cluster radius r_0, cluster spacing angle θ^*, closest neighbour length l_{min} and cluster number per plane n_0) given at two different values of cluster porosity

Run #	r_0 (µm)	θ^* (mrad)	l_{min} (µm)	n_0	r_0 (µm)	θ^* (mrad)	l_{min} (µm)	n_0
	Porosity 40%				Porosity 55%			
Run 4 Blank	1.689	3.5	13.5	1781	1.677	2.6	13.4	2434
Run 5 PAA	0.282	0.4	1.69	14153	0.280	0.3	1.68	19070
Run 6 PMA	N.A.	N.A.	N.A.	N.A.	4.533	40.2	72.5	156
Run 7 Blank	2.875	10.1	28.7	619	2.820	7.3	28.2	853

Simulation results show that the porosity has an impact on the distribution of clusters, i.e. their spacing angle, but it has little effect on cluster radius. It seems that a lower porosity requires a wider spacing of clusters to compensate for the mass gain, and so as to maintain the required tube diameter increase, the cluster radius has to increase very slightly. For all simulations, except maybe for the PMA run, the small cluster radius values and the high number of cluster per plane support the observation made during the fouling experiments that a very thin and almost invisible layer of magnetite covers the tube outside the nucleation sites. The patterns obtained for Run 6 and Run 7, characterized by a low number of clusters per plane and a high cluster radius compared to the two previous runs, are the results of the high diameter increase measured during the laser scan.

4.7 Fingertips Model Evaluation

Laser scans of the rubber fingertips are performed as if the tube were covered with magnetite. The same rotation and translation speeds as for fouling experiments are used at first. Each fingertip is then scanned a second time at a different rotation and/or translation speed. The scan results are presented in Figure 43 and Figure 44 corresponding respectively to the red and orange fingertip scan. The rolling average of the diameter measurement is calculated over one period of the periodic diameter profile. The bare fingertips diameter is obtained by measuring the minimum diameter value that appears between bumps. The values found are 17.34 mm for the red fingertip and 17.60 mm for the orange one, which is very close to the values measured using the Vernier scale. Although they show good repeatability, scans performed at different speed result in a slight difference in profile periodicity. This is probably due to the lathe translation/rotation speed programming that does not allow a better accuracy. Prior to using the fingertip model, the bump pattern characteristics have to be known. All the relevant fingertip dimensions are listed in Table 5, except the bump height that needs to be measured.

4.7.1 Bump Height Measurement

The orange fingertip is entirely covered with bumps, and their distribution is symmetrical to the horizontal plane containing the tube axis, as shown on Figure 45. Thus, shadows projected by the bumps on each side of the symmetry plane are identical, regardless of the angle at which the fingertip is scanned.

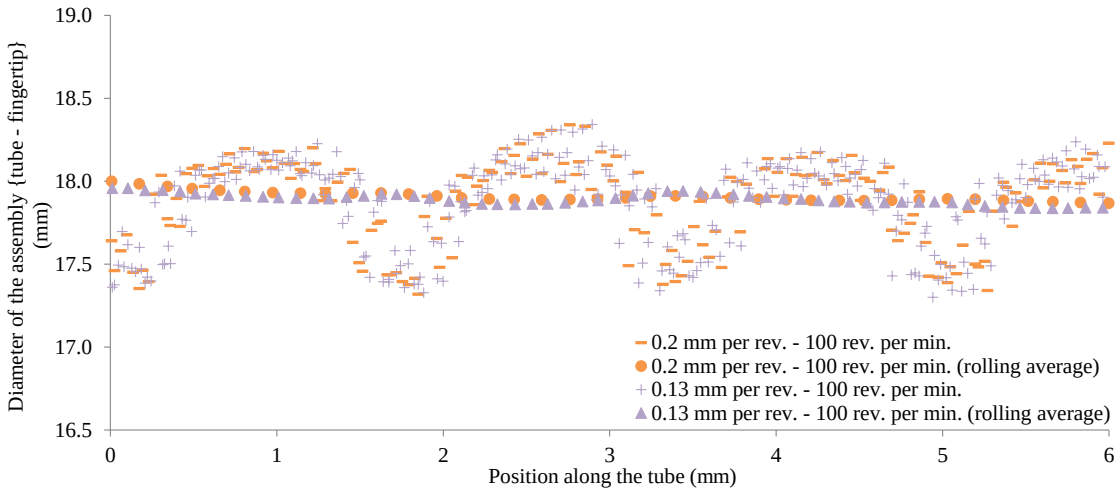

Figure 43 Result of the helical laser scan performed on the red fingertip at two different translation speeds; this fingertip is covered by bumps on only half of its surface

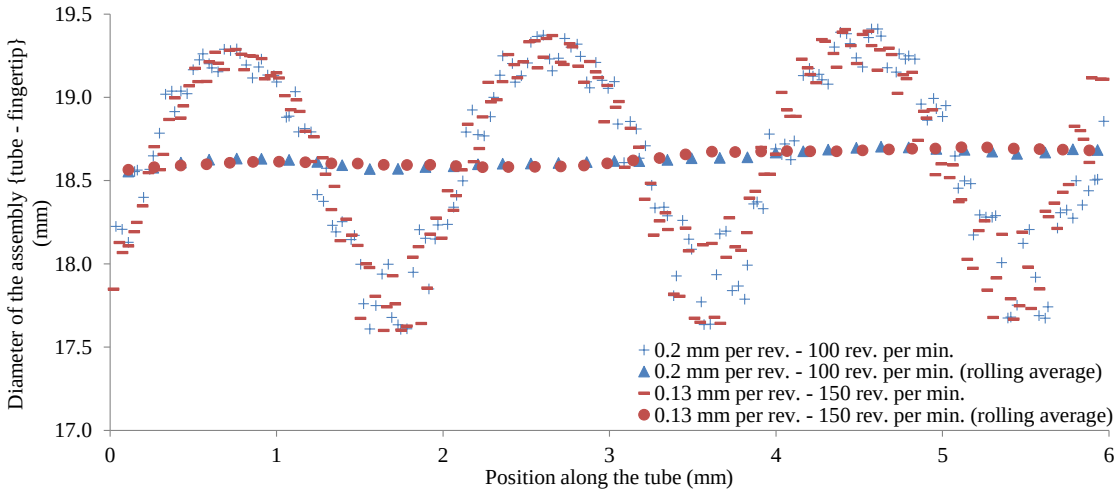

Figure 44 Result of the helical laser scan performed on the orange fingertip at two different translation and rotation speeds; this fingertip is completely covered with bumps

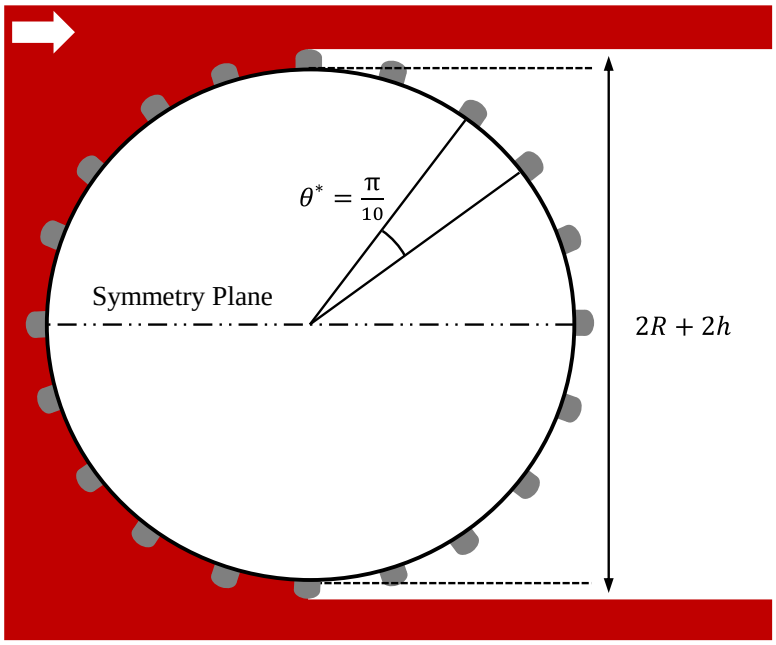

Figure 45 Schematic cross section diagram of the orange fingertip inserted on the tube during the laser scan, *R* is the fingertip radius, *h* is the bump shadow height

As a consequence the results presented on Figure 44 is the sum of two identical contributions coming from bumps scanned on each side of the symmetry plane. By subtracting the diameter of the bare fingertip inserted on the tube and dividing the results by two, the shadow height evolution due to the bumps scanned on one side of the symmetry plane only are obtained and shown on Figure 46. The graph is similar to Figure 44 as only the amplitude of the sinusoidal pattern has been divided by two and the data points have gone through an offset so that the sinusoid minima correspond to a null height. The bump height can thus be approximated by measuring the amplitude of the sinusoid h_{ora} which appears to be about 0.87 mm. In fact, the sinusoid amplitude is a bit smaller than the real bump height.

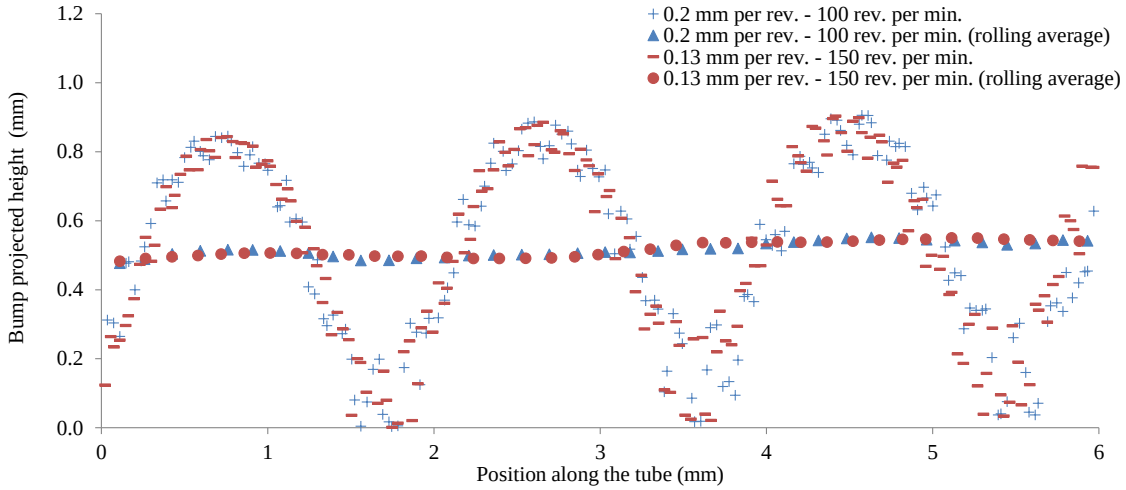

Figure 46 Adjusted orange fingertip scan results

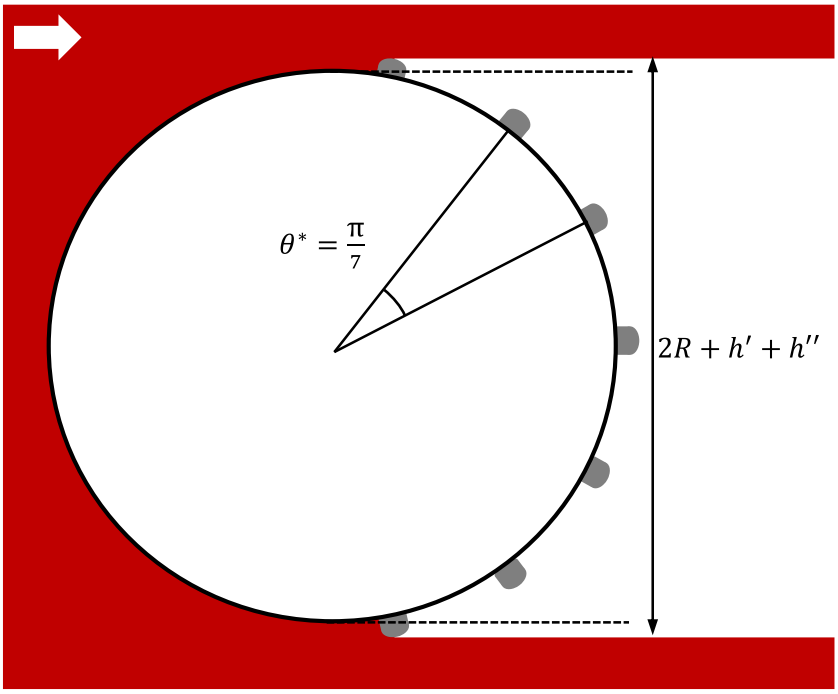

Figure 47 Schematic cross section diagram of the red fingertip bumps and tube during the laser scan

The sinusoid amplitude needs to be adjusted as the points forming the maxima of the sinusoid curve of Figure 46 result from the averaging of 40 diameter measurements, which are not all taken when the bump shadow is at its maximum. The bump height adjustment calculations are presented in Appendix D. The new adjusted bump height used in the rest of the study is $h_0^{ora} = 0.91$ mm for the orange fingertip.

Data averaging in Figure 46 gives an average shadow height of about 0.51 mm. The fact that gaps between rubber bumps observed from the scan result are not better marked might be due to the bumps alignment. If this latter is imperfect, bumps in the background and/or foreground might obstruct partially the gap made by the bump being scanned. Also the width of the laser (about 0.2 mm) certainly has an impact on contour clearness. As the centre of the laser measures the bare fingertip surface, the extremities of the laser might already be measuring the next bump shadow or it might still be measuring the previous one. This reduces the angular range for which the laser measures a null bump height.

Interpreting the red fingertip scan results is not as straightforward as it is covered by bumps only on half of its surface. This appears to make things easier at first sight as the contribution to the shadow height is due to one bump only. However, there are certain angular positions for which two bumps are shadowing the laser sensor at the same time as shown on Figure 47. For these angular positions, the laser records shadow heights data that are inconsistent with the other "normal" angular positions where one bump is shadowing the sensor at a time. Measuring only one bump at a time is important as it gives an accurate measurement of bump height and it makes comparison with the model and

the other scans possible. The model, the magnetite deposit and orange fingertip scans are based on the assumption that the tube has a symmetry plane such as the one drawn on Figure 45, thus the additional shadow height formed by deposit or bumps may be divided by two to represent the contribution of only one side of the symmetry plane. In the case of the red fingertip, the parasitic measurements bias the diameter variations read on Figure 43. The impact of the red fingertip asymmetry on the average height recorded by the laser sensor is assessed by following the evolution of the bump height over one complete rotation of the tube. The "abnormal" angular intervals are detected and the shadow height variation measured during these intervals is calculated.

So as to find the angular interval where two bumps are shadowing the sensor at the same time, the angle θ_{lim}, for which one bump lies at the limit of the tube shadow (Figure 48), is calculated using the Equation 9, where R is the radius of the bare fingertip when inserted on the tube and h_0 is the bump height.

$$\theta_{lim} = \operatorname{acos}\left(\frac{R-\frac{h_0}{2}}{R+\frac{h_0}{2}}\right) \qquad \text{Equation 9}$$

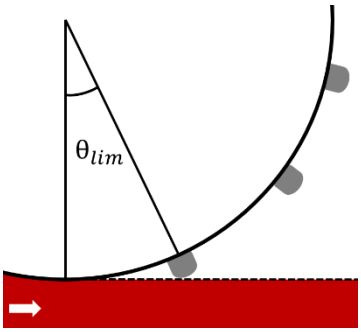

Figure 48 Close up representation of a bump at the limit of the tube shadow; the angular position of this bump in relation to the vertical is noted θ_{lim}

The amplitude of the periodic profile shown on Figure 43, $h_{red} = 0.91$ mm (which should not be confused with the orange adjusted bump height $h_0^{ora} = 0.91$ mm), is used as a first approximation of the bump height. Equation 9 gives the value of 0.450 rad for θ_{lim}, which is very close to the value of $\theta^* = \frac{\pi}{7}$ which equals to 0.449 rad. As a consequence, by assuming that $\theta_{lim} \sim \theta^*$, the diagram shown on Figure 47 can be drawn again on Figure 49 with the Bump noted #1 at the top of the tube, i.e. producing a shadow whose height is equal to the bump height, and the Bump #7 lying at the limit of the tube shadow. Assuming a clockwise rotation of the tube on Figure 49, the angular interval producing inconsistent measurements then starts when the Bump #7 reaches θ_{lim}, i.e. starts shadowing the sensor.

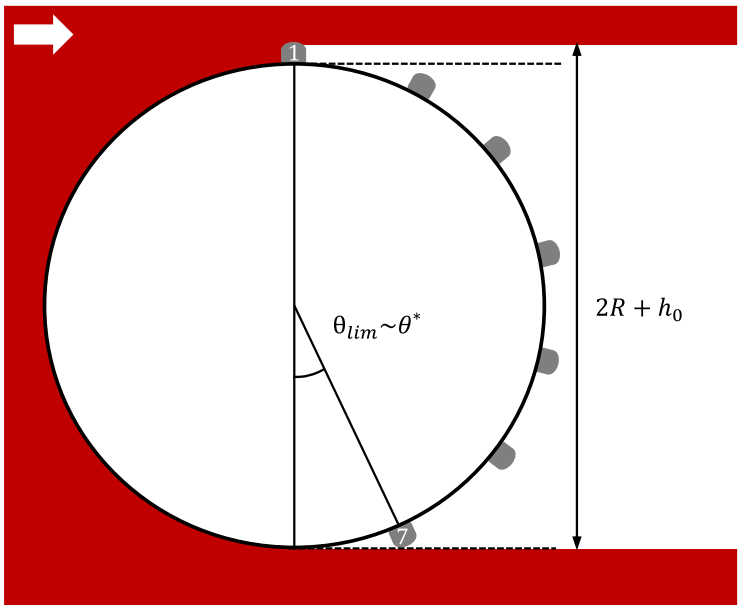

Figure 49 Particular position of the red fingertip where Bump #1 is exposing all its height to the sensor while Bump #7 is about to enter the laser field of vision (assuming a clockwise rotation)

And the interval stops when the Bump #1 is at the position θ_{lim} where it leaves the "field of vision" of the sensor, being completely shadowed by the tube. If θ is set equal to zero when the Bump #1 is at the top of the tube, the angular interval is then written [$\theta^* - \theta_{lim}$, θ_{lim}], that is [0 , θ_{lim}] with the approximation made earlier.

The shadow height variations during this angular interval are computed using the same function $height(\theta)$, see Figure 18, used for the magnetite deposit scans. To simplify the height calculations, bumps are assumed to be spherical of diameter h_{red}. Results are presented in Figure 50. As expected the laser sensor measured the Bump #1 maximum height h_{red} for $\theta = 0$, i.e. when the Bump #1 is at the top of the tube, while the Bump #7 is completely shadowed by the bottom part of the tube (this configuration is depicted in Figure 49).

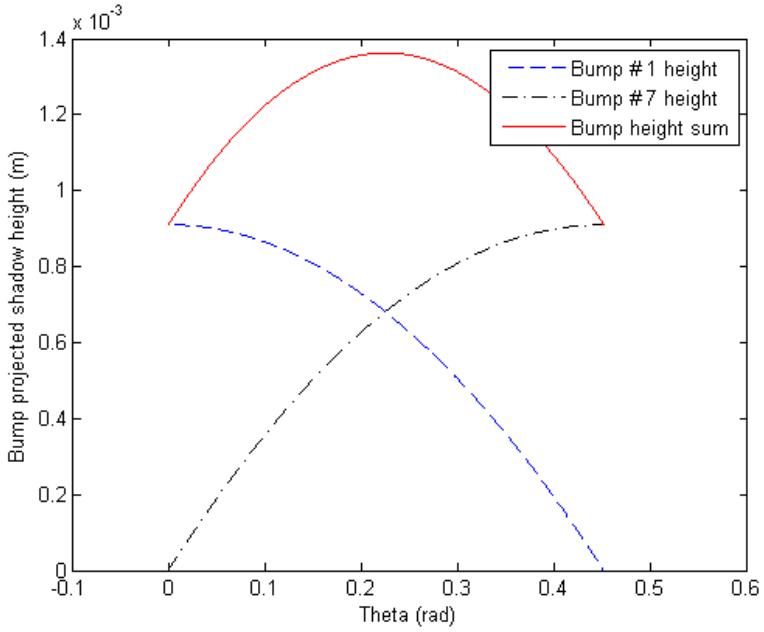

Figure 50 Projected shadow height for the two bumps shadowing the sensor at the same time

As the tube rotates, the Bump #1 is progressively shadowed by the top part of the tube, and the Bump #7 shadow height increases until this latter reaches a maximum at the position $\theta = \theta_{lim}$ where the Bump #1 is laying completely in the shadow of the top part of the tube. It should be noted that the resulting height sum is always higher than the maximum bump height h_{red}, all over the angular range presented.

The approximated bump height h_{red} needs to be refined. The same method as for the orange fingertip is used and detailed in Appendix D. By taking into account the 40 measurements averaging of Figure 43 and the asymmetrical behaviour of bumps described above, the adjusted bump height h_0^{red} is found to be 0.85 mm.

4.7.2 Model Results

Knowing the bump height of both fingertips, the thickness values read by the laser can thus be found by computing bumps projected area. The same algorithm as for the magnetite deposit model is used, except from shadow shapes. The magnetite deposit model assumes that the top halves of magnetite clusters produce circular shadow corresponding to the cluster radius, and cluster bottom halves produce rectangular shaped shadows in continuation to the top circular shape. For the fingertip model, an ellipsoidal shape is used to model the top shadow half, the bottom shadow part being modelled by a rectangle (Figure 51). The ellipse minor axis corresponds to the bump height and the major axis to half the bump width d_0 measured earlier.

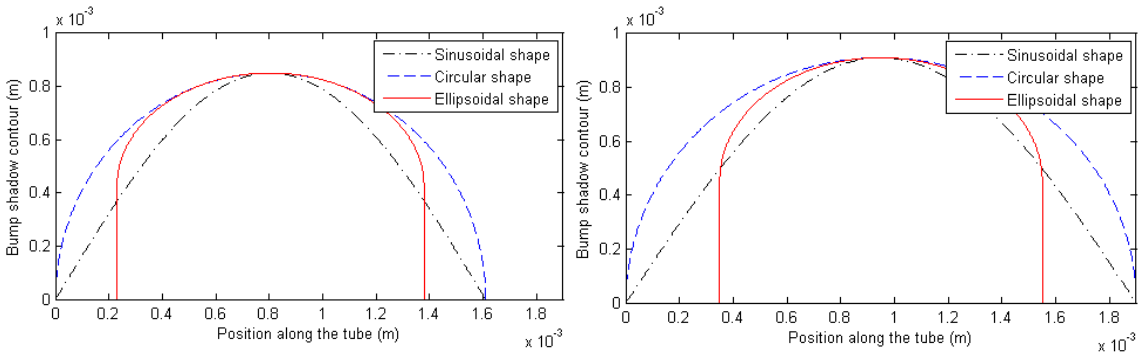

Figure 51 Different projected shadow shapes used for the red (respectively orange) fingertip model presented on the left (respectively right)

Two other shadow shapes are used to take into account the imperfect bump alignment: a sinusoidal and a circular shape contour, adjusted to equal zero at the limits of the bump plane and to be worth the bump height at its middle.

In the case of the orange fingertip, an average height increase due to the presence of the bump can be computed directly using the magnetite cluster algorithm and the specific shadow shapes described earlier.

For the red fingertip, the magnetite cluster algorithm has to be applied separately over a standard angular interval where only one bump is shadowing the sensor and over the special interval, presented in Figure 50, where the contribution of two bumps is collected by the sensor at the same time. This results in a "normal" average height increase due to the red bumps that can be observed over an angular range of $\frac{12.\pi}{7}$ for every fingertip rotation, and a "special" average height increase that can be recorded over two $\frac{\pi}{7}$ - wide angular intervals for every fingertip rotation. By weighting the average heights by their

corresponding angular presence around the fingertip, the global average height increase due to the presence of bumps on the red fingertip is found to be 0.494 mm. As a comparison, the value obtained without any adjustment applied to the red fingertip model, i.e. assuming that only one bump shadows the sensor at all time, is 0.487 mm.

The shadow shape that fits the laser scan result the best is the semi-circular shape in the case of the red fingertip with an average height percent error of 9.9% and the semi-ellipsoidal shape for the orange fingertip with a percent error of 4.7%. It should be noted that unlike the orange fingertip that has uniform bumps, some bumps of the red fingertip are slightly distorted and the bump height uniformity is not as good. This probably explains the lack of clearness of the red fingertip scan shown on Figure 43 as well as the higher percent error obtained.

Table 10 Fingertip model results using the three shadow shapes for both fingertips

		Red fingertip	Orange fingertip
θ^* (rad)		$\frac{\pi}{7}$	$\frac{\pi}{10}$
d_0 (mm)		1.15	1.20
Adjusted bump height (mm)		0.85	0.91
R (mm)		8.67	8.80
Gap between bumps belonging to adjacent planes (mm)		0.46	0.70
Average height increase from model simulations (mm)	Semi-ellipsoidal shape	0.494	0.489
	Sinusoidal shape	0.490	0.542
	Semi-circular shape	0.621	0.677
Average height increase from laser scans (mm)		0.565	0.513

5.0 DISCUSSION

5.1 Surface Analyses

The IEP of magnetite is found to be higher than the commonly accepted range, pH 6 to 7. The use of a weak base (ammonia) to adjust the pH, which lead to the adsorption of protonated amines on surfaces, is believed to be the reason for this IEP variation. Concerning Alloy-800, the IEP value found is in agreement with previous measurements by Khumsa-Ang [45]. Moreover, it is very close to the IEP value of stainless steel SS304 reported to be around 4 [64]. The behaviour of both magnetite and Alloy-800 particles in the presence of polymeric additives is in good agreement with observations made previously with PMA [30] and other carboxylic acids such as citric acid [31]. In the presence of these two additives, the IEP of a magnetite suspension shifts to more acidic values due to the presence of carboxylate anions at the magnetite surface. The carboxylic additive can also counteract particle agglomeration at favourable values of pH, i.e., when the pH is close to the IEP. This leads to the stabilization of a narrow particle size distribution over a wide pH range. Particle size distribution was not measured in the present study but, like citric acid and PMA, PAA provides anionic groups that are expected to enhance electrostatic stabilization. The coating of surfaces by polymers gives a measurable effect at a carboxylic group concentration per mass of particle as low as 0.22 mmol/mg. Polymer adsorption on both the Alloy-800 and the magnetite could thus be

responsible for an increased electrostatic repulsive force between the heating surface and magnetite particles. Moreover, such a force seems to be effective over a wider pH range in the presence of polymers than in their absence. Thus, these polymers could help to mitigate agglomeration and/or adhesion where the local pH differs from that in the bulk water, such as in crevices or under deposits. Similarly, FFA could also provide an electrostatic repulsive force over a large range of pH, since both the Alloy-800 surface and the magnetite particles are positively charged in its presence. The FFA molecule contains one primary and one secondary amine group, so its protonation should lead to positively-charged species. If it is assumed that one of the amine groups is used as the anchor point of the molecule to the Alloy-800 or magnetite surface, one positive charge at most can be formed on each FFA molecule. If FFA is used in a high-pH coolant circuit, the main concern is that, contrary to polymers that provide extra negative charges on surfaces that are already negatively charged at high pH, FFA will shift completely the surface charges to positives values. This could lead to unexpected effects that need to be investigated. A diamine FFA seems to be the best compromise of a coating additive relying on both steric repulsion [60] and electrostatic repulsion as a monoamine FFA is expected to carry no charge once anchored to a surface.

Contact angle measurements proved the hydrophobic properties of FFA-coated metals. Polymeric additives seem to make the surface slightly hydrophilic, although this observation could also be the result of discrepancies in the metal oxide layer characteristics.

5.2 Bench-top Experiment

Video footage of boiling on the Nichrome ribbons suggests that PAA(8000) or PMA(9500) reduce the number of bubble nucleation sites; the SEM pictures of exposed ribbons indicate that the number of major deposition sites of magnetite is correspondingly reduced, although the deposits are larger and thicker and surrounding surfaces are cleaner. When the concentration of PAA(8000) is increased, the effect of polymer is amplified – the deposition sites are less numerous but each apparently carries more magnetite. In terms of overall reduction of deposition, PAA(1800) is the most efficient, decreasing significantly both the deposition site density and the deposition rate at each site. This is consistent with the study conducted by Balakrishnan et al. [47], which compared the effectiveness of PAA of two molecular weights and showed that, under flow boiling conditions, a lower molecular weight polymer (MW 3500 to 5000) is more efficient at stabilizing magnetite concentration in the bulk water. Therefore, it can be concluded that the molecular weight of the dispersant has a major influence on magnetite deposition.

There is a loose correlation between the deposition site size and the surface wettability, since the increase of the latter could lead to the formation of bigger vapour bubbles and thus bigger deposition sites. Yet, the results obtained from the fouling loop experiment did not show any noticeable increase of the deposition site size in the presence of polymeric additives.

The dense deposition sites observed on ribbons in the presence of PAA and PMA might be the result of longer polymer chains that promotes inter-particle bonding. PAA(8000), which has a theoretical maximum extended length of about 21 nm, could be

long enough to link two magnetite particles together while PAA(1800), with its 6 nm theoretical maximum extended length, would be too short.

The fact that bench-top experiments show similar results when PAA(8000) and PMA(9500) are used supports the idea that molecular weight governs polymer efficiency. It must be noted however, that the agglomerating effect of PMA(9500) at ribbon nucleation sites cannot be observed visually on the tube nucleation sites. Moreover, these observation go against the hypothesis that increased polymer length provides additional steric repulsion to surfaces. Nsib et al. [30] showed that bridging between particles does not occur significantly in the case of heavy PMA molecules (MW ~ 30000) coating hematite particle; on the contrary, particle stabilization is more effective than with lighter PMA molecules. Steric hindrance may be more pronounced in the case of PMA than for PAA, as PMA has an additional carbon group in its repeating unit which reduces the molecular degree of freedom.

5.3 Fouling Loop and Laser Scan

The recirculating loop experiments also show a clear reduction in magnetite deposition when PAA or PMA are present. These two dispersants reduce the deposition site density on the tube as well as the magnetite deposition mass. Once again, PAA(1800) proves more effective than PMA(9500) in reducing both the number of deposition sites on the tube and the magnetite deposition rate at a site. Although the tube diameter increase at the end of Run 4 (without additive) and Run 5 (with PAA(1800)) shows a good correlation with the magnetite deposit mass, it is not yet understood why the laser scan for Run 6 (PMA(9500))

shows a high diameter difference for a moderate magnetite deposit mass. It was observed, at the end of the run, that the tube colour was slightly different from that in other runs. It had a faint orange-red tone, possibly due to the formation of haematite. An oxygen ingress during the run is not excluded; however, the formation of haematite in the presence of PMA has also been observed by Burgmayer et al. [48]. During a fouling test at high temperature and high pH, Burgmayer noticed that, in the presence of PMA, about half of the deposit collected on the heating surface was haematite, the other half being magnetite. On the other hand, in the absence of polymeric additive, almost all of the deposit was magnetite. Besides, the corrosion of carbon steel during the contact angle sample preparation is only observed when PMA is used. Therefore, it seems that the presence of PMA increases the oxidation capacity of alkaline water. Yet, the formation of haematite during the PMA run does not explain the puzzling laser scan results. The difference in magnetite thickness measured by the laser between Runs 4 and 7, which correspond to the same operating conditions, is also questionable and seems to be due to a helical scan setup issue.

Some limitations and uncertainties make the accuracy of the laser scan questionable to some extent:

- The transverse position of the tube in relation to the laser profilometer has an impact on the diameter measurements. In fact, the laser is designed to be focused at mid-distance between the laser generator and the laser sensor, and that is the place where the tube should be placed. A small deviation from the centre seems to create an offset in the diameter measurements.

- When installed on the lathe, the Alloy-800 tubes presents axial run-out issues, the impact of which on the diameter measurements is not known. However, the previous point suggests that it does have an impact on the measurements.
- The impact of laser diffraction due to the exposure of magnetite particles that are about the size of the laser wavelength (around 700 nm for a red laser) is unknown.

5.4 Laser Scan Model

The laser-scan model based on the idealised fouling pattern indicated that the loop experimental results for PMA(9500) could be explained providing that the uniform magnetite deposit between bubble nucleation sites was in the form of larger and more spaced-out clusters on the tube than were invoked to explain deposits without additive or with PAA. This contradicts the dispersant properties of PMA mentioned earlier, although it could be linked to the fact that bench-top experiments show thicker magnetite deposits at nucleation sites when this polymer is used. The fingertip scan and its comparison to the model give satisfactory results for one of the two fingertips.

Additional scans performed on more magnetite deposits and diverse other patterns would be needed to refine the algorithm. Yet, this latter remains a useful tool to give some perspective to the laser scan readings and help in the comparison of experimental magnetite thickness and mass values.

Recommendations:

- The Swagelok fitting at the end of the Alloy-800 tube, used to fix the tube on the lathe, should be perfectly aligned with the tube to avoid axial run-out problems.
- A procedure should be developed to ensure that the tube lies at the centre of the laser profilometer, or at least that the tube is always placed at the same position between the laser generator and sensor so as to make scan comparisons consistent.
- The influence of the scanning speed does not seem to have an influence on fingertip profile, but its impact would need to be investigated on micrometre scale profiles.
- The implicit assumption that the scanning of a fingertip, with millimetre-size bumps, and a magnetite deposit, with micrometre-size clusters, could be modelled the same way should be used carefully as it has not been validated. In particular, it was assumed that a complete rubber bump was illuminated by the laser at once, which is not true as the laser width is smaller than bump width. If the model were to be refined with more fingertip-like scans, a pattern with a periodicity smaller than the laser width, should be preferred
- In order to ease analyses and modelling, the heating surface should be able to generate a uniform heat flux on its surface so as to create a uniform deposit. The more uniform the deposit, the closer to reality is the model as this latter relies on symmetries and periodicities.
- Fouling experiments should be conducted on a heating surface that can be subjected to three different analyses: the helical laser scan, SEM analysis and

deposit mass measurements. The diameter increase and deposit mass could thus be compared to a precise magnetite deposit pattern provided by the SEM, and the model could be refined accordingly.

6.0 CONCLUSIONS

1. Helical scans with a laser profilometer of Alloy-800 tubes show very good repeatability and resolution at the micrometer scale for measuring diameter increases due to fouling. The interpretation of the scan results in terms of deposit mass and dispersion is complex, however, and requires further development, especially when local deposition is increased by bubble nucleation.
2. Screening experiments conducted in a beaker with heated Nichrome ribbons are useful for indicating qualitatively the influence of chemical additives on magnetite deposition under low-pressure and low-temperature conditions.
3. A film-forming amine (FFA) significantly improves boiling heat transfer in beaker experiments but also agglomerates magnetite particles from suspension at high concentration – notably at the vapour-liquid interface; agglomerates then stick to most surfaces. Magnetite agglomeration in the presence of FFA is in agreement with the reported detergent properties of film-forming amines [58, 59].
4. The addition of polyacrylic acid PAA(1800), PAA(8000) or polymethacrylic acid PMA(9500) to water with pH adjusted with ethanolamine reduces the magnetite deposition site density on Nichrome ribbons under pool-boiling conditions.
5. Similar results are obtained with heated Alloy-800 tubes sustaining flow-boiling conditions in ammoniated water in a recirculating loop. During a 50 h exposure of an

Alloy-800 tube in the loop, the addition of PAA(1800) and PMA(9500) reduces the magnetite mass deposited on the surface by about 80% and 55% respectively.

6. The molecular weight of a polymer has a major impact on its ability to mitigate magnetite fouling. A polymer of low molecular weight has the greater effect.
7. The polymers PMA(9500) and PAA(8000) have similar effects on deposition during beaker experiments, possibly because they have carbon chains of about the same length and thus carry about the same number of functional carboxylic groups.
8. Zeta potential measurements indicate that PAA and PMA impose negative charges on magnetite and Alloy-800, reducing the pH at the isoelectric point (IEP) and probably increasing the repulsive force between particles and tube surfaces. FFA imposes a positive charge on magnetite and Alloy-800 surfaces over a wide range of pH, pushing the IEP outside the range 2 – 10.5.
9. PMA seems to be more corrosive than PAA, or standard amines used for pH control.

References

[1] M. G. Fontana, *Corrosion Engineering*, 3rd ed.: McGraw-Hill Book Company, 1987.

[2] D. H. Lister, "Corrosion products in power generating systems," in *International conference on the fouling of heat transfer equipment*, Troy - N.Y., 1979.

[3] IAEA, "Assessment and management of ageing of major nuclear power plant components important to safety: steam generators," IAEA2011.

[4] R. L. Tapping, J. Nickerson, P. Spekkens, and C. Maruska, "CANDU steam generator life management," *Nuclear Engineering and Design,* vol. 197, pp. 213-223, 2000.

[5] P. R. Tremaine and J. C. LeBlanc, "The solubility of magnetite and the hydrolysis and oxidation of Fe2+ in water to 300°C," *Journal of Solution Chemistry*, vol. 9, pp. 415-442, 1980.

[6] K. Mabuchi, Y. Horii, H. Takahashi, and M. Nagayama, "Effect of temperature and dissolved oxygen on the corrosion behavior of carbon steel in high-temperature water," *Corrosion,* vol. 47, pp. 500-508, 1991.

[7] P. Roberge, *Corrosion engineering: principles and practice*: McGraw-Hill Professional, 2008.

[8] L. L. Tomlinson, "Mechanism of corrosion of carbon and low alloy ferritic steels by high temperature water," *Corrosion,* vol. 37, pp. 591-596.

[9] C. W. Turner and P. Angell, "Implications of steam generator fouling on the degradation of material and thermal performance," in *7th CNS International Steam Generators to Controls Conference*, Toronto, 2012.

[10] Y. F. Cheng and F. R. Steward, "Corrosion of carbon steels in high-temperature water studied by electrochemical techniques," *Corrosion Science,* vol. 46, pp. 2405-2420, 2004.

[11] E. C. Potter and G. M. W. Mann, "Oxidation of mild steel in high temperature aqueous systems," in *1st International Congress on Metallic Corrosion*, London, 1961, pp. 417 - 426.

[12] C. W. Turner and S. J. Klimas, "Deposition of magnetite particles from flowing suspensions under flow-boiling and single-phase forced-convective heat transfer," *The Canadian Journal of Chemical Engineering,* vol. 78, pp. 1065-1075, 2000.

[13] C. W. Turner, S. J. Klimas, and M. G. Brideau, "Thermal resistance of steam-generator tube deposits under single-phase forced convection and flow-boiling heat transfer," *The Canadian Journal of Chemical Engineering,* vol. 78, pp. 53-60, 2000.

[14] D. H. Lister, A. D. Feicht, K. Fujiware, M. Khatibi, L. Liu, T. Ohira, *et al.*, "The mitigation of flow accelerated corrosion in the feed water systems of nuclear reactors - The influence of dissolved oxygen under different operating conditions," *Power Plant Chemistry,* vol. 13, 2011.

[15] E. G. Brush, "Corrosion and corrosion product release behavior of carbon steel in neutral feedwater," in *American Power Conference*, 1969, pp. 699-705.

[16] T. Prusek, E. Moleiro, F. Oukacine, A. Adobes, M. Jaeger, and M. Grandotto, "Deposit models for tube support plate flow blockage in Steam Generators," *Nuclear Engineering and Design,* vol. 262, pp. 418-428, 2013.

[17] C. W. Turner, W. Guzonas, and S. J. Klimas, "Surface chemistry interventions to control boiler tube fouling - Part I," Atomic Energy of Canada Limited, Chalk River, Ont., EPRI Report TR-110083/AECL-120362000.

[18] C. W. Turner, S. J. Klimas, and M. G. Brideau, "The effect of alternatives amines on the rate of boiler tube fouling," AECL1997.

[19] L. McCrea, "Deposition of Corrosion Product Particles onto Heat Exchange Surfaces," M.Sc.E., University of New Brunswick, 2001.

[20] N. Epstein, "Thinking about heat transfer fouling: a 5 x 5 matrix," *Heat transfer engineering,* vol. 4, pp. 43-56.

[21] H. E. C. Rummens, J. T. Rogers, and C. W. Turner, "The thermal hydraulics of tube support fouling in nuclear steam generators," *Nuclear technology,* vol. 148, pp. 268-286.

[22] D. Q. Kern and R. E. Seaton, "A theoretical analysis of thermal surface fouling," *British Chemical Engineering,* vol. 4, pp. 258-262, 1959.

[23] N. Epstein, "Particulate Fouling of Heat Transfer Surfaces: Mechanisms and Models," in *Fouling Science and Technology*. vol. 145, L. F. Melo, T. R. Bott, and C. A. Bernardo, Eds., ed: Springer Netherlands, 1988, pp. 143-164.

[24] C. W. Turner, D. H. Lister, and D. W. Smith, *The deposition and removal of sub-micron particles of magnetite at the surface of alloy-800*. Chalk River, Ont: Atomic Energy of Canada Limited, 1994.

[25] D. H. Lister and F. Cussac, "Modeling of particulate fouling on heat exchanger surfaces: Influence of bubbles on iron oxide deposition," *Heat Transfer Engineering,* vol. 30, pp. 840-850, 2009.

[26] J. Cossaboom and D. H. Lister, "The fouling of alloy-800 heat exchanger tubes by nickel ferrite under bulk boiling conditions," in *6th International Conference on Heat Exchanger Fouling and Cleaning - Challenges and Opportunities*, Kloster Irsee, Germany, 2005.

[27] C. W. Turner, "Rates of particle deposition from aqueous suspensions in turbulent flow: a comparison of theory with experiment," *Chemical Engineering Science,* vol. 48, pp. 2189-2195, 1993.

[28] M. J. Rosen, *Surfactants and Interfacial Phenomena*, 3rd ed. Hoboken, New Jersey: John Wiley & Sons, Inc., 2004.

[29] P. W. J. Glover and M. D. Jackson, "Borehole electrokinetics," *Leading Edge (Tulsa, OK),* vol. 29, pp. 724-728.

[30] F. Nsib, N. Ayed, and Y. Chevalier, "Comparative study of the dispersion of three oxide pigments with sodium polymethacrylate dispersants in alkaline medium," *Progress in Organic Coatings,* vol. 60, pp. 267-280, 2007.

[31] A. Hajdú, E. Tombácz, E. Illés, D. Bica, and L. Vékás, "Magnetite Nanoparticles Stabilized Under Physiological Conditions for Biomedical Application," in *Colloids for Nano- and Biotechnology*. vol. 135, Z. Hórvölgyi and É. Kiss, Eds., ed: Springer Berlin Heidelberg, 2008, pp. 29-37.

[32] P. L. García-Ybarra and J. L. Castillo, "Mass transfer dominated by thermal diffusion in laminar boundary layers," *Journal of Fluid Mechanics,* vol. 336, pp. 379-409, 1997.

[33] M. Basset, N. Arbeau, J. McInerney, and D. H. Lister, "Deposition of magnetite particles onto alloy-800 steam generator tubes," in *3rd Int. Steam Generator and Heat Exchanger Conference*, Toronto, Canada, 1998, pp. 677 - 693.

[34] M. Basset, J. McInerney, N. Arbeau, and D. H. Lister, "The fouling of alloy-800 heat exchange surfaces by magnetite particles," *The Canadian Journal of Chemical Engineering,* vol. 78, pp. 40-52, 2000.

[35] C. W. Turner and M. Godin, "Mechanisms of Magnetite Deposition in Pressurized Boiling and Non-Boiling Water," AECL1994.

[36] K. Khumsa-Ang and D. Lister, "Initial oxide particle deposition under low-temperature cooling water conditions: Experiments under subcooled boiling at high pH," *Heat Transfer Engineering,* vol. 34, pp. 702-711, 2013.

[37] F. P. Incropera, *Fundamentals of heat and mass transfer*, 6th ed.: Wiley, 2006.

[38] F. Cussac, "Modelling of particulate fouling on heat transfer surfaces: the influence of bubbles on the deposition of iron oxides on alloy-800 heater tubes," M.Sc.E., Chemical engineering, University of New Brunswick, 2007.

[39] L. G. Hamburger, "On the growth and rise of individual vapour bubbles in nucleate pool boiling," *International Journal of Heat and Mass Transfer,* vol. 8, pp. 1369-1386, 1965.

[40] M. G. Cooper and A. J. P. Lloyd, "The microlayer in nucleate pool boiling," *International Journal of Heat and Mass Transfer,* vol. 12, pp. 895-913, 1969.

[41] Y. Utaka, Y. Kashiwabara, M. Ozaki, and Z. Chen, "Heat transfer characteristics based on microlayer structure in nucleate pool boiling for water and ethanol," *International Journal of Heat and Mass Transfer,* vol. 68, pp. 479-488, 2014.

[42] H. Bindra and B. G. Jones, "Deposition of metallic colloids under sub-cooled nucleate boiling," *Colloids and Surfaces A: Physicochemical and Engineering Aspects,* vol. 397, pp. 85-91, 2012.

[43] M. Basset, "Deposition of magnetite particles onto alloy-800 steam generator tubes," M.Sc.E., Chemical Engineeering, University of New Brunswick, 1998.

[44] M. Kosmulski, "The pH-dependent surface charging and points of zero charge: V. Update," *Journal of Colloid and Interface Science,* vol. 353, pp. 1-15, 2011.

[45] K. Khumsa-Ang, "The deposition of nickel ferrite on Alloy-800 surfaces during subcooled boiling heat transfer: mechanisms of removal," Ph.D., Chemical Engineering, University of New Brunswick.

[46] D. Y. Kwok and A. W. Neumann, "Contact angle measurement and contact angle interpretation," *Advances in Colloid and Interface Science,* vol. 81, pp. 167-249, 1999.

[47] P. V. Balakrishnan, S. J. Klimas, L. Lépine, and C. W. Turner, "Polymeric dispersants for control of steam generator fouling," in *3rd International Steam Generator and Heat Exchanger Conference,* Toronto, 1998.

[48] P. Burgmayer, R. Crovetto, C. W. Turner, and S. J. Klimas, "Effectiveness of selected dispersants on magnetite deposition at simulated PWR heat-transfer surfaces," in *3rd International Steam Generator and Heat Exchanger Conference,* Toronto, 1998.

[49] E. Tombácz, A. Majzik, Z. Horvát, and E. Illés, "Magnetite in aqueous medium: coating its surface and surface coated with it," *Romanian Reports in Physics,* vol. 58, pp. 281 - 286, 2006.

[50] S. Catrouillet, C. Fonteneau, L. Bouteiller, N. Delorme, E. Nicol, T. Nicolai, *et al.*, "Competition between steric hindrance and hydrogen bonding in the formation

of supramolecular bottle brush polymers," *Macromolecules,* vol. 46, pp. 7911-7919, 2013.

[51] A. Wooding, M. Kilner, and D. B. Lambrick, "“Stripped” magnetic particles. Applications of the double surfactant layer principle in the preparation of water-based magnetic fluids," *Journal of Colloid and Interface Science,* vol. 149, pp. 98-104, 1992.

[52] M. A. Amin, S. S. A. Ei-Rehim, E. E. F. El-Sherbini, O. A. Hazzazi, and M. N. Abbas, "Polyacrylic acid as a corrosion inhibitor for aluminium in weakly alkaline solutions. Part I: Weight loss, polarization, impedance EFM and EDX studies," *Corrosion Science,* vol. 51, pp. 658-667, 2009.

[53] A. C. Joshi, A. L. Rufus, S. Suresh, P. Chandramohan, S. Rangarajan, and S. Velmurugan, "Characterization of the oxide formed in the presence of poly acrylic acid over the steam generator structural materials of nuclear power plants," *Journal of Nuclear Materials,* vol. 437, pp. 139-148, 2013.

[54] S. A. Umoren, Y. Li, and F. H. Wang, "Effect of aluminium microstructure on corrosion and inhibiting effect of polyacrylic acid in H2SO4 solution," *Journal of Applied Electrochemistry,* vol. 41, pp. 307-315, 2011.

[55] S. A. Umoren, Y. Li, and F. H. Wang, "Influence of iron microstructure on the performance of polyacrylic acid as corrosion inhibitor in sulfuric acid solution," *Corrosion Science,* vol. 53, pp. 1778-1785, 2011.

[56] L. Lépine and R. Gilbert, "Thermal degradation of polyacrylic acid in dilute aqueous solution," *Polymer Degradation and Stability,* vol. 75, pp. 337-345, 2002.

[57] A. Gurkaynak, F. Tubert, J. Yang, J. Matyas, J. L. Spencer, and C. C. Gryte, "High-temperature degradation of polyacrylic acid in aqueous solution," *Journal of Polymer Science Part A: Polymer Chemistry,* vol. 34, pp. 349-355, 1996.

[58] U. Ramminger, J. Fandrich, and A. Drexler, "An Innovative Strategy For Secondary Side System Lay-up Using Film-Forming Amines," in *7th CNS International Steam Generators to Control Conference*, Toronto, 2012.

[59] E. V. Chernyshev, E. N. Veprov, V. A. Petrov, S. L. Bogdanov, T. Y. Levina, T. I. Petrova, *et al.*, "Increasing the corrosion resistance of equipment due to the use of film-forming amines," *Power Technology and Engineering*, vol. 40, pp. 34-37, 2006.

[60] C. Foret, G. Stoianovici, G. Chaussec, A. de Bache, C. Z. Kolk, and W. Hater, "Study of efficiency and stability of film forming amines (FFA) for the corrosion protection of the carbon steel in water circuits," in *European corrosion congress EUROCORR 2008* Frankfurt, Germany, 2008.

[61] R. J. Harrison, R. E. Dunin-Borkowski, and A. Putnis, "Direct Imaging of Nanoscale Magnetic Interactions in Minerals," *Proceedings of the National Academy of Sciences of the United States of America*, vol. 99, pp. 16556-16561, 2002.

[62] L. Deydier de Pierrefeu, "The dissolution behavior of magnetite electrodes in high-temperature water," M.Sc.E., Chemical Engineering, University of New Brunswick, 2006.

[63] A. Iljinas, R. Brucas, V. Stankus, and J. Dudonis, "Synthesis of Fe3O4 thin films by solid state reactions," *Materials Science and Engineering: C*, vol. 25, pp. 590-594, 2005.

[64] Z. Wei, P. Duby, and P. Somasundaran, "Pitting inhibition of stainless steel by surfactants: an electrochemical and surface chemical approach," *Journal of Colloid and Interface Science*, vol. 259, pp. 97-102, 2003.

Appendix A: Magnetite Concentration Measurement Procedure

This procedure can be followed for expected magnetite concentrations of 2 ppm up to 240 ppm. In particular, it has given satisfactory results for magnetite concentrations of 5 to 15 ppm. The concentration measurement is based on the reaction of dissolved iron with a commercial iron reagent Ferrover® that forms an orange-red complex. The magnetite suspension thus has to be digested in acid and its pH has to be adjusted between 3 and 5 which is the optimal pH for the reagent-iron reaction. A spectrophotometer is finally used to measure the sample absorbance and convert it into the iron concentration in the sample.

Sample Preparation

1) Pour about 10 mL of Hydrochloric Acid (HCl) in a beaker. Take 5 mL of HCl using a clean and dry pipette and pour it in a clean and dry 100 mL-beaker.
2) Flush about 50 mL of coolant from the sample line to ensure that the stagnating water contained in the sampling line is completely removed.
3) Clean a 5 mL pipette and a 50 mL beaker and rinse them with the loop coolant at the purged sampling line.
4) Fill the rinsed 50 mL-beaker half way with the loop coolant.
5) Collect 5 mL of coolant with the pipette and pour it in the 100 mL-beaker containing 5 mL of HCl.
6) Cover the 100 mL beaker with a paraffin film to avoid loss by evaporation.
7) Place the beaker in a warm ultrasonic bath (about 40˚C) for 60 min.

8) Take the 100 mL-beaker in the ultrasonic bath back under the fume hood and tap on the paraffin film to make the condensed droplets fall into the solution.
9) Remove the film and dilute the solution it contains with 40 mL of deionized water.

Spectrophotometer Calibration

10) Prepare a blank solution containing a proportion of HCl equal to 1 mL of HCl for 60 mL of solution, and pour 30 mL into a clean and dry 50 mL-plastic beaker.
11) Clean a burette and rinse it with 5 molar sodium hydroxide solution (less than 1 mL).
12) Fill the burette with a few millilitres of NaOH 5N.
13) Pour NaOH very slowly in the plastic beaker containing the blank solution while measuring the solution pH.
14) Stop pouring NaOH once the solution pH is included in the range 3 to 5.
15) Fill a FerroVer® Iron Reagent AccuVac® ampoule with the pH-adjusted solution.
16) Calibrate the spectrophotometer using the ampoule containing the blank solution.

Sample Measurement

17) Stir the sample solution obtained at the end of the ‘Sample Preparation’ section using a clean stirring rod, take 5 mL of the solution and pour it into a clean and dry 50 mL plastic beaker.
18) Take 25 mL of deionized water and pour it into the plastic beaker. The proportion of HCl in the plastic beaker solution is now equal to 1 mL of HCl for 60 mL of solution.

19) Mix the solution and repeat the points 13) to 15).
20) Measure the iron concentration in the second AccuVac ampoule containing the sample solution.

Magnetite Concentration Calculation

By taking into account magnetite stoichiometry and the successive sample dilutions, including the one resulting from the pH adjustment, the magnetite concentration in the original 5 mL sample can be obtained from the iron concentration given by the spectrophotometer.

Appendix B: Magnetite Cluster Model – Matlab Code

The Matlab algorithm used is described succinctly in Figure 18. It is composed of a main function named *laserScan* that launches a double iterative loop. The first loop is used to test different values of the spacing angle θ^*. The second loop, included in the former, is scanning all the values of θ belonging to $[0\ ;\theta^*]$, calculating the magnetite cluster height and projected shadow for each of them.

Two simple functions *shadowArea* and *height* are called by the function *laserScan* within the double iterative loop. The inputs and outputs of these functions are shown in Table 11.

Table 11 Program functions description

	Inputs	Outputs
laserScan(l, p, run)	1. Cluster radius (in µm) 2. Cluster porosity percentage (decimal value) 3. Simulated run name	Plot of the magnetite deposit thickness and deposit mass in function of θ^*
shadowArea(r, h)	1. Cluster radius (in m) 2. Cluster shadow height (in m)	Area value (in m²) of the cluster projected shadow
Height(R, dia, theta)	1. Tube radius (in m) 2. Cluster diameter (in m) 3. Cluster angular position (in rad)	Height value (in m) of the cluster projected shadow

The detailed and commented code for these three functions used is shown below. Comments are preceded by '%'.

- Function *laserScan(l, p, run)*

```
function laserScan(l,p,run)

% radius conversion into metres
r=l*0.000001;

width=2*r;
R=0.01566/2;

% angular position for which the cluster shadow height nullifies
ThetaLim=acos((R-r)/(R+r));

% spacing angle for which clusters of the same plane 'touch' each other
ThetaMin=asin(r/(R+r));

% run# recognition; the two blank runs performed without additive,
% 'Mag1' and 'Mag2', correspond respectively to Run 4 and 7
PAA=strcmp(run,'PAA');
PMA=strcmp(run,'PMA');
Mag1=strcmp(run,'Mag1');
Mag2=strcmp(run,'Mag2');

% plot size adjustment for the two porosity values used (55% and 40%)
if (p==0.55)
    a=4;
    b=32;
    c=1;
    d=4;
elseif (p==0.4)
    a=4;
    b=16;
    c=1;
    d=2;
else
    a=2;
    b=8;
    c=1;
    d=1;
end

% experimental targets (deposit thickness and mass) adjustment
depending
% on the additive used
if (Mag1==1)
    targetMass=340;
    targetThickness=0.000003;
```

```
    ThetaMax=ThetaLim/a;
elseif (PAA==1)
    targetMass=75;
    targetThickness=0.0000005;
    ThetaMax=ThetaLim/b;
elseif (PMA==1)
    targetMass=160;
    targetThickness=0.000006;
    ThetaMax=ThetaLim/c;
elseif (Mag2==1)
    targetMass=340;
    targetThickness=0.000005;
    ThetaMax=ThetaLim/d;
else
    fprintf('\nAdditive name assignment error\n\n')
end

% initialization
devMass=targetMass/100;
devThickness=targetThickness/100;
iterations=100;
graphLimThickness=2*targetThickness;
graphLimMass=2*targetMass;
sum=[1,iterations];
thickness=[1,iterations];
fouling=[1,iterations];
N=[1,iterations];
d=[1,iterations];
V=[1,iterations];
M=[1,iterations];
A=[1,iterations];
i=(ThetaMax-ThetaMin)/(iterations-1);
x=0;

% first iterative loop
for theta=ThetaMin:i:ThetaMax
    x=x+1;
    n=0;
    sum(x)=0;

% calculation of the deposit mass assigned to 'fouling(x)'
    N(x)=2*pi/(2*theta);
    V(x)=4/3*pi*r*r*r*N(x);
    M(x)=(1-p)*V(x)*5.2*1000000000;
    A(x)=2*pi*R*width;
    fouling(x)=M(x)/A(x);

% second iterative loop
    for j=0:0.0001:theta
        n=n+1;
        if j > ThetaLim
            sum(x) = sum(x) + 0;
        else
```

```
% the functions shadowArea and height are called
            sum(x) = sum(x) + shadowArea(r,height(R,2*r,j))/width;
        end
    end
% thickness values are averaged
    thickness(x)=sum(x)/n;

% detection of computed deposit thickness and mass that are close to
% experimental values (plus or minus one hundredth of the target value)
    if ((targetThickness-devThickness) < thickness(x)) && (thickness(x)
<(targetThickness+devThickness)) && ((targetMass-devMass) < fouling(x))
&& (fouling(x) < (targetMass+devMass))

% if both thickness and mass values fit the experimental data, the
% corresponding spacing angle is displayed
        theta
    end
end

% plot of the magnetite deposit thickness and deposit mass in function
% of the spacing angle
figure;
x=1:1:iterations;
plot(x,targetThickness);
hold all
line = plotyy(x,thickness(x),x,fouling(x),'plot');
set(line(1),'ylim',[0 graphLimThickness],'YTick',targetThickness);
set(line(2),'ylim',[0 graphLimMass],'YTick',targetMass);
set(get(line(1),'Ylabel'),'String','Thickness (m)');
set(get(line(2),'Ylabel'),'String','Mass (mg/m2)');
xlabel('Theta*');

end
```

- Function *shadowArea(r, h)*

```
function a = shadowArea(r,h)

syms r

if h <= 0
    a=0;

% if the shadow height is positive and inferior to the cluster radius,
% a double integral is used to calculate the projected shadow
elseif (h>0) && (h <= r)
    fun = @(theta,r) r;
    rmin = @(theta) (r-h)./cos(theta);
    a = 2*integral2(fun,0,acos((r-h)/r),rmin,r);


% if the shadow height is superior to the cluster radius, the projected
% shadow of the top semi-circle and rectangular bottom shape is
calculated
elseif (h > r) && (h <= 2*r)
    a=pi*r*r/2+(h-r)*2*r;

end
```

- Function *Height(R, dia, theta)*

```
function h = height(R,dia,theta)

if R*(-1+cos(theta))+dia/2*(1+cos(theta)) >= 0
    h=R*(-1+cos(theta))+dia/2*(1+cos(theta));

else
    h=0;

end
```

Appendix C: Magnetite Cluster Model – Cluster Pattern Selection

The cluster pattern selection is composed of four steps listed below.

- The run to be simulated and a cluster porosity are selected.
- An initial value of the cluster radius is guessed.
- The function *laserScan* is launched and a plot of the idealised pattern thickness and mass in function of the pattern spacing angle is drawn.
- If the two curves do not intersect on the experimental target values (Figure 52), the cluster radius is modified until they do (Figure 53).
- The spacing angle at the intersecting point of Figure 53 is reported in Table 8.

The case of the PMA run at a cluster porosity of 55% is presented here as an example. On the two figures shown below, the unique value displayed on each ordinate axis is the experiment target values. Besides, the abscissa axis does not show the value of θ^* but a partition of the angular range analysed (abscissa values shown are arbitrary).

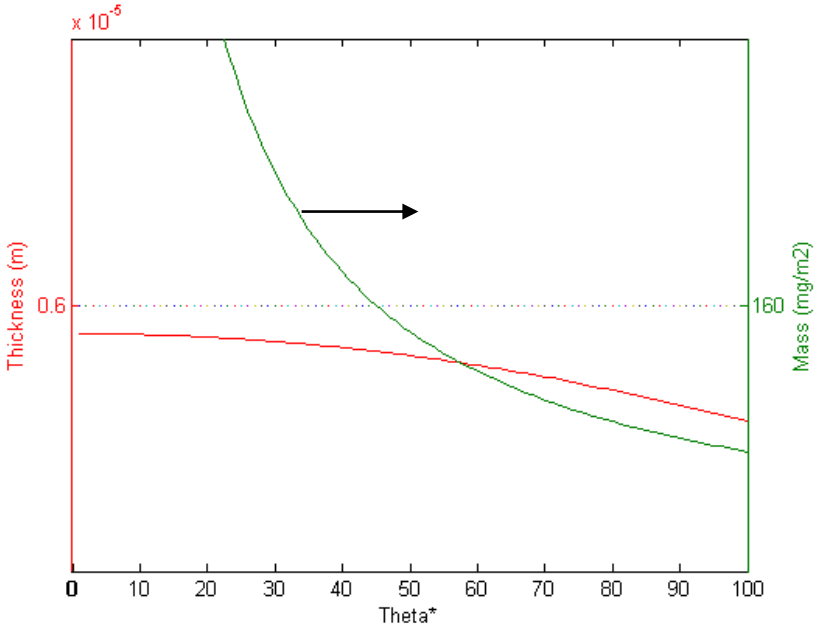

Figure 52 Plot drawn by laserScan(3,0.55,'PMA') for a cluster radius of 3 µm

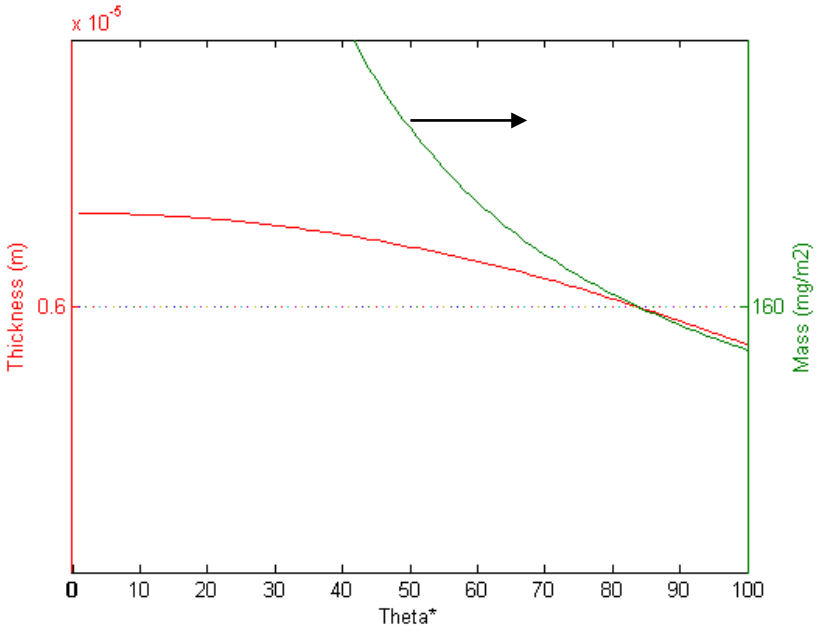

Figure 53 Plot drawn by laserScan(4.533,0.55,'PMA') for a cluster radius of 4.533 μm

Appendix D: Bump Height Calculation

Orange fingertip case

Considering the laser scan performed on the orange fingertip at 100 revolutions per minute and 0.2 mm per revolution shown on Figure 46, the measurement of the sinusoid amplitude gives a height h_{ora} of about 0.87 mm. However this height measurement results from the averaging of 40 measurement recorded by the laser device, which records at a frequency of 400 per second. Thus, at the rotation speed mentioned above, the laser takes a measure every 0.02618 rad and records an average value every 1.0472 rad, the latter value being the one that appears on the scan results graphs.

In order to calculate the bump height, the evolution of the projected shadow height over the angular range $[0\ ;\ 1.0472]$ needs to be investigated by imitating the laser device recording procedure. By computing the bump height every 0.02618 rad during the rotation of the tube until 40 measurements are taken, the average shadow height over the considered angular range can be obtained. An approximated bump height, such as h_{ora}, is used to perform the first angular sweep. Using a trial and error approach, the bump height may then be modified in order to reach an average shadow height that fits with the sinusoid amplitude h_{ora}.

The shadow height is computed using the function *height* of the magnetite cluster Matlab program. Also, it is assumed that the 40 measurements required are performed at a fixed position along the tube, where the heights recorded are the highest (for instance the abscissa 0.8 cm on Figure 46). This assumption is reasonable as it will only take 0.1

second for the helical scan setup to record a 40-measurement average, which corresponds to an axial translation of 34 µm.

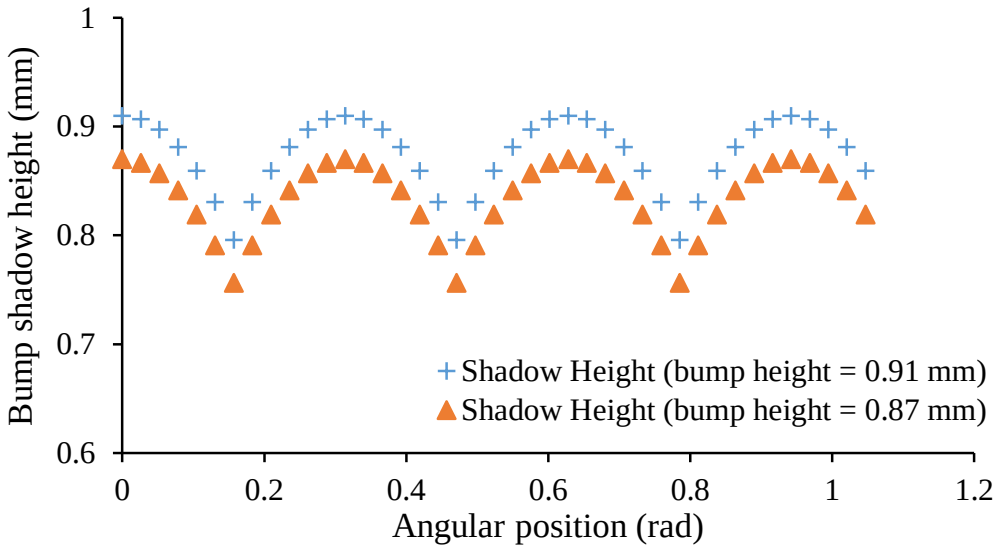

Figure 54 Bump shadow height profile during the tube rotation

The first and last trials of the trial and error procedure are shown on Figure 54. The first trial, corresponding to a bump height of 0.87 mm, provides an average shadow height of 0.83 mm, which is smaller than the sinusoid amplitude h_{ora}. The bump height is then increased progressively until the value 0.91 mm which results in an average shadow height of 0.87 mm over the 40 measurements. A bump height of 0.91 mm thus results in an average shadow height that fits the experimental value of the sinusoid amplitude h_{ora}.

$$Orange\ bump\ height\ h_0^{ora} = 0.91\ mm$$

Red fingertip case

As with the orange fingertip case, the evolution of the projected shadow height of the red fingertip over the angular range $[0\,;1.0472]$ is investigated by computing the bump height every 0.02618 rad (the same scanning speeds are used as for the orange fingertip). To do so, the case scenario that maximized the average shadow height over 40 measurements is chosen. This is assumed to be the case where the angular range starts with the 'abnormal' angular range described in Figure 50, the remaining of the 40 measurements being taken over the 'normal' angular range giving shadow height below or equal to one bump height. The adjusted shadow height evolution over the considered angular range is presented on Figure 55.

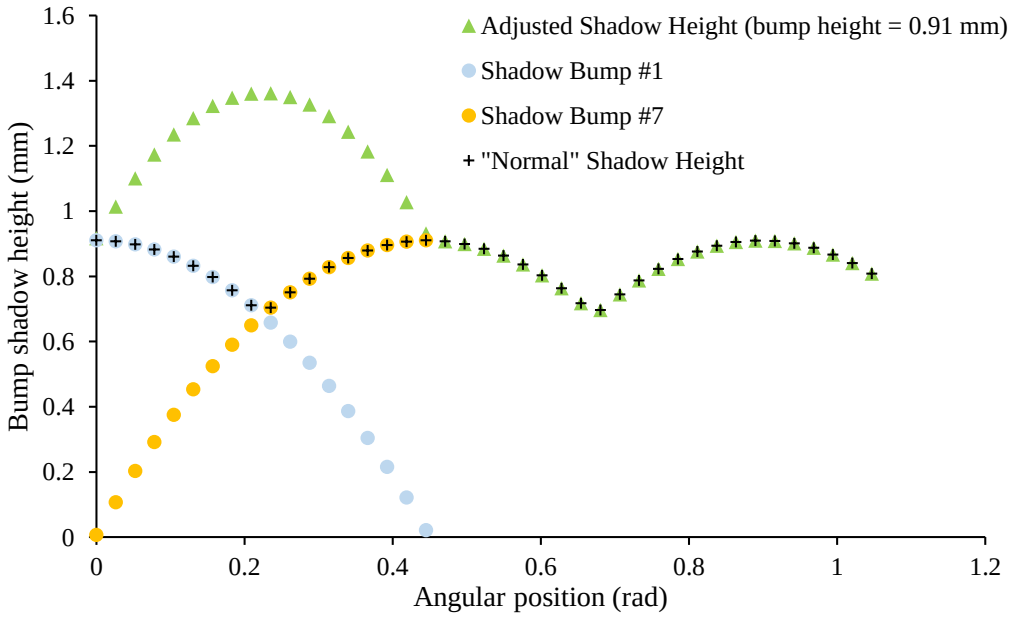

Figure 55 Bump projected shadow height during the tube rotation

The adjusted curve is equal to the sum of the shadows of Bump #1 and #7 until the Bump #1 is completely shadowed by the tube. At this angular position, the adjusted curve starts following the 'normal' bump shadow height corresponding to the contribution of only one bump to the diameter increase read by the laser sensor.

Using the same trial and error method as for the orange fingertip, the bump height is successively adjusted so that the averaged value of the adjusted shadow height is equal to the experimental scan amplitude $h_{red} = 0.91$ mm. The first and last trials are depicted on Figure 56. The bump height of 0.85 mm is the one that fits the experimental scan values the best, leading to an average shadow height value of 0.916 mm.

$$Red\ bump\ height\ h_0^{red} = 0.85\ mm$$

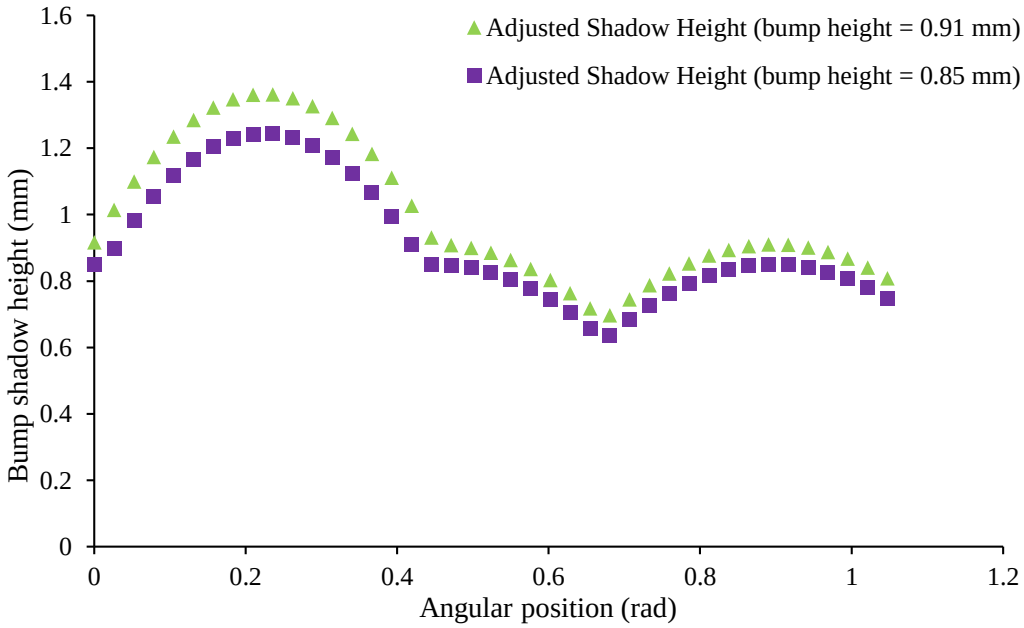

Figure 56 Bump projected shadow height during the tube rotation

Curriculum Vitae

Candidate's full name: Cyprien Patrick Gasnier

Universities attended:

- Ecole Nationale Supérieur des Mines de Saint-Etienne (2009-2011)
  Ingénieur Civil des Mines (2014)

Publications:

- C. Gasnier and D. Lister, "The effect of chemical additives on magnetite deposition in boiling heat transfer," in International Conference on Heat Exchanger Fouling and Cleaning, Budapest, 2013.

Conference Presentations:

- C. Gasnier and D. Lister, "The effect of chemical additives on magnetite deposition in boiling heat transfer" in International Conference on Heat Exchanger Fouling and Cleaning, Budapest, 2013.
- C. Gasnier and D. Lister, "The effect of chemical additives magnetite deposition in boiling heat transfer and on surface properties" in Canadian Chemical Engineering Conference, Fredericton, 2013.